Band Structure of Crystalline Anthracene and Its Dependence On Pressure

By

Salah E. Elnahwy

A dissertation submitted to the Graduate Faculty in Physics in partial fulfillment of the requirements for the degree of Doctor of Philosophy, The City University of New York.

1976

This manuscript has been read and accepted for the Graduate Faculty in Physics in satisfaction of the dissertation requirement for the degree of Doctor of Philosophy.

Feb 5 1976
date

Arthur C. Danek
Chairman of the Examining committee

February 17, 1976
date

Myriam P. Sarachik
Executive Officer

Professor George J. Dienes
Professor Milton Furst
Professor Arthur Paskin
Professor Martin Pope
Professor William Whitten

Supervisory Committee

The City University of New York

Acknowledgement

The author wishes to express his deepest gratitude to his major advisor Professor Arthur . C. Damask for supervising this work. He provided both the facilities and the atmosphere to develop a broad spectrum of skills. His constant stimulation and advice made the completion of this work possible. Finally his contribution and prompt reviewing of this manuscript is most appreciated by the author. The author would also like to thank Prof. William Whitten for providing his valuable experience in the field. The design of the High Pressure System would not have been possible without the experience and co-operation of Prof. William Daniels of the University of Delaware. Thanks are also due to Dr. David Cox of Brookhaven National Laboratory for colaborating in the neutron diffraction work. Prof. George J. Dienes has kindly guided the work on the elastic constants. The author also wishes to thank Brookhaven National Laboratory for allowing him to use the facilities of the laboratory. The Air Force of the United States of America and the City University of New york have kindly supported the project through their grants.The author appreciates the support he recieved from the Physics Department of Queens College and likes to thank all the faculty,secretaries and science assistants for the friendly atmosphere.

Table of contents

Tables

Figures

Chapter I

Introduction

This work is on the band structure of crystalline anthracene and its pressure dependence. In this chapter, we discuss the general characteristics of crystalline anthracene, the experimental facts about charge transport in anthracene, and the objectives of this investigation are stated.

It will be shown that this work introduces an internally consistent band model which is in good agreement with the available experimental data.

A. General characteristics of crystalline anthracene.

Anthracene, a planar polycyclic aromatic hydrocarbon (see fig.1.1), has been used in scintillation counters for many years. Thus, being readily available commercially, in what was believed to be an adequately pure crystalline form, anthracene has long been considered by many to be a prototype material for the investigation of the properties of organic semiconductors.

Most of these organic semiconductors have very high electrical resistivity. Their dark electrical conductivity increases exponentially with temperature as $\sigma = \sigma_0 \exp\left(-\frac{E}{kT}\right)$, hence the name semiconductors. The conductivity arises usually from the injection of charge carriers into the organic semiconductor by some extrinsic means such as by contacts, adsorbed gases, or impurities.
For anthracene $E = 0.85$ e.v., $\sigma_0 \simeq 2.5 \times 10^{-31}$ $(\text{ohm.cm})^{-1}$, and $\sigma_{20°C} \simeq 10^{-15} (\text{ohm.cm})^{-1}$. Since $2E$ is smaller than the band gap, as can be seen from Fig. 1.3, for anthracene,

Fig. 1.1. The molecular structure of anthracene, $C_{14}H_{10}$. The C-C bond lengths are approximately 1.4 Å, and the C-H bond lengths are approximately 1.1 Å at 290 K.

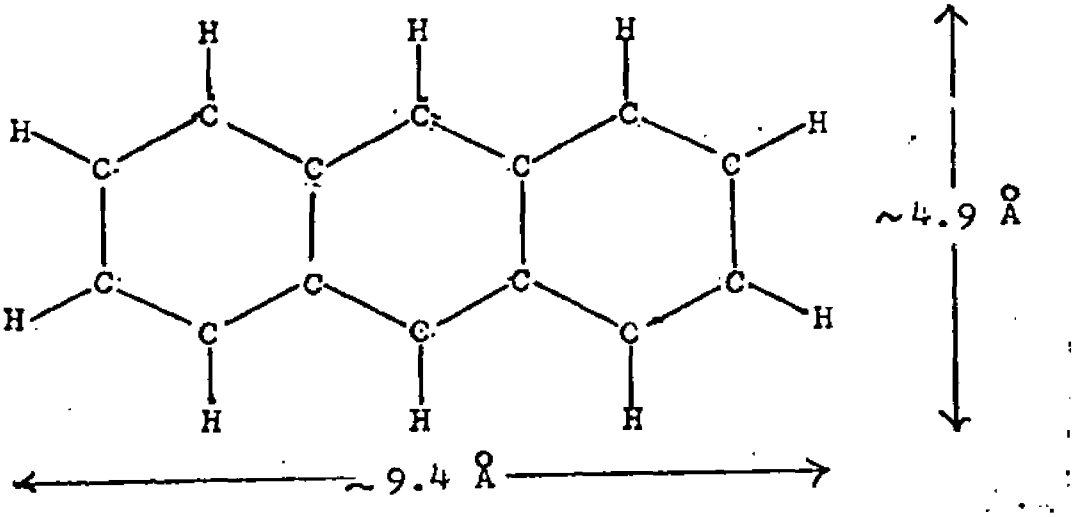

The conduction must be extrinsic. Pope[23] has measured the conduction threshold by the Millikan oil drop technique. He reported a value of 3.7 e.v. In a later review paper[24] he concluded that the gap energy is 3.8 ± 0.1 e.v.

Organic semiconductors belong to the class of solids known as molecular crystals. The binding forces of these crystals are the Van der Waals forces, and the molecules are relatively far from one another.

Due to the weak crystal forces, the molecular energy levels are relatively undisturbed in a molecular crystal. In order to obtain charge transport, it is necessary, at the very least, to excite an electron into one of these molecular states. The electronic states of aromatic molecules are assumed to factor into noninteracting sets of σ- orbitals and π-orbitals. The σ-orbitals are symmetrical around the bond axis, giving localized C-C and C-H bonds. The π- orbitals are perpendicular to the molecular plane. Fig. 1.2 is a composite sketch of three benzene molecular orbitals for anthracene. The composite was made from a sketch of the molecular orbitals of a benzene molecule[1] and is used to give a schematic representation of the σ and π- orbitals. Any π- orbital overlaps equally with both of its neighbors so that the π- electrons are completely delocalized.

Considering only the π- orbitals, the ground state of the molecule is obtained by placing pairs of electrons, with opposite spin, into the lowest orbitals. There are an even number of electrons in anthracene. The state of lowest energy is a singlet state. An excited state may be obtained by removing an electron from the uppermost filled orbital of the ground state to a vacant orbital of higher energy. If the spin is conserved in this process, the total spin of the excited state is zero, giving rise to an excited singlet state. If there is a spin reversal, the total spin of the excited state is one, resulting in a triplet state. The first excited singlet and triplet states of an anthracene crystal are shown schematically relative to the singlet ground state in fig. 1.3.

FIG. I.2. ANTHRACENE MOLECULAR ORBITALS.
(a) LOCALIZED σ-ORBITALS; (b) UNLOCALIZED π-ORBITALS.[1]

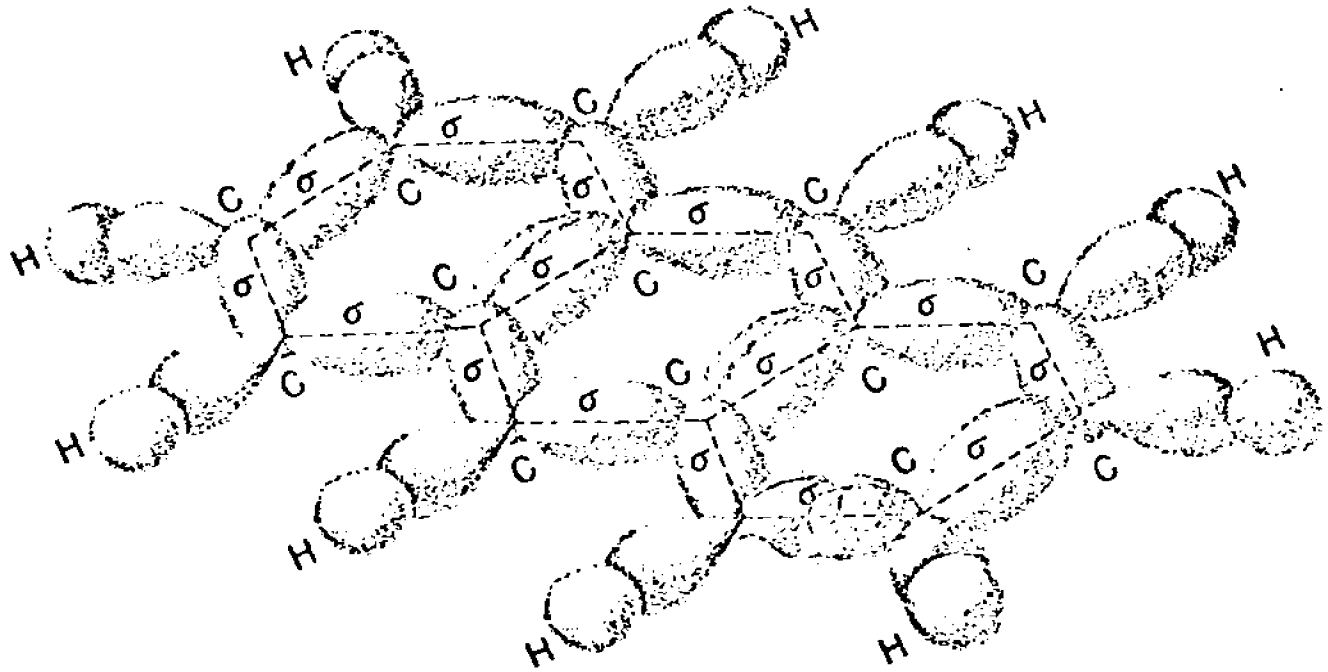

(a)

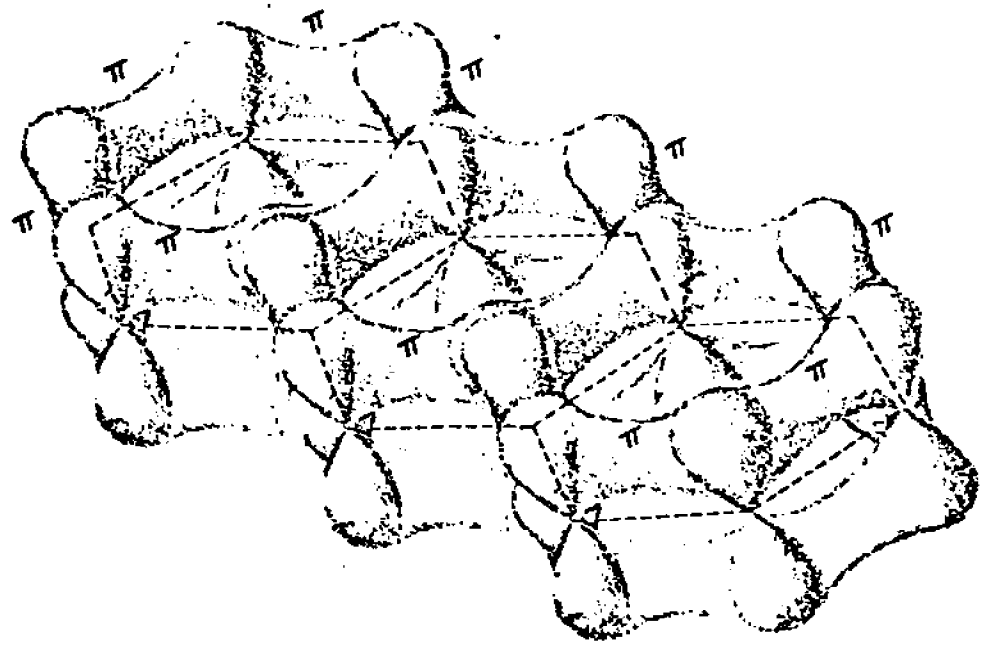

(b)

Fig. 1.3. The first excited singlet and triplet states of anthracene single crystals.

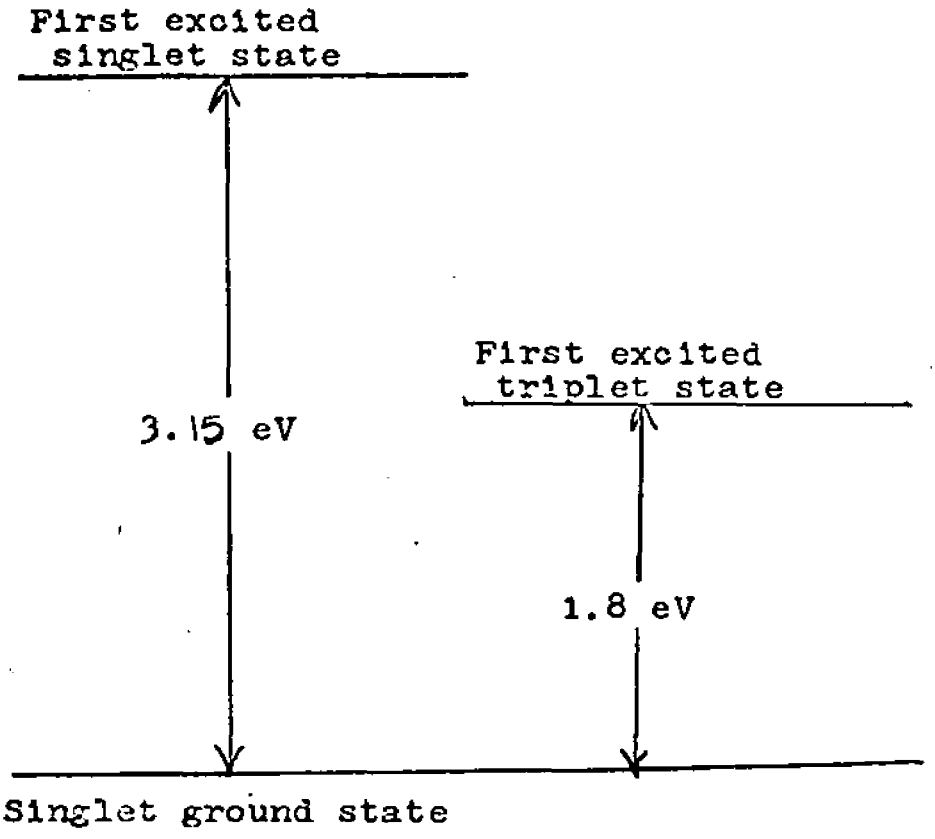

B. Experimental facts about charge transport in crystalline anthracene.

Kepler[2] and LeBlanc[3] have measured the drift mobilities of electrons and holes injected in small numbers in an otherwise neutral anthracene crystal.
Two facts have been clearly established: (1) The mobilities of both holes and electrons are of the order of 1 cm^2/volt.sec at room temperature (2) The mobilities vary with absolute temperature as T^{-n} , with $1 < n < 2$.
In a later investigation Kepler[4] measured the change of the drift mobilities of electrons and holes in anthracene with pressure at 3 kilobars. More recently Kajiwara et al[5] measured the drift mobilities of electrons in anthracene at different pressures up to 6.6 kilobars. Their results are very close to those of Kepler.
Several investigators tried to measure the Hall mobility of injected carriers in anthracene [6-13]. Although the quantitative data obtained are in question, because of the experimental difficulties involved in such a measurement, a general conclusion was that the Hall mobility is anomalous in sign for some directions of the magnetic field[13].
More recently Dresner [25] has measured the Hall mobility of volume generated holes in anthracene under space charge conditions. His results do not show such sign anomaly, they are also larger in magnitude than previously reported values.

A mechanism of charge- carrier transport that involves phonon - assisted hopping from molecule to molecule would imply that the carrier mobility increases with temperature contrary to experiment. On the hand, a band scheme is consistent with the experimental temperature dependence of the drift mobility mentioned above. This led LeBlanc and others[14-19] to

attempt calculations of the excess electron and excess hole band structures and the mobilities of charge carriers in crystalline anthracene. These calculations are discussed in detail in chapter IV.
In order to be physically meaningful, such a band scheme must satisfy a stringent condition imposed by the uncertainty principle.[20] One possible statement of this restriction is that the carrier mean free path with respect to scattering must be larger than the lattice spacings. Or equivalently the uncertainty of the energy associated with the relaxation time must be smaller than the bandwidth*. Although, as will be shown in chapter IV, the band schemes mentioned predicted the anisotropy of the drift mobility to agree fairly well with experiment, the internal consistency of these calculations remains in question.

LeBlanc[21] and Toombs[16] have shown that the band model predicts the anomaly of the sign of the Hall mobility observed experimentally. However, a hopping model introduced by Munn and Siebrand[22] has also predicted such anomaly.

Finally, comparison of the change of the drift mobility with pressure, as predicted by the band theory, with the experimental data was not possible before the present investigation because the linear compressibilities of crystalline anthracene were not known.

C. Thesis objectives.

Based on the previous observations it was believed that by using better molecular wavefunctions than the ones used by the other investigators we could improve both the agreement between the theoretical and experimental values of the drift mobility as well as the internal consistency of the model. Secondly, by determining the

---

* Actually this condition is too stringent since the band widens by kT at any temperature T ather than zero.

linear compressibilities of crystalline anthracene, the pressure dependence of the band structure could be determined. These results can be used to test the band model against the experimental pressure data.

The plan of the work was as follows:

1. Sample preparation, this involves growing pure single crystals of anthracene as explained in chapter III.

2. The determination of the linear compressibilities by neutron diffraction techniques at high pressure.

3. Calculation of the band structure and its pressure dependence using improved molecular wavefunctions.

4. Calculation of the drift mobility tensor at different pressures and comparing the results with the experimental data available.

5. Calculation of the Hall mobility, for the six possible directions of the current and the magnetic field, at different pressures.

6. The development of a high pressure gas system with the following specifications:
a. A non-magnetic pressure cell with two optical windows and as many as five electrical leads available at the outside.
b. A miniaturized sample holder which can fit into the cell.
c. A precise method to measure the pressure.

7. Measurement of the Hall mobility at different pressures and comparing the results with the theoretical predictions.

All parts of the plan were completed. However no quantitative data were obtained for the Hall mobility because of a new effect reported for the first time in these crystals as will be discussed in chapter V.

References - chapter I

1. M.Alonso and E.J.Finn, Fundamental University Physics (Addison- Wesley Publishing co.,Inc., Reading,Mass.,1968),vol.III,p.211.

2.R.G.Kepler,Phys.Rev.119,1226(1960).

3. O.H.LeBlanc,J.Chem.Phys.33,626(1960).

4. R.G.Kepler in Organic Semiconductors conference, edited by J.J.Brophy and J.W.Buttrey (The Macmillan Company. New York 1962),p1.

5. Takashi Kajiwara,Hiroo Inokuchi and Shigeru Minomura Bull.of the Chem.soc.of Jap.vol 40,No.5 105?(1967)

6. T.Toombs , Ph.D.Thesis,Princeton University (unpublished,1968).

7. J.Dresner,Phys.Rev.1?3,558(1966).

8. G.Delacote and M.Schott,Solid State Comm.4,177(1966)

9. R.Pethig and K.Motgan, Nature 214,266(1967).

10. V.N.Dobrovol'skii and Yu.I.Gritsenko,Soviet Physics-solid state 4,2025 (1963).

11. G.C.Smith,Bull.Am .Phys.Soc.14,370 (1969).

12. A.G.Redfield,Phys.Rev.94,526 (1954).

13. A.Korn,R.A.Arndt,and A.C.Damask,Phys.Rev.186,938(1969).

14. O.H.LeBlanc Jr.,J.Chem.Phys.35,1275(1961).

15. G.D.Thaxton,R.C.Jarnagin,And M.Silver,J.Phys.Chem. 66,2461(1962).

16. J.I.Katz,S.A.Rice,S.Choi,and J.Jortner,J.Chem.Phys. 39,1683 (1963).

17. R.Silbey,J.Jortner,S.A.Rice,And M.T.Vala Jr,J.Chem. Phys.43,2925(1965).

18. R.M.Glaeser, and R.S.Berry,J.Chem.Phys. 44,3797 (1966).

19. Chojnacki, Molecular Crystals 3,375 (1967).

20. H. Frohlich and Sewell,Proc.Phys.Soc. 74,643 (1959).

21. O.H.LeBlanc Jr ,J.Chem.Phys. 39,2395 (1963).

22. R.W.Munn and W.Siebrand,Phys.Rev.B,vol 2,No.8,3435 (1970).

23. Martin Pope,Scientific American 216,86 (1967).

24. Martin Pope and Hartmut Kallmann,Discuss. of Faraday Soc. 51, p.7 (1971).

25. J.Dresner,J.Chem.Phys. Vol 52,No.12,p.6343.

Chapter II
Drift and Hall Mobilities

This chapter consists of two main sections as follows:

A. Elementary theory of the Hall effect.
   This section deals with basic definitions and description of the Hall effect.

B. General theory of the drift and Hall mobilities.
   Expressions of the drift and Hall mobilities, in the general case of a statistical distribution of drift velocities, are derived by solving the Boltzmann transport equation.

A. Elementary theory of the Hall effect.

The usual geometry used to describe the simple Hall effect is shown in Fig. 2.1. A longitudinal current J_x is flowing in a sample in the shape of a rectangular parallelopiped. On applying a magnetic field in a direction normal to that of the current, along the z- axis in Fig. 2.1, charge carriers are deflected due to the Lorentz force given by $q\,\underline{V} \times \underline{B}$.

Positive charge carriers acquire a velocity component in the negative y- direction.

If no current is allowed to leave the sample in the y- direction, charges will accumulate on the sides normal to y- axis. This charge accumulation produces an electric field E_H which in turn exerts a force on the charge carriers opposite to the Lorentz force. Charge accumulation will continue resulting in an increasing value of E_H until it produces a force equal in magnitude to the Lorentz force. With this value of the field E_H the net transversal force on the charge carriers will be zero and there will not be any more deflection as they travel across the sample.

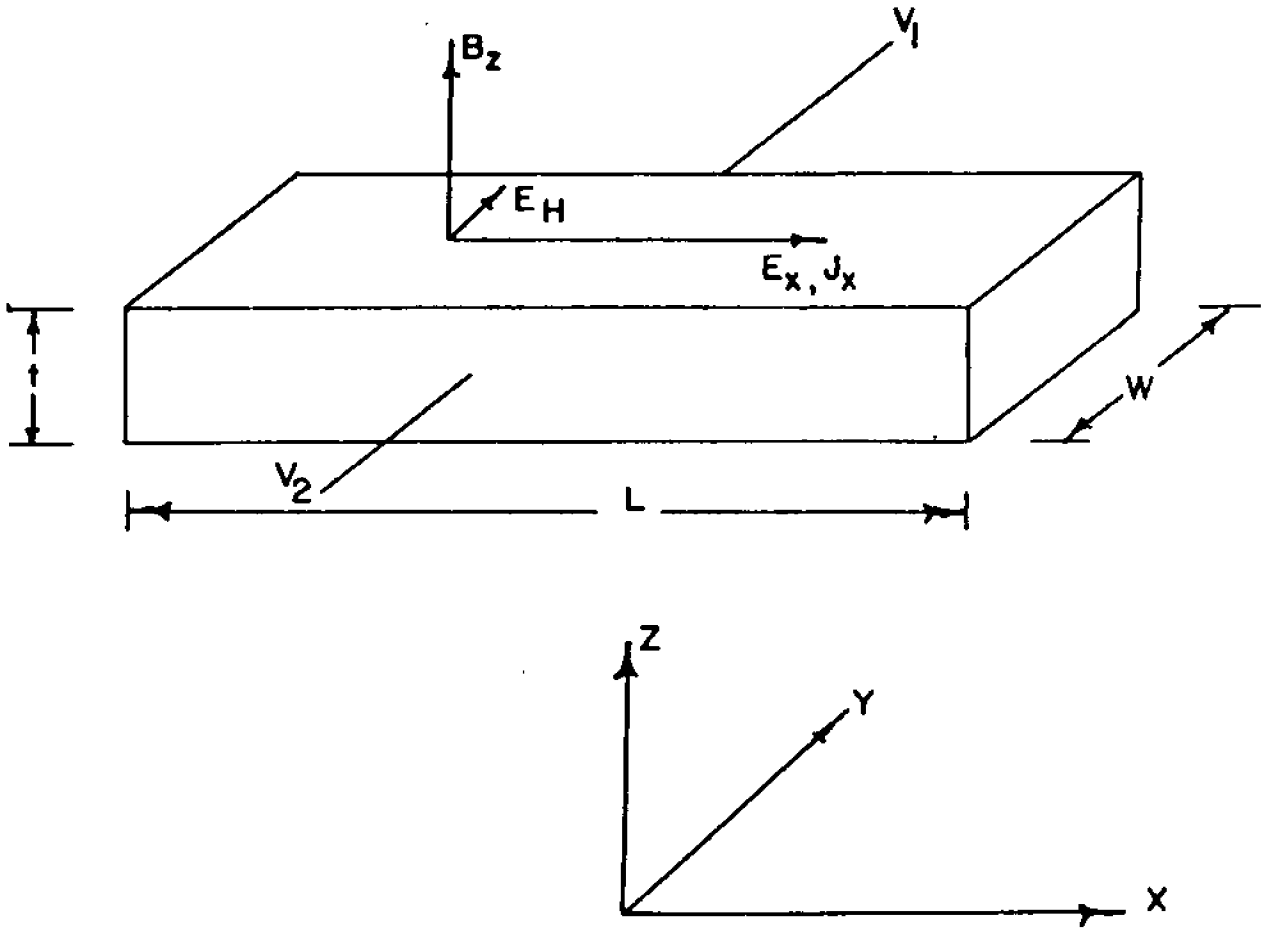

FIG. 2.1

The electric field E_H is called the Hall field and it is given by the Condition of zero force as follows:

$$q\underline{E}_H = -q\,\underline{V} \times \underline{B} \qquad (2.1)$$

$$\therefore \quad \underline{E}_H = -\underline{V} \times \underline{B} \qquad (2.2)$$

with the configuration of Figure 2.1 equation 2.2 becomes

$$E_H = V_x B_z \qquad (2.3)$$

The longitudinal current density J_x is given by

$$J_x = n q V_x \qquad (2.4)$$

where n is volume density of the charge carriers.

Substituting equation 2.4 into equation 2.3 it becomes

$$E_H = J_x B_z / nq \qquad (2.5)$$

The Hall Coefficient is defined by

$$R_H = E_H / J_x B_z \qquad (2.6)$$

The Hall mobility is defined as

$$\mu_H = \sigma R_H \qquad (2.7)$$

Where σ is the conductivity in the x- direction.

From (2.6) and (2.7) μ_H is given by

$$\mu_H = \sigma E_H / J_x B_z \qquad (2.8)$$

$$\text{Since } J_x = \sigma E_x \qquad (2.9)$$

therefore μ_H can be written as

$$\mu_H = E_H / E_x B_z \qquad (2.10)$$

In this simple analysis equation (2.5) and (2.6) lead to

$$R_H = \frac{1}{nq} \qquad (2.11)$$

Since $\sigma = \eta q \mu_D$ (2.12)

Where μ_D is the drift mobility in the x - direction, plugging equations(2.11) and (2.12) into equation (2.7) it reduces to $\mu_H / \mu_D = 1$ (2.13)

This simple equivalence between the drift and Hall mobilities results from the assumption that all carriers will have the same drift velocity. In general, this is not true as will be shown later on (page 19). Therefore a general treatment using the transport theory is necessary to derive expressions for both drift and Hall mobilities.

The Hall field E_H results in a Hall voltage V_H given by (see Fig. 2.1)

$$V_H = V_2 - V_1 = W E_H \qquad (2.14)$$

$$\therefore \mu_H = V_H / W E_x B_z \qquad (2.15)$$

Equations 2.6, 2.7, and 2.5 will be used as definitions in the next section.

B. General theory of the drift and Hall mobilities.

In all of the following analysis only one type of charge carrier will be assumed responsible for conduction, although the analysis applies equally well for either type.

The Boltzmann transport equation is usually written as:(1)

$$\underline{F} \cdot \underline{\nabla}_{\underline{p}} f + \underline{v} \cdot \underline{\nabla}_{\underline{r}} f + \frac{\partial f}{\partial t} = \left(\frac{\partial f}{\partial t}\right)_{Coll} \qquad (2.16)$$

Where $f(\underline{r},\underline{p},t)\,d\underline{p}\,d\underline{r}$ is the number of particles in the volume element $d\underline{r}$ around $\underline{r}$ in the momentum volume element $d\underline{p}$ around $\underline{p}$ at time t . $\underline{F}$ is the force on the particle, $\underline{V}$ is the velocity of the particle, and $\left(\frac{\partial f}{\partial t}\right)_{Coll}$ is the rate of change of the distribution function f due to collision.

In the steady state $\frac{\partial f}{\partial t} = 0$ and equation (2.16) becomes

$$\underline{F}\cdot\nabla_{\underline{p}} f + \underline{V}\cdot\nabla_{\underline{r}} f = \left(\frac{\partial f}{\partial t}\right)_{Coll} \qquad (2.17)$$

If the medium is homogeneous, f does not depend on the position and $\nabla_{\underline{r}} f$ will be zero. For an electron moving in a magnetic field

$$\underline{F} = -e\left(\underline{E} + \underline{V}\times\underline{B}\right) \qquad (2.18)$$

In this case the Boltzmann equation reduces to

$$-e\left(\underline{E} + \underline{V}\times\underline{B}\right)\cdot\nabla_{\underline{p}} f = \left(\frac{\partial f}{\partial t}\right)_{Coll} \qquad (2.19)$$

In the absence of external fields and at thermal equilibrium f is given by the Fermi-Dirac distribution function

$$f_o = \frac{1}{\exp\left[(\mathcal{E}-\mathcal{E}_f)/kT\right] + 1} \qquad (2.20)$$

Where $\mathcal{E}_f$ is the Fermi level. When there are external fields which cause f to change only slightly from f_o, different degrees of approximations [2] are used for the term $(\partial f/\partial t)$ collision. In this work the so-called relaxation time approximation is used in which $\left(\frac{\partial f}{\partial t}\right)_{Coll} \simeq -(f-f_o)/\tau$ that is, the rate of change of

f due to collision is proportional to the negative of the change from the equilibrium value.

Substituting this expression of $\left(\frac{\partial f}{\partial t}\right)_{Coll}$ in equation (2.19), the Boltzmann equation takes the form (2.21)

$$-e\left(\underline{E}+\underline{v}\times\underline{B}\right)\cdot\nabla_{\underline{p}} f = -\left(f-f_0\right)/\tau \qquad (2.21)$$

A method developed by Jones and Zener[3] is used to solve the Boltzmann equation. A new dependent variable ϕ is introduced such that $f = f_0 - \phi\frac{\partial f_0}{\partial \mathcal{E}}$ (2.22), ϕ is now to be determined from the solution of the Boltzmann equation (2.21). The velocity of the electron is the group velocity, given by $\underline{v} = \nabla_{\underline{k}}\omega = \frac{1}{\hbar}\nabla_{\underline{k}}\mathcal{E}$ (2.23). Since $\underline{p} = \hbar\,\underline{k}$, thus $\nabla_{\underline{p}} = \frac{1}{\hbar}\nabla_{k}$ (2.24). The term $\nabla_{\underline{p}} f$ is now evaluated:

$$\nabla_{\underline{p}} f = \frac{1}{\hbar}\nabla_{\underline{k}} f = \frac{1}{\hbar}\left[\nabla_{\underline{k}} f_0 - \left(\nabla_{\underline{k}}\phi\right)\frac{\partial f_0}{\partial \mathcal{E}} - \phi\,\nabla_{\underline{k}}\frac{\partial f_0}{\partial \mathcal{E}}\right]$$

Since f_0 is a function of $\mathcal{E}$ only, therefore

$$\nabla_{\underline{k}} f_0 = \frac{\partial f_0}{\partial \mathcal{E}}\nabla_{\underline{k}}\mathcal{E} = \hbar\,\underline{v}\frac{\partial f_0}{\partial \mathcal{E}} \qquad (2.25)$$

Also

$$\nabla_{\underline{k}}\frac{\partial f_0}{\partial \mathcal{E}} = \hbar\,\underline{v}\frac{\partial^2 f_0}{\partial \mathcal{E}^2}$$

Therefore $\nabla_{\underline{p}} f = \underline{v}\left(\frac{\partial f_0}{\partial \mathcal{E}} - \phi\frac{\partial^2 f}{\partial \mathcal{E}^2}\right) - \frac{1}{\hbar}\frac{\partial f_0}{\partial \mathcal{E}}\nabla_{\underline{k}}\phi$ (2.26)

with this expression for $\nabla_{\underline{p}} f$, the term $\left(\underline{v}\times\underline{B}\right)\cdot\nabla_{\underline{p}} f$ becomes:

$$\left(\underline{v}\times\underline{B}\right)\cdot\nabla_{\underline{p}} f = \left(\underline{v}\times\underline{B}\right)\cdot\left[\underline{v}\left(\frac{\partial f_0}{\partial \mathcal{E}} - \phi\frac{\partial^2 f}{\partial \mathcal{E}^2}\right) - \frac{1}{\hbar}\left(\nabla_{\underline{k}}\phi\right)\frac{\partial f_0}{\partial \mathcal{E}}\right]$$

since $\left(\underline{v}\times\underline{B}\right)\cdot\underline{v} = 0$

therefore $(\underline{v} \times \underline{B}) \cdot \nabla_{\underline{p}} f = -\frac{1}{\hbar}[(\underline{v} \times \underline{B}) \cdot \nabla_{\underline{k}} \Phi] \frac{\partial f_0}{\partial \mathcal{E}}$

$$= -\frac{1}{\hbar}\left(\frac{\partial f_0}{\partial \mathcal{E}}\right) \underline{B} \cdot (\nabla_{\underline{k}} \Phi \times \underline{v})$$

$$= \frac{1}{\hbar}\left(\frac{\partial f_0}{\partial \mathcal{E}}\right) \underline{B} \cdot (\underline{v} \times \nabla_{\underline{k}} \Phi)$$

$$= \frac{1}{\hbar} \frac{\partial f_0}{\partial \mathcal{E}} \underline{B} \cdot \left(\frac{1}{\hbar} \nabla_{\underline{k}} \mathcal{E} \times \nabla_{\underline{k}} \Phi\right)$$

$$= \frac{1}{\hbar^2}\left(\frac{\partial f_0}{\partial \mathcal{E}}\right) \underline{B} \cdot \underline{\Omega} \Phi \qquad (2.27)$$

where $\underline{\Omega}$ is the vector operator defined by

$$\underline{\Omega} = \nabla_{\underline{k}} \mathcal{E} \times \nabla_{\underline{k}} \qquad (2.28)$$

If equations (2.22), and (2.27) are substituted in the Boltzmann equation (2.21), an equation for the variable $\Phi(\underline{k})$ is obtained as:

$$\Phi/\tau + \frac{e}{\hbar} \underline{E} \cdot \nabla_{\underline{k}} \mathcal{E} + \frac{e}{\hbar^2} \underline{B} \cdot \underline{\Omega} \Phi = 0 \qquad (2.29)$$

In deriving equation (2.29), terms in E^2 and $E\Phi$ are neglected since equation (2.22) is considered as a first order expansion of f in powers of E. The solution of (2.29) will be shown to be consistent with these approximations.

Jones and Zener[3] solved this equation by iteration. They expressed Φ in ascending powers of $\underline{B}$ as follows:

$$\Phi = -\frac{e}{\hbar}[\tau \underline{E} \cdot \nabla_{\underline{k}} \mathcal{E} - \frac{e}{\hbar^2} \tau \underline{B} \cdot \underline{\Omega}(\tau \underline{E} \cdot \nabla_{\underline{k}} \mathcal{E}) +$$

$$\frac{e^2}{\hbar^4} \tau \underline{B} \cdot \underline{\Omega}(\tau \underline{B} \cdot \underline{\Omega}(\tau \underline{E} \cdot \nabla_{\underline{k}} \mathcal{E})) + \cdots] \qquad (2.30)$$

The density of states per unit volume in the $\underline{K}$ space is $2/(2\pi)^3$ where the factor 2 in the numerator accounts for the two possible orientations for the spin. The current density due to electrons is therefore given by:

$$\underline{J} = -e\frac{2}{(2\pi)^3}\int_{\text{all } \underline{K} \text{ space}}(f-f_o)\underline{v}\,d\underline{K} = \frac{e}{4\pi^3}\int_{\text{all } \underline{K} \text{ space}}\Phi\frac{\partial f_o}{\partial \mathcal{E}}\underline{v}\,d\underline{k} \qquad (2.31)$$

From equation (2.20), it follows that

$$\frac{\partial f_o}{\partial \mathcal{E}} = -f_o(1-f_o)/KT \qquad (2.32)$$

If the density of electrons in the conduction band is small enough so that $f_o \ll 1$, i.e., if the system is non-degenerate so that it may be described by classical Boltzmann statistics, equation (2.32) reduces to

$$\frac{\partial f_o}{\partial \mathcal{E}} = -f_o/KT \qquad (2.33)$$

and the current density is then given by

$$\underline{J} = \frac{-e}{4\pi^3}\cdot\frac{1}{KT}\int_{\text{all } \underline{k} \text{ space}}\underline{v}\Phi f_o\,dk \qquad (2.34)$$

To derive an expression for the drift mobility the magnetic field $\underline{B}$ is set equal to zero and the electric field $\underline{E}$ is assumed to be in the x- direction. The solution for Φ in this case is given by

$$\Phi = \frac{-e}{\hbar}\tau E_x\frac{\partial \mathcal{E}}{\partial k_x} = -e\tau E_x v_x \qquad (2.35)$$

substituting this value of Φ in equation (2.34) the current density in the x- direction becomes

$$J_x = \frac{e^2}{4\pi^3}\frac{E_x}{KT}\int\tau v_x^2 f_o\,d\underline{k} \qquad (2.36)$$

Since the density of carriers is given by

$$n = \frac{1}{4\pi^3}\int f_o\,d\underline{k} \qquad (2.37)$$

equation (2.36) can be written as $J_x = \frac{e^2}{4\pi^3} \frac{E_x}{KT} \cdot 4\pi^3 n \langle \tau v_x^2 \rangle$

$\therefore J_x = \frac{ne^2 E_x}{KT} \langle \tau v_x^2 \rangle$ (2.38) Since $J_x = -ne\mu_D E_x$

where μ_D is the drift mobility in the x- direction

$\therefore \mu_D = \frac{-e}{KT} \langle \tau v_x^2 \rangle$ (2.39)

Similar expressions follow for the rest of the components of the drift mobility tensor.

To derive an expression for the Hall mobility, external fields are assumed in the following forms:

$$\underline{E} = E_x \hat{x} + E_H \hat{y} \quad (2.40)$$

$$\underline{B} = B_z \hat{z} \quad (2.41)$$

With these fields equation (2.30) for ϕ becomes:

$$\phi = \frac{-e}{\hbar} \tau \left[E_x \frac{\partial \varepsilon}{\partial k_x} + E_H \frac{\partial \varepsilon}{\partial k_y} \right] + \frac{e^2}{\hbar^3} \tau B_z \Sigma_z \tau \left[E_x \frac{\partial \varepsilon}{\partial k_x} + E_H \frac{\partial \varepsilon}{\partial k_y} \right] \quad (2.42)$$

Substituting equation (2.42) in equation (2.34) for j, the y- component J_y is given by

$$J_y = \frac{e^2}{4\pi^3} \frac{1}{KT} \int \tau v_y \left(E_x v_x + E_H v_y \right) f_o \, d\underline{k} -$$

$$\frac{e^3}{4\pi^3 \hbar^2} \frac{B_z}{KT} \int \tau v_y \Sigma_z \left[\tau \left(E_x v_x + E_H v_y \right) \right] f_o \, d\underline{k} \quad (2.43)$$

Since $J_y = \sigma_{yx} E_x + \sigma_{yy} E_H$ (2.44)

and since for the configuration considered in Figure (2.1), in the steady state $J_y = 0$, eq.(2.43)leads to(2.45).

$$\frac{E_H}{E_x} = -\frac{\sigma_{yx}}{\sigma_{yy}} = \frac{-\langle \tau v_y v_x \rangle + \frac{eB_z}{\hbar^2} \langle \tau v_y \Sigma_z \tau v_x \rangle}{\langle \tau v_y^2 \rangle - \frac{eB_z}{\hbar^2} \langle \tau v_y \Sigma_z \tau v_y \rangle} \quad (2.45)$$

Since in the absence of a magnetic field, $J_y = 0$, the term $\langle \tau v_y v_x \rangle$ must be negligibly small. The second term in the denominator is a magneto-resistance term. This effect was measured by Frankevich and Sokolik.[5] They measured a variation in the photocurrent as large as 8% when anthracene crystals were placed in a megnetic field of 3 kilogauss. However, it is believed that this Frankevich effect is significant only for light intensities greater than 10^{18} photon/cm^2. sec. The effect was not reported for lower light intensities. This term introduces a quadratic term in the Hall mobility. In the range of magnitude of magnetic field where linear terms are dominant it is reasonable to neglect the second term in the denominator of equation (2.45).

From equation (2.15) the Hall mobility is given by $\mu_H = E_H / E_x B_z$, therefore equation (2.45) leads to

$$\mu_H = \frac{e}{\hbar^2} \frac{\langle \tau v_y \Omega_z \tau v_x \rangle}{\langle \tau v_y^2 \rangle} \qquad (2.46)$$

Also $$\sigma_{yx} = -\frac{e^3}{\hbar^2} \frac{B_z}{KT} \eta \langle \tau v_y \Omega_z \tau v_x \rangle \qquad (2.47)$$

expanding the operator Ω_z as defined by equation (2.28), the term $\langle \tau v_y \Omega_z \tau v_x \rangle$ becomes

$$\langle \tau v_y \Omega_z \tau v_x \rangle = \hbar^2 \langle \tau^2 (v_y v_x M^{-1}_{yx} - v_y^2 M^{-1}_{xx}) \rangle + \langle \tau v_y v_x \Omega_z \tau \rangle \qquad (2.48)$$

Where M^{-1}_{ij} is the symmetric effective mass tensor defined by

$$M^{-1}_{ij} = \frac{1}{\hbar^2} \left(\frac{\partial^2 E}{\partial k_i \partial k_j} \right) \qquad (2.49)$$

Two simplified models are usually considered for the dependence of τ on $\underline{k}$.

1. Constant relaxation time.

2. Constant mean free path.

When the first model is considered, namely constant τ, the second term in equation (2.48) vanishes and μ_H is then given by $\mu_H = e\tau \frac{\langle v_y v_x M^{-1}_{yx} - v_y^2 M^{-1}_{xx} \rangle}{\langle v_y^2 \rangle}$ (2.50)

If the second model is considered i.e. constant free path λ, τ is given by $\tau = \frac{\lambda}{|\underline{v}(\underline{k})|}$ (2.51)

The second term in equation (2.48) can now be expanded as follows:

$$\langle \tau v_y v_x \Omega_z \tau \rangle = \langle \tau v_y v_x \hbar \left(v_x \frac{\partial}{\partial k_y} - v_y \frac{\partial}{\partial k_x} \right) \tau \rangle$$

$$= \hbar \langle \tau v_y v_x \left(v_x \frac{\partial \tau}{\partial k_y} - v_y \frac{\partial \tau}{\partial k_x} \right) \rangle \quad (2.52)$$

equation (2.52) can be written as

$$\langle \tau v_y v_x \Omega_z \tau \rangle = \frac{\hbar}{2} \langle \frac{\partial}{\partial k_y} \left(\tau^2 v_y v_x^2 \right) - \frac{\partial}{\partial k_x} \left(\tau^2 v_x v_y^2 \right) \rangle -$$

$$\frac{\hbar}{2} \langle \tau^2 \frac{\partial}{\partial k_y} (v_y v_x^2) - \tau^2 \frac{\partial}{\partial k_x} (v_y^2 v_x) \rangle \quad (2.53)$$

On applying Green's theorem to the first term on the right side of equation (2.53) it vanishes, and the second term reduces to

$$\langle \tau v_y v_x \Omega_z \tau \rangle = \frac{\hbar^2}{2} \langle \tau^2 \left(v_y^2 M^{-1}_{xx} - v_x^2 M^{-1}_{yy} \right) \rangle \quad (2.54)$$

Substituting equation (2.54) in equation (2.48), the Hall mobility for a constant free path becomes

$$\mu_H = \frac{e}{2} \frac{\langle \tau^2 (2 v_y v_x M_{yx}^{-1} - v_y^2 M_{xx}^{-1} - v_x^2 M_{yy}^{-1}) \rangle}{\langle \tau v_y^2 \rangle} \qquad (2.55)$$

If a Hall current J_H, is to be measured, E_H is then zero and $J_H = J_y$.

The Hall mobility is then given by

$$\mu_H = J_H / J_x B_z \qquad (2.56)$$

The solution of the Boltzmann equation then leads to

$$J_H / J_x = \frac{\frac{-e}{\hbar^2} B_z \langle \tau v_y \Omega_z \tau v_x \rangle + \langle \tau v_x v_y \rangle}{\langle \tau v_x^2 \rangle - \frac{e}{\hbar^2} B_z \langle \tau v_x \Omega_z \tau v_x \rangle} \qquad (2.57)$$

On applying an analysis similar to the one used for Hall voltage the Hall mobility is then given by

$$\frac{\mu_H}{\mu_D} = -\frac{KT}{2} \frac{\langle \tau^2 (v_y^2 M_{xx}^{-1} + v_x^2 M_{yy}^{-1} - 2 v_y v_x M_{yx}^{-1}) \rangle}{\langle \tau v_x^2 \rangle \langle \tau v_x^2 \rangle} \qquad (2.58)$$

As shown from equations (2.58) and (2.55) μ_H For Hall voltage is in general not the same as μ_H for Hall current for an anisotropic material like anthracene.

The above equations for μ_H and μ_D can be applied to positive charge carriers i.e. holes if e is changed to $-e$ and the energy, $\mathcal{E}$, is changed to $-\mathcal{E}$.

References Chapter II

1. Kerson Huang, Statistical Mechanics/John Wiley & Sons, Inc., New York, London, Sydney/ Page 58.

2. Reference 1, Page 104.

3. H. Jones and C. Zener, PROC. ROY. SOC. A145 268 (1934)

4. C. Kittel, Introduction to Solid State Physics/ John Wiley & Sons, Inc., New York, London, Sydney/ Third edition, Page 174.

5. E.L. Frankevich and I.A. Sokolik, Soviet Physics Solid State 25, 790 (1967).

Chapter III

Measurement of linear compressibilities of anthracene and determination of a possible set of elastic constants

Evaluation of the drift and Hall mobilities as given by equations (2.39) and (2.55) requires knowledge of the band structure of anthracene, i.e. the dependence of the energy $\mathcal{E}$ on the wave vector $\underline{K}$. Since the averaging processes shown in these equations are performed over the first Brillouin zone it is necessary to know the geometry of this zone. Both the band structure and the first Brillouin zone depend on the lattice parameters of the anthracene crystal as will be shown in Chapter IV. If the mobilities are to be calculated as functions of pressure, the variation of the lattice parameters with pressure must be determined first.

There are two types of interactions in molecular crystals of aromatic compounds, e.g. anthracene. The atoms in a molecule are strongly coupled via covalent interactions (intramolecular interactions) and the molecules are held together with weak van der Waals interactions (intermolecular interactions). Obviously the intermolecular distances are shortened first under pressure. Because the intermolecular interactions are relatively weak, these crystals may be expected to be quite compressible in the pressure range up to 100 kilobars. Dispersion forces between conjugated π-

electron systems are anisotropic, therefore volume compressibility data are not enough to determine the linear compressibilities. Although these linear compressibilities can be calculated from the elastic constants in the linear approximation, the latter are only approximately known. Therefore direct experimental data on the linear compressibilities are necessary for these crystals.

For the sake of continuity this chapter is divided into two main sections as follows:

A. Experimental determinations of linear compressibilities of anthracene using neutron diffraction techniques. This section contains information necessary for the rest of the thesis.

B. Determination of a possible set of elastic constants which is consistent with the measured linear compressibilities.
This section involves further manipulation of the data and is independent of the rest of the thesis.

A. Experimental determination of the linear compressibilities of anthracene.

Experimental procedures and apparatus.

1. Purification of anthracene.

Measurements involving charge transport in anthracene require single crystals of high purity. Impurities and/or defects can act as charge trapping centers which may change the properties of this material.[1,2,3] High purity single crystals were prepared as follows, commercial grade synthetic anthracene (Eastman H480) was purified by vacuum sublimation and zone refining. All purification processes were performed under yellow "safe" lights to prevent photo-reactions from generating impurities. The major impurities in synthetic anthracene have been isolated and identified. These are anthraquinone, anthrone, bianthryl, and 9, 10-dihydroanthracene.[4]

Vacuum sublimation

Purification was started by vacuum sublimation. The apparatus used for this purpose was a combined sublimation and zone refining tube shown in Figure (3.1). 60 grams of synthetic anthracene were loaded into the left-hand bulb, the filling tube sealed, and the apparatus pumped down to a pressure that was less than 50 microns. The left-hand bulb was placed in a furnace, maintained at a temperature of 145° c, and the anthracene sublimed under continious evacuation into the second bulb. The most volatile impurities were pumped off and trapped.

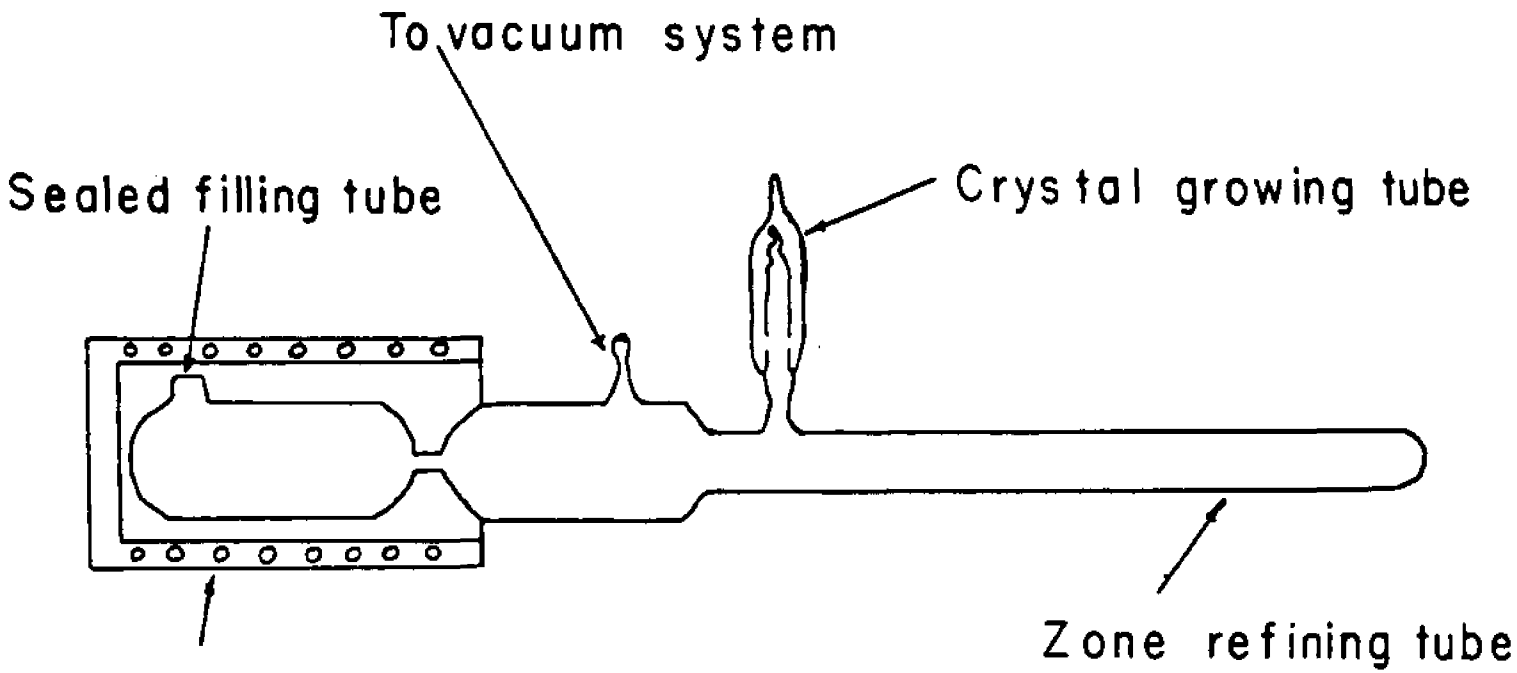

FIG. 3.1 Combination tube consisting of vacuum sublimation, zone refining and crystal growing vessels

When approximately 95% of the anthracene had passed over to the second bulb, the furance was turned off and the remaining 5% impure anthracene was sealed in the first bulb by melting the constriction between the first and second bulbs. The apparatus was flushed twice and filled to ½ atmosphere with pure nitrogen (research grade). The remaining bulb and zone refining tube were then sealed off from the vacuum system and the anthracene was melted into the zone refining tube and allowed to solidify from the lower end of the zone refining tube.

Zone refining

The next stage was zone refining. This was carried out on a Fisher zone refiner, shown in Figure (3.2) The refining was carried out in thick-walled, 20 mm, Pyrex tubing to reduce the possibility of breakage which could occur as a result of the large expansion on melting which is characteristic of organic compounds. Better segregation was obtained by the use of air coolers above the heaters to stabilize the width of the molten zone. Another precaution is to start zone melting at the free surface to avoid tube breakage. The presence of an inert gas in the tube prevented serious sublimation of anthracene up the tube. About 30 zones of ½" to 1" in length were passed down a 14" column at the rate of one inch per hour. The heaters were maintained at the lowest temperature that would permit the forma-

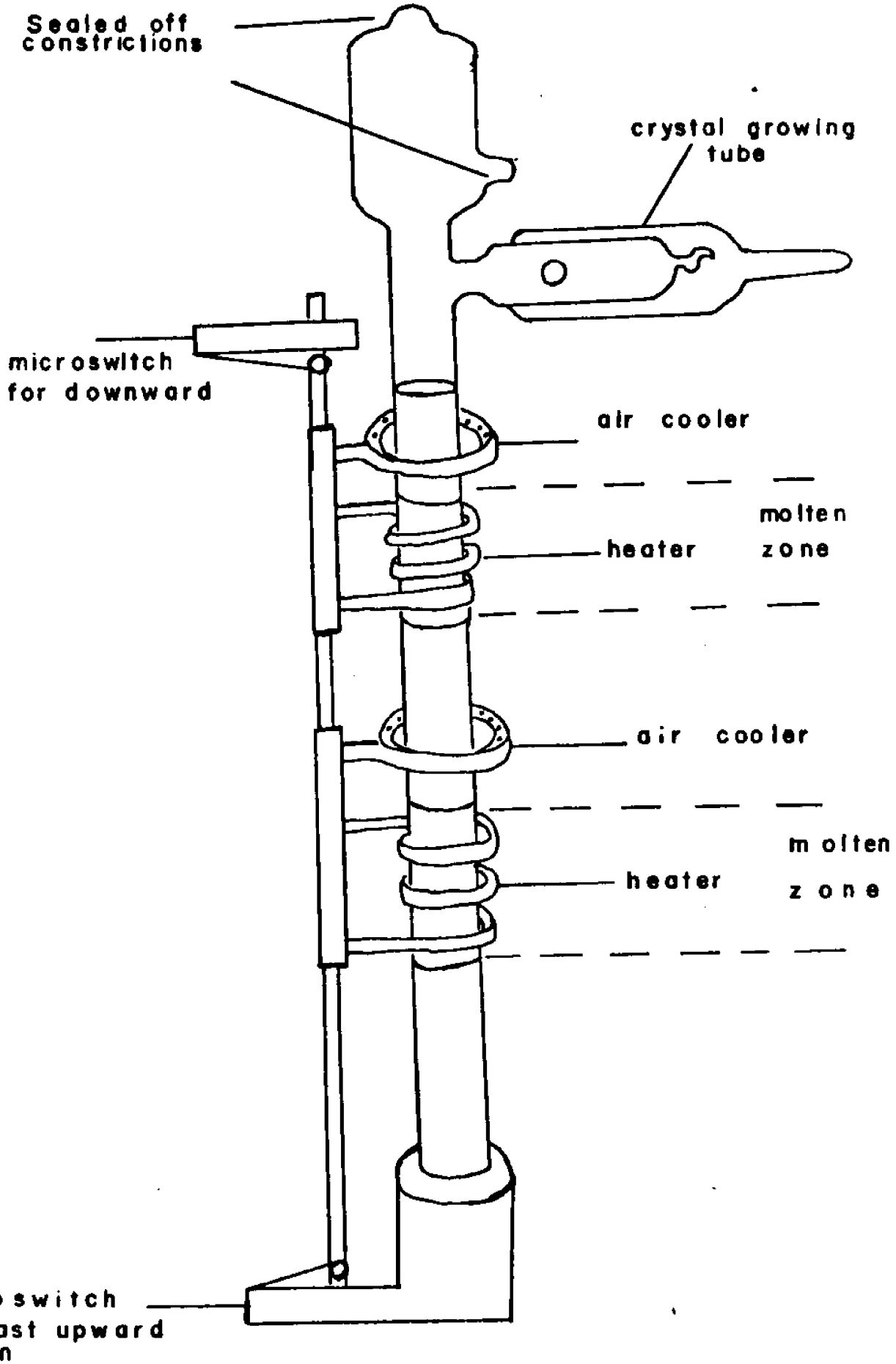

FIG.3.2 Zone refiner

tion of a good zone so that thermal decomposition could be minimized.

The most obvious change of the anthracene column during zone refining was the concentration of yellow anthraquinone together with some dark brown material at the lower end of the tube. Impurities which lower the freezing point of the host substance, anthracene, traveled with the molten zone, and tended to segregate at the bottom end of the anthracene column. These impurities have a segregation coefficient that is less than one. (The segregation coefficient is defined as the ratio of the impurity mole fraction in the solid to that in the liquid[5]). Impurities which raise the freezing point traveled in a direction opposite to the direction of motion of the molten zone and therefore tended to segregate at the top of the anthracene column. These impurities have a segregation coefficient that is greater than one. An impurity such as carbozole has a segregation coefficient that is approximately one and is therefore not efficiently removed by zone refining, however the synthetic anthracene used did not contain carbozole. When the zone refining was completed, the tube was cracked open and the upper and lower ends were rejected. The center portion of the anthracene column was then combined with a similar material and loaded into combined sublimation, zone refining, and crystal growing tubes. The material was then sublimed as before, and melted into the combined zone refining and crystal

growing tubes. The material was then zone refined. After this second zone refining, the top end of the column was melted into the empty sublimation bulb. The center portion of the column was then melted into the crystal growing tube which was then sealed off from the zone refining tube. In this way the transfer was effected without exposing the anthracene to atmospheric oxidation and the crystal was grown in the same atmosphere as used for the final zone refining.

2. Growth and quality of anthracene crystals.

Crystals were grown by the Bridgman method in which controlled cooling is carried out by slowly lowering the crystal growing tube at a rate of one inch per day through a vertical temperature gradient from the hot to the cold end[6]. A suitable temperature gradient was obtained by arranging two isothermal furnaces, as shown in Figure (3.3), such that the upper furnace was at 240°c and the lower furnace was at 205°c. (The melting point of anthracene is 217°c.)

A diagram of the crystal growing tube is shown in Figure (3.4). The tube was suspended in the furnace, as shown in Figure (3.5), so that the tip was just below the melting point isothermal, and the lowering mechanism was then turned on. Crystallization was begun by cooling the tip of t e tube. This prevented supercooling and the subsequent formation of multicrystals. As the

FIG.3.3 Crystal growing furnace

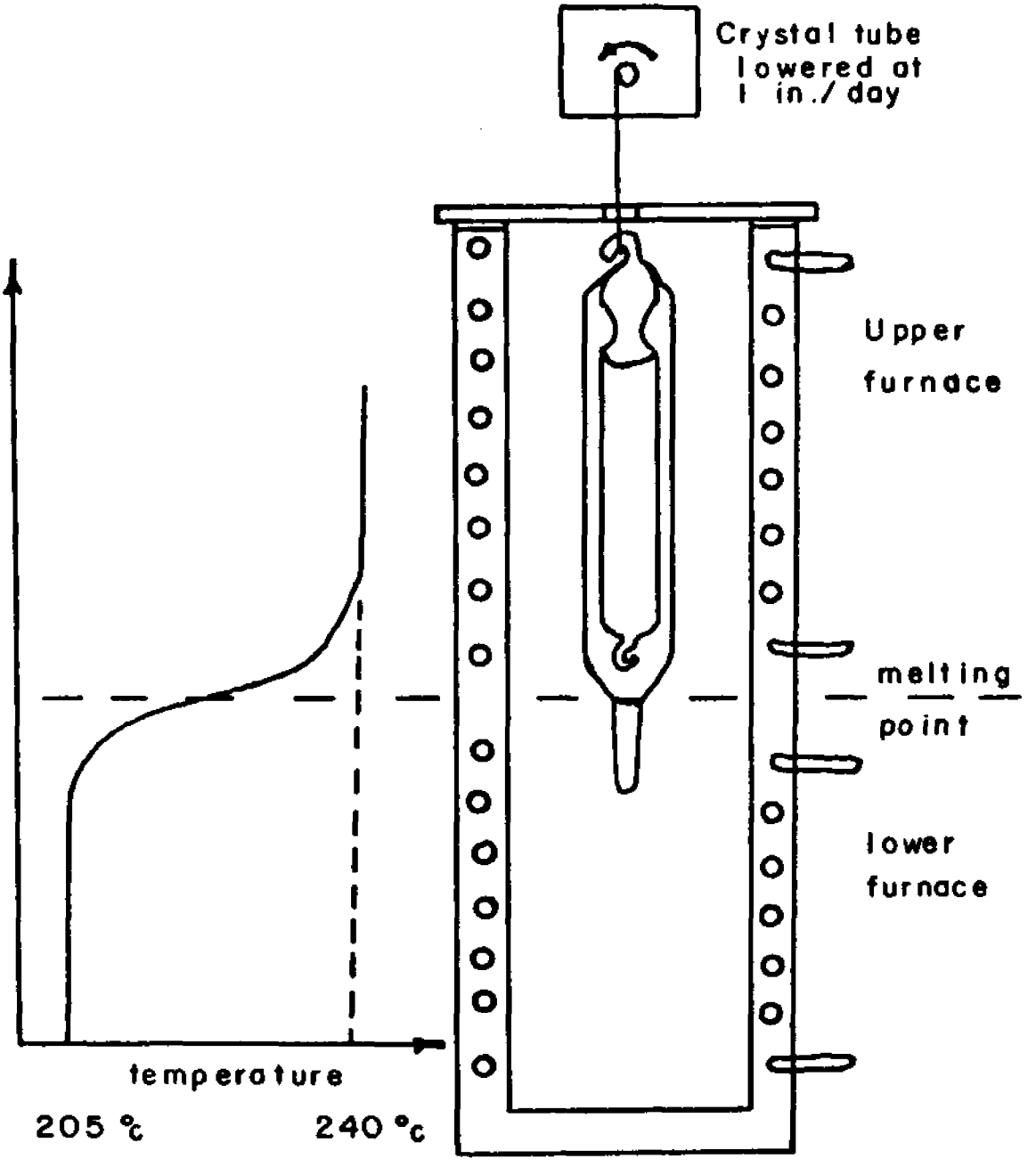

FIG. 3.4. Crystal growing tube

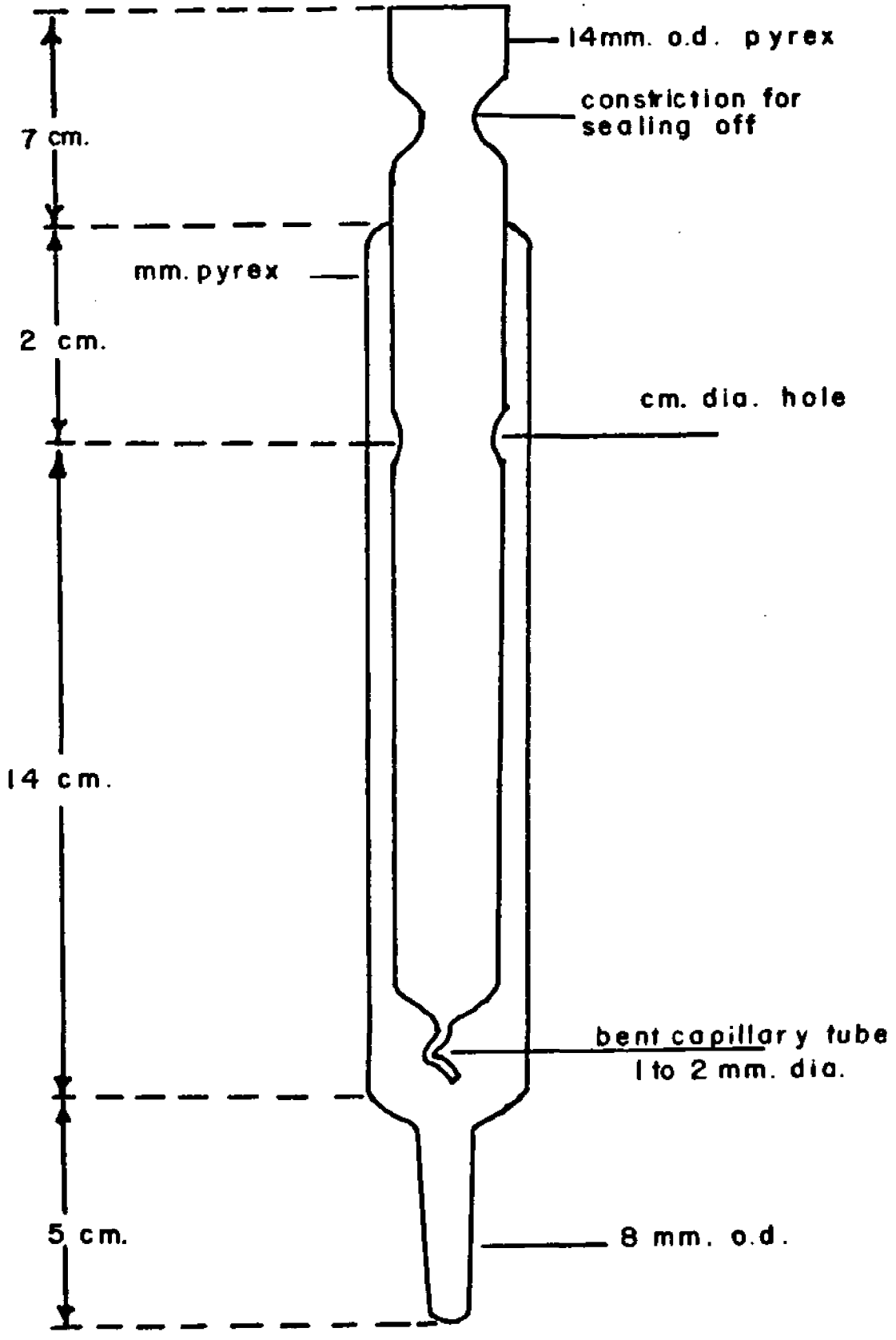

tube is lowered, crystallites grow until, just below the bent capillary, several large crystallites occupy the tube. The bent capillary inevitably selects a particular seed which grows into the upper tube as a large crystal. If the angle between the capillary and the tube axis is less than 45°, the a b cleavage plane will grow parallel to the tube axis. If the angle is greater than 45° it will grow perpendicular to the tube axis(7). When growth was complete, the crystal in the tube was removed from the lower furnace and allowed to cool rapidly for a few minutes to let the crystal break away from the tube wall. There was usually a cracking sound as this occurred. The crystal and the tube were then returned to the lower, annealing furnace and cooled to room temperature over a period of three days. After this period, the crystal tube was opened and the crystal boule was easily slid from the tube because the inside surface of the crystal growing tube had been treated with "Dow Corning 200" silicone release agent, dissolved in methyl ethyl ketone. After treatment, and before filling, the tube had been baked for one hour at 275°c. The release agent reacted chemically with the glass surface and when a crystal was grown, contamination of the crystal, due to the release agent, did not occur.

No impurities were eluted in a gas chromatography. Therefore, it was concluded that the total impurity content was less than 1 P.P.M. The final purity and structural defect concentration of the material was checked by the triplet lifetime which was found to be between 20 and 25 m. sec., equivalent to the longest which has been reported(8).

Cutting, orienting, and shaping a sample from a crystal boule.

A crystal boule usually had some cleavage cracks. Applying pressure with a razor blade in the direction of the crack readily cleaved the crystal apart. The cleavage face is the a b plane. The location of the a direction in the plane was obtained by a polarizing microscope(9) and checked by observation of the double refraction of the crystal(10). With this information and knowing the relative directions of the b and c′ directions(11), the crystal could be cut in any desired orientation of the a, b, or c′ directions Figure (3.5). After orientation, the crystal was cut with a string saw using xylene as a cutting medium. An optical finish was obtained by polishing the crystal on a glass slide covered with a "Kleenex" tissue, soaked in xylene.

FIG. 3.5. Orientation of an anthracene crystal by double refraction

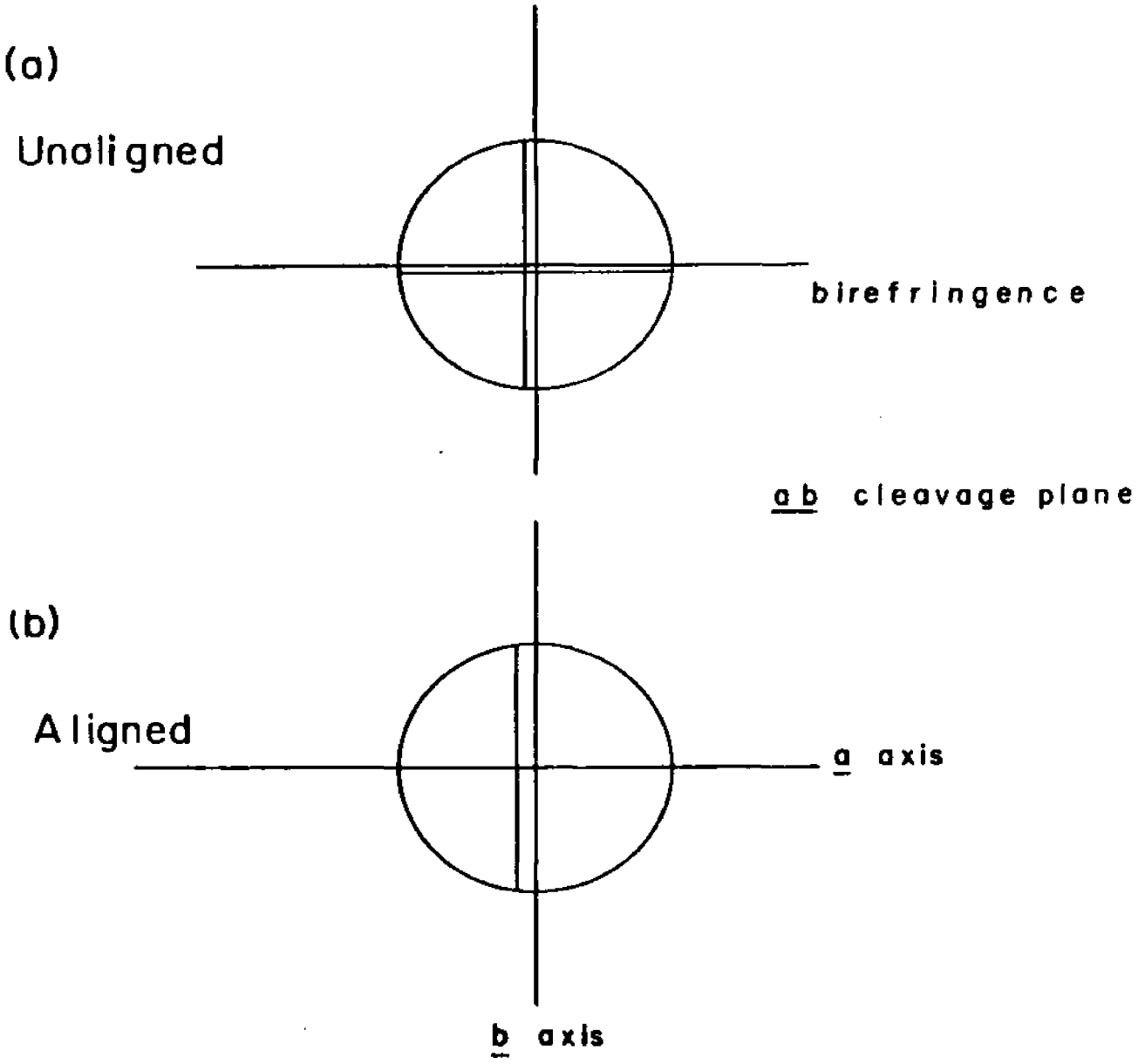

Neutron diffraction experiment:

This experiment was performed at the High Flux Beam reactor of Brookhaven National Labotatory. A monochromatic beam of neutrons of wavelength 2.4609 A was Bragg reflected off a single crystal of anthracene. The beam was obtained from the (002) reflection of a pyrolytic graphite monochromator[12,13]. The half wavelength component was essentially removed by means of a pyrolytic graphite filter. The Bragg angles of reflection were measured with a precision of 0.02°. Two samples in the shape of a rectangular parallelopiped were used. The dimensions of the samples were 2x3x6 mm and 2x6x3 mm in the $\underline{c}'\underline{x}\underline{a}\underline{x}\underline{b}$ directions respectively.

A gas pressure system using helium as a pressure transmitting medium was used. The system consisted mainly of two sections, a low pressure section, and a high pressure one.

A two stage air-operated compressor was used to pump the whole system up to two kilobars (American Instruments Company No. # 46 - 14021). The pressure in this range was measured by a Heise dial gauge which was also used to calibrate a manganin wire resistor whose resistance varies linearly with hydrostatic pressure in the pressure range of interest in this experiment. The resistance was measured by a d.c. bridge.

Above two kilobars the low pressure section was isolated by means of a high pressure valve. An Enerpac oil hand pump was then used to pump up the piston of a pressure intensifier which has a ratio of 1 to 15 (Harwood Engineering Company, Inc., No. A 2.5J Laboratory type intensifier for gas service to 200,000 P.S.L.). The high pressure section was thus raised from two kilobars to a final pressure up to 5.4 kilobars. The pressure in this range was measured by the variation of the resistance of the manganin wire resistor. An aluminum cell with a cylindrical vertical bore was used as a sample chamber. The cell was bolted to the tray of the neutron diffraction spectrometer.

Procedure.

A computer program using the published values of the lattice parameters of anthracene[14] determined the approximate positions and intensities of the different Bragg reflections. The strong ones, namely, (020), (200), and (003) were selected for measurement. The variations of the lattice parameters with pressure were determined from the shift of the Bragg reflection angles with pressure.

Results

Figures (3.6 - 3.9) show the lattice parameters a, b, c, and β of anthracene as functions of pressure up to 5.4 kilobars. It is clear from the figures that up to this pressure the parameters are linear with pressure.

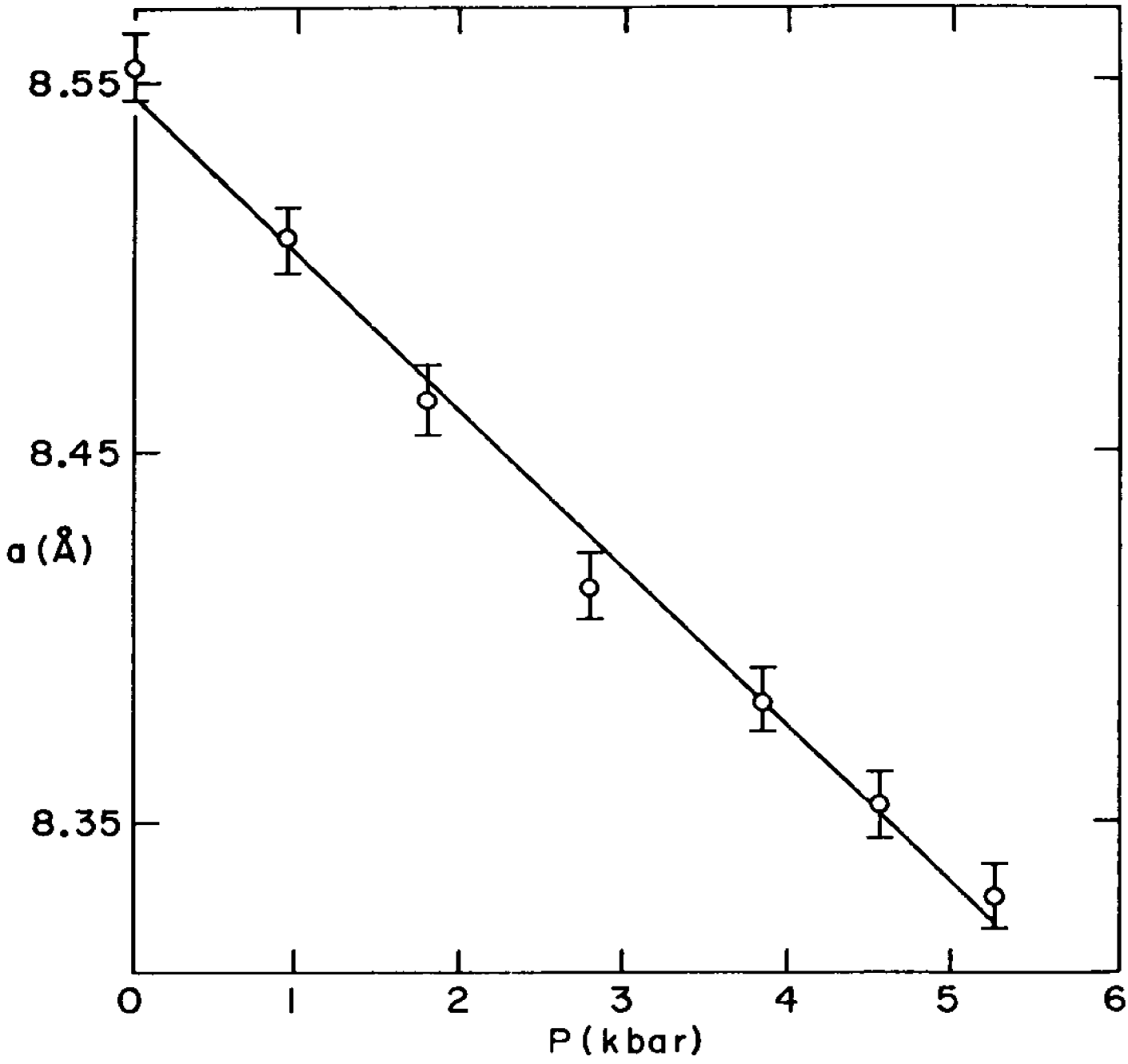

FIG. 3.6

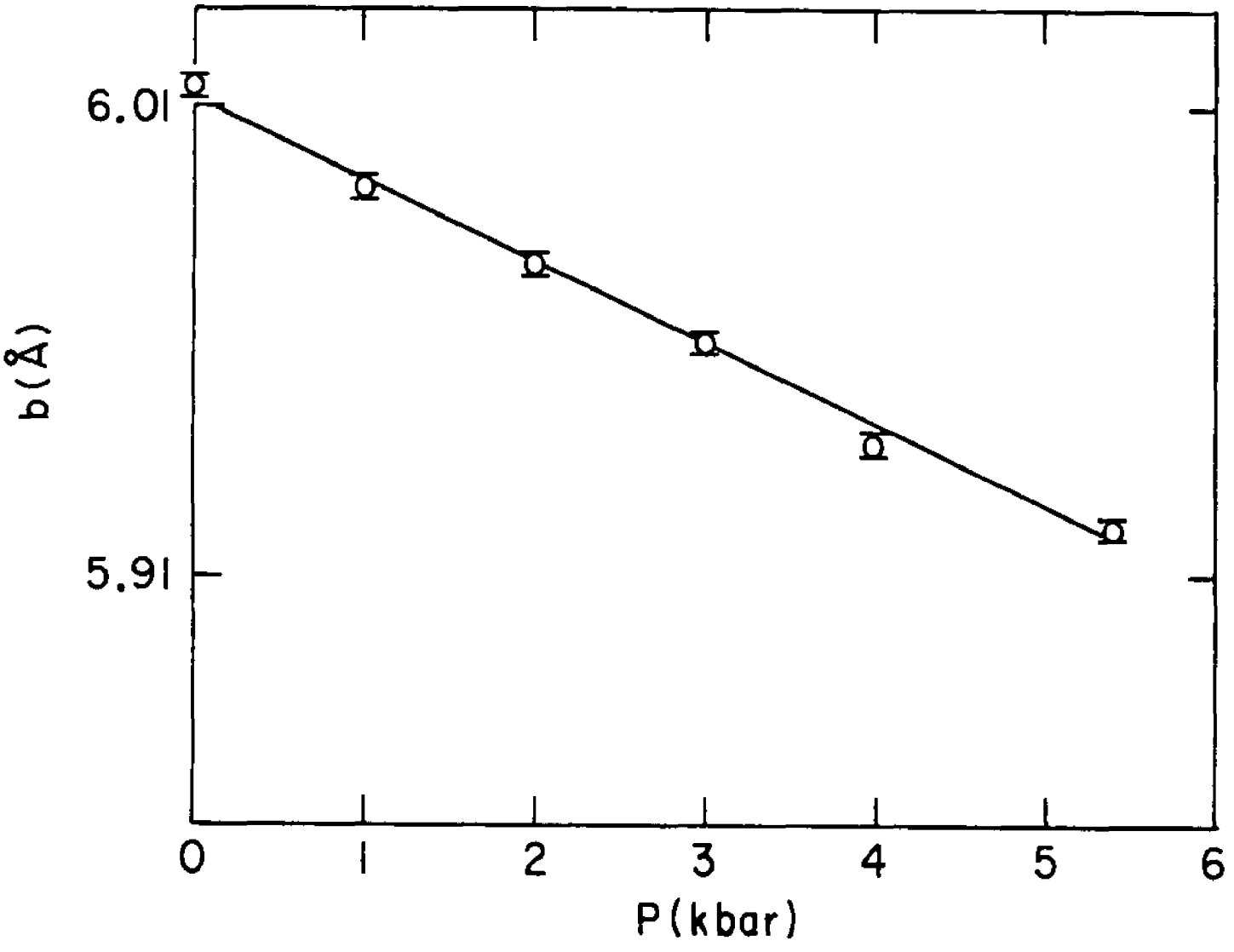

FIG 3.7

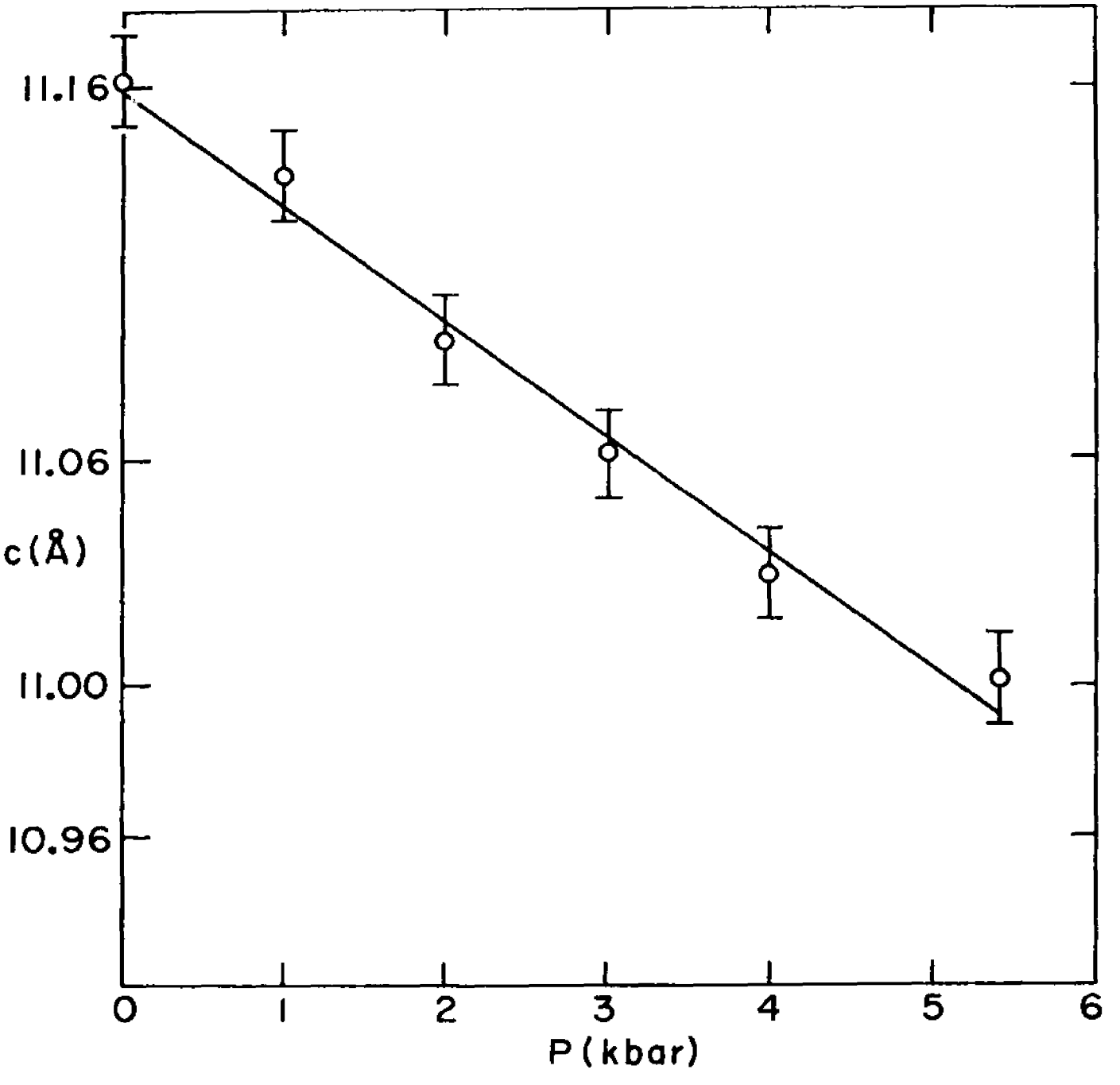

FIG. 3.8

FIG. 3.9

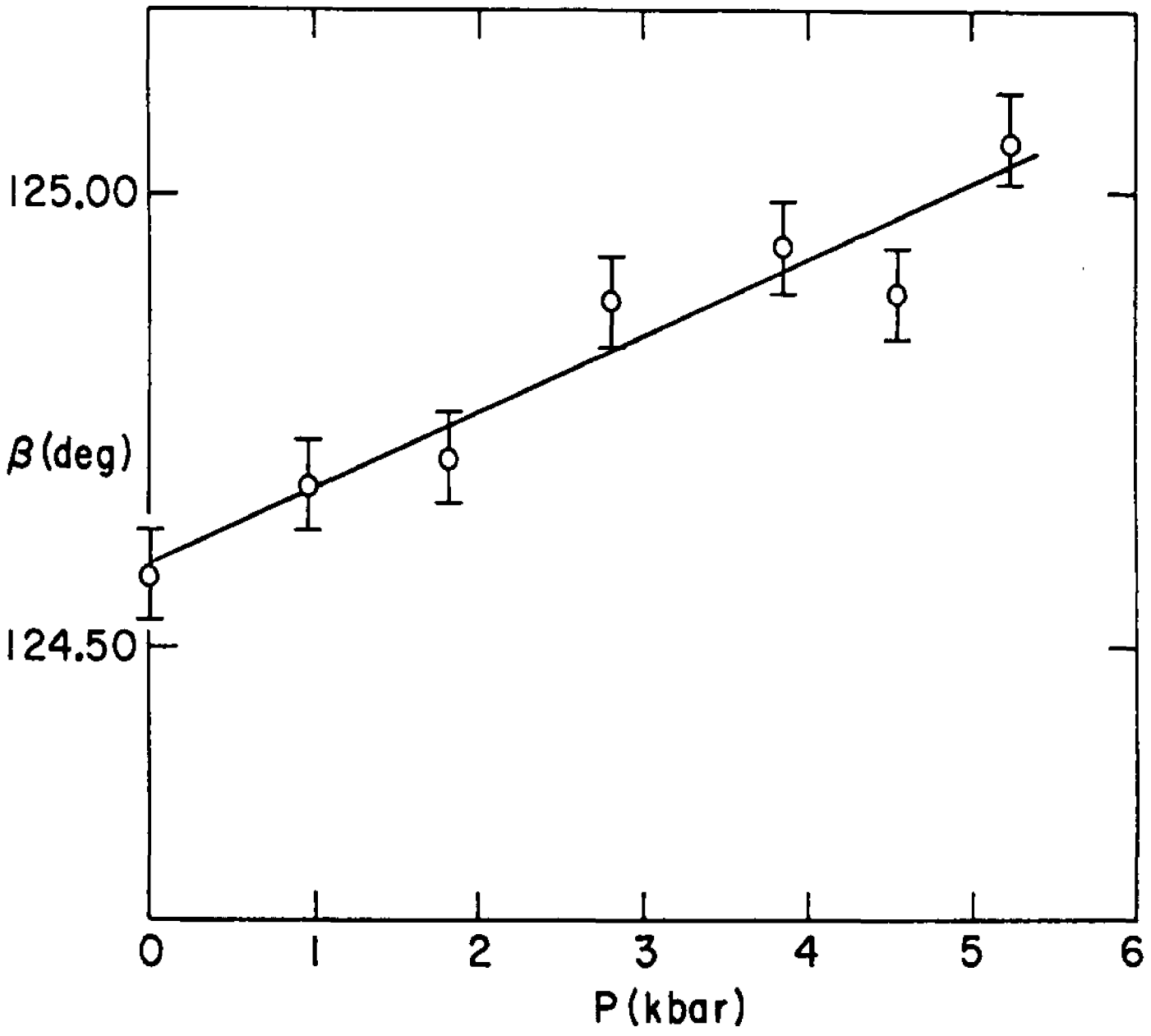

The data were therefore fitted to straight lines using the least squares method. The equations of these best lines are as follows:

$$a = 8.546(1-.00496P) \quad \text{A} \quad (3.1)$$

$$b = 6.011(1-.00286P) \quad \text{A} \quad (3.2)$$

$$C = 11.162(1-.00277P) \quad \text{A} \quad (3.3)$$

$$\beta = 124.59(1+.00067P) \quad \text{degress} \quad (3.4)$$

where P is in kilobars.

From the above equations it can be noted that the linear compressibility along b is very close in magnitude to that along c and about half that along a. The volume of the unit cell is given by

$$V = abc\sin(\beta) \quad (3.5)$$

For small changes in the lattice parameters the fractional change in volume is given by

$$\frac{\Delta V}{V} = \frac{\Delta a}{a} + \frac{\Delta b}{b} + \frac{\Delta c}{c} + \Delta\beta\ \cot(\beta) \quad (3.6)$$

Fig. (3.10) shows the percentage variations in a, b, c, β as well as v as functions of pressure.

Comparison with previous data.

The most recent measurement of the volume compressibility of anthracene was done by Vaidya and Kennedy[15]. Their results show a change of volume of 5.5% at 5 kilobars and the value calculated from this work is 5.8% in fairly good agreement. Rice and Jortner[16] noticed that the volume compressibility data of a number of aromatic

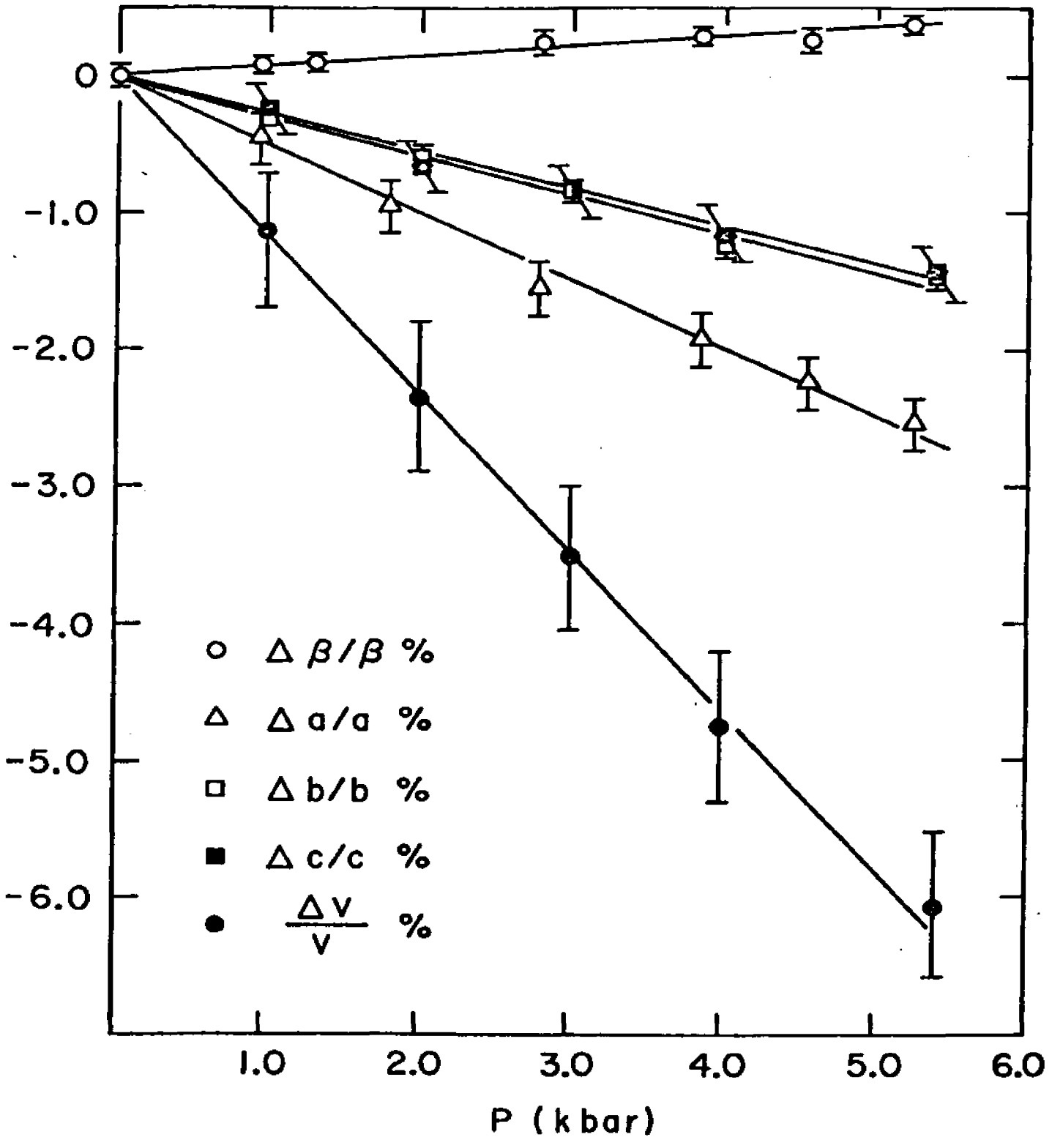

FIG. 3.10

crystals (i.e. naphthalene, anthracene, biphenyl, terphenyl, and substituted benzenes) as measured by Bridgman[17] and by Kabalinka[18] do not differ from one compound to the other by more than 20% up to 50 kilobars. That led them to construct an approximate unified volume compressibility pressure curve for a generalized molecular crystal of aromatic molecules. They also used these generalized data together with the data of linear compressibilities of linear polyphenyls as measured by Kabalinka[18] to construct a general linear compressibility curve for a model monoclinic crystal. Table 3.1 summarizes the above results.

From table 3.1 it can be noticed that the volume compressibility calculated from this work is in good agreement with all previous data. The linear compressibilities of anthracene in the a and b directions are slightly smaller but very close to those introduced by Rice et al (within 10%). The linear compressibility of anthracene in the c direction is almost 40% larger than that of Rice et al. However, we would like to point out here that even the linear polyphenyls upon which Rice et al based their model differ in their linear compressibility in the c direction. Therefore, we conclude that the available data justify speaking of general linear compressibilities for a model monoclinic crystal in the a and b directions but not in the c direction.

Table 3.1

Linear and volume compressibility data of anthracene.

		anthracene		biphenyl	terphenyl	quaterphenyl
		5 kilo-bars	10 kilo-bars	10 kilo-bars	10 kilo-bars	10 kilo-bars
Vaidya et al	$\Delta v/v$	.055	.091			
Bridg-man	$\Delta v/v$	.057	.09			
Kaba-linka	$\Delta a/a$			.054	.054	.054
	$\Delta b/b$			.030	.030	.030
	$\Delta c/c$			.022	.014	.005
	$\Delta v/v$		.083	.106	.098	
Rice et al	$\Delta a/a$		.054			
	$\Delta b/b$		.030			
	$\Delta c/c$		.020			
	$\Delta\beta/\beta$		–			
	$\Delta v/v$		.095			
This work	$\Delta a/a$	.0248				
	$\Delta b/b$	.0143				
	$\Delta c/c$	.0139				
	$\Delta\beta/\beta$	.0034				
	$\Delta v/v$	.058				

B. A possible set of elastic constants of anthracene.

The linear compressibilities of anthracene can in principle be calculated from the elastic constants in the linear approximation, as will be shown later. Three sets of elastic constants of anthracene have been deduced experimentally by Afanaseva et al[19], Huntington et al[20], and Danno et al[21]. In all cases the ultrasonic velocities were measured along specified directions and the elastic constants were obtained by solving the Christoffel equations[20].

This procedure involves both experimental limitions in measuring velocities e.g. high attenuation, small specimen size, inhomogenities in the material, transit time correction, as well as computational errors in calculating the elastic constants. Huntington et al[20] have stated that the velocity measurements have only a marginal accuracy of, at best about 2%, often considerably worse. The propagation of random errors affect some constants more than others, depending on the data reduction procedure. A fourth set of elastic constants was derived by Pawley[22] using the atom - atom potential model proposed by Kitaigorodskii[23].

In the next two sections we first show how the linear compressibilities are calculated from the elastic constants and then we discuss a trial to improve the available values of some of the constants using the ex-

perimental values of the linear compressibilities.

Calculation of the linear compressibilities from the elastic constants in the linear approximation.

Hooke's law when applied to an anisotropic material takes the form

$$\epsilon_{ij} = S_{ijk\ell}\sigma_{k\ell} \qquad (i,j,k,\ell = 1,2,3) \qquad (3.7)$$

where ϵ_{ij} are the components of the second rank strain tensor, $\sigma_{k\ell}$ are the components of the second rank stress tensor, and $S_{ijk\ell}$ are the components of the fourth rank compliance tensor. There are 9 equations of the form (3.7) for different values of i and j. Each equation has nine terms corresponding to different values of k and l. The tensor S therefore has 81 components. If equations (3.7) are solved for the stress components equations (3.8) are obtained

$$\sigma_{ij} = C_{ijk\ell}\epsilon_{k\ell} \qquad (3.8)$$

where the 81 $C_{ijk\ell}$ are the components of the fourth rank stiffness tensor.

The $C_{ijk\ell}$ and the $S_{ijk\ell}$ obey the following symmetry conditions:

$$S_{ijk\ell} = S_{jik\ell} \qquad (3.9)$$

$$S_{ijk\ell} = S_{ij\ell k} \qquad (3.10)$$

$$C_{ijk\ell} = C_{jik\ell} \qquad (3.11)$$

$$C_{ijk\ell} = C_{ij\ell k} \qquad (3.12)$$

Equations 3.9 - 3.12 reduce the number of independent components of S_{ijkl} and C_{ijkl} to 36 components each.

The matrix notation.

The symmetry of S_{ijkl} and C_{ijkl} in the first two and last two suffixes makes it possible to use the matrix notation as shown below. Both the stress components and the strain components are written with a single suffix running from 1 to 6:

$$\begin{bmatrix} \sigma_{11} & \sigma_{12} & \sigma_{13} \\ \sigma_{21} & \sigma_{22} & \sigma_{23} \\ \sigma_{31} & \sigma_{32} & \sigma_{33} \end{bmatrix} = \begin{bmatrix} \sigma_1 & \sigma_6 & \sigma_5 \\ \sigma_6 & \sigma_2 & \sigma_4 \\ \sigma_5 & \sigma_4 & \sigma_3 \end{bmatrix} \qquad (3.13)$$

and

$$\begin{bmatrix} \epsilon_{11} & \epsilon_{12} & \epsilon_{13} \\ \epsilon_{21} & \epsilon_{22} & \epsilon_{23} \\ \epsilon_{31} & \epsilon_{32} & \epsilon_{33} \end{bmatrix} = \begin{bmatrix} \epsilon_1 & \frac{1}{2}\epsilon_6 & \frac{1}{2}\epsilon_5 \\ \frac{1}{2}\epsilon_6 & \epsilon_2 & \frac{1}{2}\epsilon_4 \\ \frac{1}{2}\epsilon_5 & \frac{1}{2}\epsilon_4 & \epsilon_3 \end{bmatrix} \qquad (3.14)$$

In the S_{ijkl} and C_{ijkl} the first two suffixes are abbreviated into a single one running from 1 to 6, and the last two are abbreviated in the same way, according to the following scheme;

Tensor notation	11	22	33	23,32	13,31	12,21
Matrix notation	1	2	3	4	5	6

At the same time factors of 2 and 4 are introduced as follows,

$S_{ijkl} = S_{mn}$ when both m and n are 1,2, or 3,

$2S_{ijkl} = S_{mn}$ when either m or n are 4,5,or 6,

$4S_{ijkl} = S_{mn}$ when both m and n are 4, 5, or 6.

Now consider equation (3.7) written out for ϵ_{11} and ϵ_{23}:

$$\epsilon_{11} = S_{1111}\sigma_{11} + S_{1112}\sigma_{12} + S_{1113}\sigma_{13} + S_{1121}\sigma_{21} + S_{1122}\sigma_{22} + S_{1123}\sigma_{23} + S_{1131}\sigma_{31} + S_{1132}\sigma_{32} + S_{1133}\sigma_{33}$$

$$\epsilon_{23} = S_{2311}\sigma_{11} + S_{2312}\sigma_{12} + S_{2313}\sigma_{13} + S_{2321}\sigma_{21} + S_{2322}\sigma_{22} + S_{2323}\sigma_{23} + S_{2331}\sigma_{31} + S_{2332}\sigma_{32} + S_{2333}\sigma_{33}$$

In the matrix notation these two equations become:

$\epsilon_1 = S_{1j}\sigma_j$ and $\epsilon_4 = S_{4j}\sigma_j$

In general, therefore, equation (3.7) takes the shorter form

$$\epsilon_i = S_{ij}\sigma_j \qquad (i,j = 1,2,\ldots 6) \qquad (3.15)$$

The reason for introducing the 2's and 4's into the definitions of the S_{ij} is to avoid the appearance of 2's and 4's in equation (3.15) and to make it possible to write this equation in a compact form.

For the C_{ijkl} no factors of 2 or 4 are necessary. For if we simply write $C_{ijkl} = C_{mn}$ $(i,j,k,l = 1,2,3; m,n = 1,2,\ldots 6)$ it may be shown that equations (3.8) take the form

$$\sigma_i = C_{ij}\epsilon_j \qquad (i,j = 1,2,\ldots 6) \qquad (3.16)$$

Therefore in this notation the arrays of S_{ij} and C_{ij} are 6x6 matrices while (σ_i) and (ϵ_i) are 6x1 column matrices. It should be pointed out here that, in spite of their appearance with two suffixes, the S_{ij} and C_{ij} are not components, and so do not transform like the components, of a second rank tensor. To transfer them to other axes it is necessary to go back to the tensor notation.

The effect of crystal symmetry

The presence of symmetry in the crystal reduces still further the number of independent S_{ij} and C_{ij}. In the case of monoclinic crystals like anthracene symmetry elements reduce the number of independent components in each of (S_{ij}) and (C_{ij}) to 13 components. The arrays of S_{ij} and C_{ij} therefore are written out as follows

$$\begin{bmatrix} S_{11} & S_{12} & S_{13} & 0 & S_{15} & 0 \\ S_{21} & S_{22} & S_{23} & 0 & S_{25} & 0 \\ S_{31} & S_{32} & S_{33} & 0 & S_{35} & 0 \\ 0 & 0 & 0 & S_{44} & 0 & S_{46} \\ S_{51} & S_{52} & S_{53} & 0 & S_{55} & 0 \\ 0 & 0 & 0 & S_{64} & 0 & S_{66} \end{bmatrix} \quad \text{and} \quad \begin{bmatrix} C_{11} & C_{12} & C_{13} & 0 & C_{15} & 0 \\ C_{21} & C_{22} & C_{23} & 0 & C_{25} & 0 \\ C_{31} & C_{32} & C_{33} & 0 & C_{35} & 0 \\ 0 & 0 & 0 & C_{44} & 0 & C_{46} \\ C_{51} & C_{52} & C_{53} & 0 & C_{55} & 0 \\ 0 & 0 & 0 & C_{64} & 0 & C_{66} \end{bmatrix} \tag{3.17}$$

From equations (3.15) and (3.16) it is clear that the matrix (S_{ij}) is equal to the matrix $(C_{ij})^{-1}$ which is the inverse of the matrix (C_{ij}).

Further restrictions on the constants.

The work necessary to produce a strain ϵ_i, called the strain energy, is

$$\frac{1}{2} C_{ij} \epsilon_i \epsilon_j \tag{3.18}$$

This energy must be positive, for otherwise the crystal would be unstable. This means that the quadratic form (3.18) must be positive definite, that is, greater than zero for all real values of the ϵ_i unless all ϵ_i are zero. This implies further restrictions on the S_{ij} and C_{ij}.

The sufficient conditions that the strain energy is positive are(24)

$$P_m = \begin{vmatrix} c_{11} & \cdots & c_{1m} \\ \vdots & & \\ c_{m1} & & c_{mm} \end{vmatrix} > 0 \quad \text{for all } m \leq 6 \qquad (3.19)$$

Volume and linear compressibilities.

Volume compressibility.

We first calculate the proportional decrease in volume of a crystal when subjected to unit hydrostatic pressure, i.e., its volume compressibility. In equation (3.7) σ_{kl} is substituted as $-P\delta_{kl}$. Then

$$\epsilon_{ij} = -P s_{ijkl}\delta_{kl} = -P s_{ijkk} \qquad (3.20)$$

The dilation Δ is given by

$$\Delta = \frac{\Delta V}{V} = \epsilon_{ii} = -P s_{iikk} \qquad (3.21)$$

The volume compressibility is $-\frac{\Delta}{P}$ and is therefore equal to s_{iikk}.

Linear compressibilities.

Under hydrostatic pressure P the stretch of a line in the direction of a unit vector with direction cosines l_i is

$$\epsilon_{ij} l_i l_j = -P s_{ijkk} l_i l_j \qquad (3.23)$$

The linear compressibility, $\frac{\epsilon_{ij} l_i l_j}{-P}$, is therefore

$$\alpha = s_{ijkk} l_i l_j \qquad (3.24)$$

For a monoclinic crystal the direction cosines of the crystal axes are as follows

$$\begin{aligned} \hat{a} &\equiv (1,0,0) \\ \hat{b} &\equiv (0,1,0) \\ \hat{c} &\equiv (\cos(\beta), 0, \sin(\beta)) \end{aligned} \qquad (3.25)$$

The linear compressibilities along the crystal axes, written in the matrix notation, are therefore given by

$$\alpha|_{\underline{a}} = S_{11} + S_{12} + S_{13}$$

$$\alpha|_{\underline{b}} = S_{12} + S_{22} + S_{23}$$

$$\alpha|_{\underline{c}} = (S_{11}+S_{12}+S_{13})\cos^2(\beta_0) + (S_{13}+S_{23}+S_{33})\sin^2(\beta_0) + (S_{15}+S_{25}+S_{35})\sin(\beta_0)\cos(\beta_0) \qquad (3.26)$$

Where β_0 is the atmospheric pressure value of the monoclinic angle β .

β under hydrostatic pressure is given by

$$\cos(\beta) = \frac{(\underline{a}+\Delta\underline{a})\cdot(\underline{c}+\Delta\underline{c})}{|\underline{a}+\Delta\underline{a}||\underline{c}+\Delta\underline{c}|} \qquad (3.27)$$

If the cosine is expanded up to the linear term and the right side of equation (3.27) is also expanded up to linear terms in the strains, equation (3.27) leads to

$$\Delta\beta \equiv \beta-\beta_0 = P\left[(S_{11}+S_{12}+S_{13})\sin(\beta_0)\cos(\beta_0) - (S_{13}+S_{23}+S_{33})\sin(\beta_0)\cos(\beta_0) + (S_{15}+S_{25}+S_{35})\sin^2(\beta_0)\right] \qquad (3.28)$$

Where $(S_{ij}) = (C_{ij})^{-1}$ as shown before. Equations (3.26) and (3.28) summarize the procedure of calculating the change of the parameters a, b, c, and β with pressure from the elastic constants in the linear approximation. This procedure is very well justified since the experimental data presented in this work indicate a linear dependence of the lattice parameters on pressure up to 5.4 kilobars. For reference purposes equations (3.26) and (3.28) are rewritten in Table 3.2.

Table 3.2

Lattice parameters are written in the form

$x = x_o(1-\alpha p)$

parameter	pressure coefficient α
crystal axis a	$S_{11} + S_{12} + S_{13}$
crystal axis b	$S_{12} + S_{22} + S_{23}$
crystal axis c	$(S_{11} + S_{12} + S_{13})\cos^2(\beta_o) + (S_{13} + S_{23} + S_{33})\sin^2(\beta_o)$ $+ (S_{15} + S_{25} + S_{35})\sin(\beta_o)\cos(\beta_o)$
monoclinic angle β	$-\frac{1}{\beta_o}\left[(S_{11} + S_{12} + S_{13})\sin(\beta_o)\cos(\beta_o) - (S_{13} + S_{23} + S_{33})\sin(\beta_o)\cos(\beta_o) + (S_{15} + S_{25} + S_{35})\sin^2(\beta_o)\right]$

Table 3.3 shows the values of the pressure coefficients as calculated from the four sets of elastic constants available (19,20,21,22).

Table 3.3 lattice parameters are written as $\chi = \chi_0(1-\alpha P)$ where P is in kilobars.

Parameter	Pressure Coefficients α in (Kilobar) $^{-1}$				
	Afanaseva	Huntington	Danno	Pawly	This Work
a axis	.0084	.025	.0127	.0099	.00496
b axis	.0041	.0013	.0044	.00	.00286
c axis	.0002	.018	-.0024	.0037	.00277
Angle β	-.00228	.013	-.0040	-.00007	-.00067

As can be seen from table 3.3 none of the four sets predicts the correct values of the pressure coefficients as given in this work. This is not a surprising result because of the errors involved in the deductions of these sets. From equation (3.15) it can be seen that the three constants C_{44}, C_{46}, C_{66} are not involved in the calculation of the linear compressibilities, consequently the results of this work cannot be used to improve them. However these three constants are determined directly from the square of the measured velocities, therefore the percentage errors involved in them are only double those of the velocities.

The results of Afanaseva et al and Huntington et al agree on these three constants to within 6%. The values of Danno, however, are different by as much as 25% from the other two sets. Since Danno does not mention

anything about the accuracy of his measurements and since his set predicts a large expansion in the c- axis with pressure, we base our discussion on the sets determined by Afanaseva et al and Huntington et al.

It is therefore fair to assume that the three constants C_{44}, C_{46}, and C_{66} as given by Afanaseva et al are accurate to within 6%. C_{22} is also determined directly, therefore it should have a comparable accuracy. C_{33} and C_{35} do not differ by more than 17%. C_{11} differs by less than 20% and C_{55} by less than 30%. It is important to note that in the data reduction procedure followed by Huntington et al[20] the quantity which is determined more directly is $C_{11} + C_{55}$ and this sum does not differ by more than 5%.

The precision of the other constants namely C_{12}, C_{13}, C_{15}, C_{25}, and C_{23} is not known due to the propagation of errors throughout the computation. Based on the previous observations we assume C_{22} to be accurate to within 6%. C_{11}, C_{33}, C_{55}, and C_{35} were assumed to be accurate to $\pm$ the difference in their values from one experimental set to the other.

A computer scan of the values of the elastic constants was done on this basis while varying C_{15}, C_{25}, C_{12}, C_{13}, and C_{23} within wider limits in a trial to find a set which predicts the linear compressibilities correctly. The closest set to the experimental values of Afanaseva et al, which gave the correct linear compressibilities is given in the last column of table 3.4. It is to be noted that variation of C_{15} from 0 to -0.32 and C_{25} from -0.6 to $\pm$1.2 results in a change of about 10% in the

Table 3.4 Elastic Constants of anthracene.

	Huntington	Afanseva	Danno	Pawley	This Work
C_{11}	7.2	8.52	8.92	7.9	8.977
C_{22}	11.6	11.70	13.8	13.1	12.470
C_{33}	17.2	15.22	17.0	16.7	15.011
C_{44}	2.7	2.72	2.42	3.1	-
C_{46}	*1.3	1.38	1.14	1.0	-
C_{66}	4.2	3.99	3.16	2.5	-
C_{55}	3.6	2.82	2.84	4.6	2.811
C_{35}	-1.6	-1.87	-2.88	-4.9	-1.605
C_{12}	$\sim$ 4	6.72	4.63	7.3	9.82
C_{13}	3.3	5.9	4.49	5.9	6.99
C_{15}	3.3	-1.92	-2.58	-.20	-.125
C_{25}	$\sim$ 0	-1.7	-2.59	1.4	-.476
C_{23}	$\sim$ 8	3.75	8.44	5.6	4.144

C's are given in units of 10^{10} dyne/cm^2

* A sign mistake in one of the Christoffel equations results in a wrong minus sign. The correct sign gives 1.3.

compressibilities. We would also like to point out that C_{15} as given by this work is fairly close to the value calculated by Pawly [21]. Although Huntington et al gave positive and zero values for C_{15} and C_{25} respectively, they indicated that the value given for C_{25} is just an estimate and that C_{25} is probably negative. They also mentioned that the difficulty in determining the sense of one of their axes may result in an ambiguity in the sign of C_{15}, in addition the relative error in the sum $C_{15} + C_{35}$ is large since it involves the cancellation of 85% between large terms. It was because of these reasons that the scan was done around the values given by Afanaseva et al since their set gave better vales of the compressibilities to start with.

We would finally like to point out that because the standard deviations in the experimental values of the constants are not known it was not possible to have a quantitative measure of the closeness of the system given in this work to the experimental ones. This had to be judged by inspection. As far as uniqueness is concerned the scan showed that all the systems in the range of values between the experimental sets and the last one given in table 3.4 and which gave the correct compressibilities were very close to the latter. All five sets in table 3.4 satisfy the stability condition (3.19). It should also be known that since 10 constants had to be varied with small increments the scan was very time consuming on the computer.

We end this chapter by making it clear that by no means are we claiming that the given set is the set of elastic constants for anthracene but it is a set which predicts the compressibilities correctly and it is the only set which is close to Afanaseva's values.

References Chapter III

1. D.C. Northrop and D. Simpson, Proc. Roy. Soc., 2449, 377 (1958)
2. R.G. Kepler, Phys, Rev. 119, 1226 (1960)
3. D.C. Hoesterey and G.M. Letson, J. Phys. Chem. Solids, 24, 1609 (1963)
4. J.N. Sherwood, Purification and Growth of Large Anthracene Crystals in M. Zeif editors. Methods and Techniques of Fractional Solidification (M. Dekker, New York, 1969)
5. F. Gutmann and L.E. Lyons, Organic Semiconductors (J. Wiley and Sons, Inc., New York, 1967) P. 130
6. F.R. Lipsett, Can. J. Phys. 35, 284 (1957)
7. J.N. Sherwood and S.J. Thomson, J. Sa. Inst. 37, 242 (1960)
8. S. Singh et al, J. Chem. Phys. 42, 330 (1965)
9. R.C. Jarnagin et al, J. Chem. Phys. 39, 573 (1962)
10. I. Nakada, J. Phys. Soc. of Japan 17, 113 (1962)
11. J.M. Robertson , Revs. Mod. Phys. 30, 155 (1958)
12. B.O. Loapstra, Nucl. Inst. Methods 44, 181 (1966)
13. G. Shirane and V.J. Minkiewicz, Nucl. Inst. Mehtods 89, 109 (1970)
14. V.C. Sinclair, J. Monteath Robertson and A. McL. Mathieson Acta Cryst. 3, 251 (1950)

15. S.N. Vaidya and G.C. Kennedy, J. Chem. Phys. 55, 987 (1971)

16. Stuart A. Rice and Joshua Jortner, Physics of Solids at High Pressure (Academic Press 1965) P.134-139, United Kingdom Edition.

17. P.W. Bridgman, Proc.Am. Acad. Arts Sci 76,9,71 (1945); ibid. 76,1,19 (1945); ibid 76,3,83 (1948)

18. G.S. Kabalinka, Soviet Phys. Solid State 4, 2288 (1963)

19. G.K. Afanaseva, K.S. Aleksandrov, and A.J. Kitaigorodskii, Phys, Stata Sol. 24, K61 (1947)

20. H.B. Huntington, S.G. Gangoli, and J.L. Mills, J. Chem. Phys. 50, 9, 3844 (1969)

21. T. Danno and H. Inokuchi, Bulletin of the Chemical Society of Japan 41, P. 1783 (1968)

22. G.S. Pawley, Phys. Status Solidi, 20, 347 (1967)

23. A.I. Kitaigorodskii, J. Chem. Phys. 63, 1 (1966)

24. Leon Brillouin, Tensors in Mechanics and Elasticity (Acadamic Press. New York. London. 1964), p 310.

Chapter IV

Dependence of Band Structure, Drift and Hall Mobilities in Anthracene on Pressure

In this chapter the band structure of anthracene crystal and its dependence on pressure will first be calculated. The results of these calculations will then be used together with the linear compressibilities to calculate the drift and Hall mobilities of excess electron and excess holes, in the constant free path and constant relaxation time models, as well as their dependence on pressure.

The anthracene crystal is monoclinic with two molecules per unit cell. The unit cell structure is shown schematically in Fig. 4.1. The molecule with geometrical center at (0,0,0) is transformed into that with center at $(a/2, \frac{b}{2}, 0)$ by reflection in the ac plane followed by the indicated translation.

I. Band Structure

A. Summary of prior work.

The band structure of one excess electron and one excess hole in crystalline anthracene was first calculated by Le Blanc(1) in the tight binding approximation. This approximation was used because of the relatively small binding energy of the molecules in the anthracene crystal compared to excitation energies of the various excited electronic states of the molecule. Le Blanc based his calculations on a number of assumptions. In what follows we state the assumptions and discuss the validity of some of them.

1. The Hamiltonian matrix of the anthracene crystal is identical to one describing a hypothetical crystal which contains one molecule per unit cell.

This assumption is not justified since corresponding to the two molecules per unit cell there are two bands (arising from the symmetric and antisymmetric combina-

FIG. 4.1

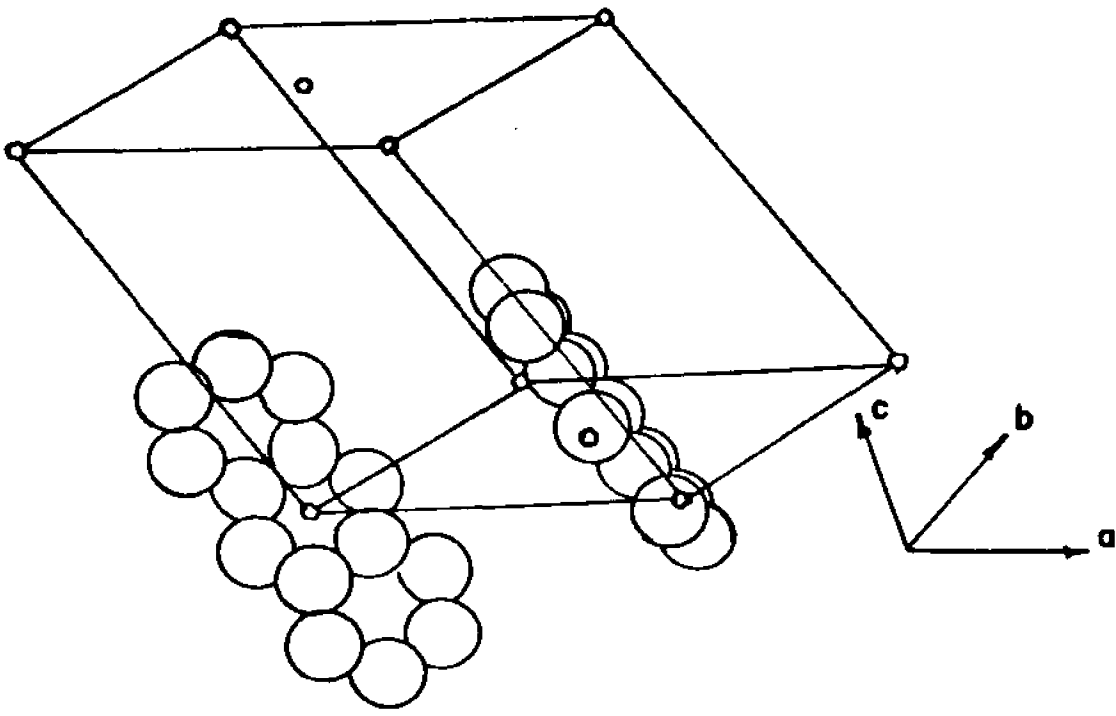

a. crystal structure of anthracene

b. cross section of the first Brillouin zone

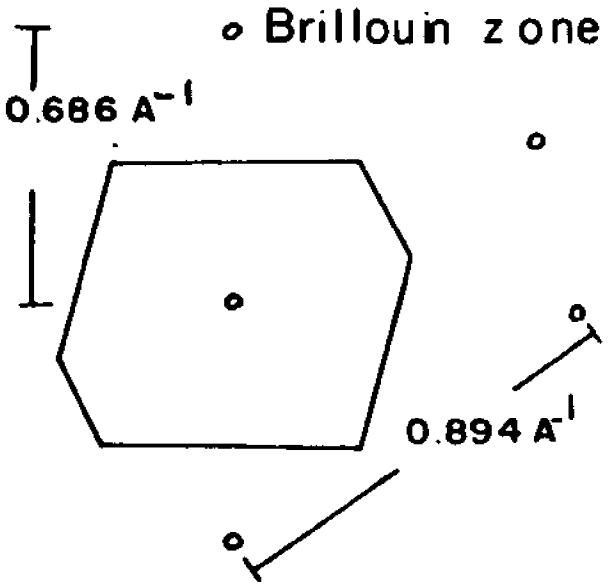

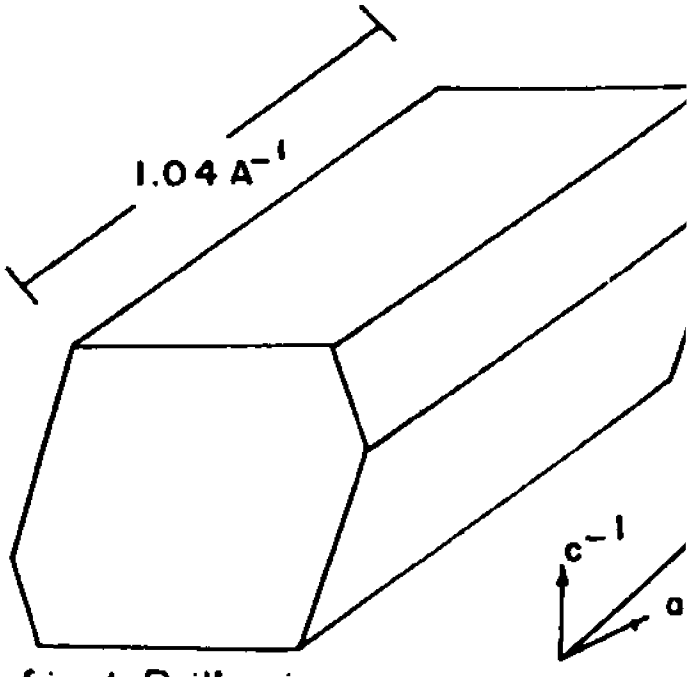

c. first Brillouin zone

tions of molecular wavefunctions in a unit cell) for the electron and two bands for the hole whereas in LeBlanc's calculation there is only one band for each.

2. The crystal is rigid and consists of non-vibrating molecules. This will be mentioned on page 66.

3. He used a one electron crystal wavefunction for the excess electron or hole represented by a Bloch sum of molecular orbitals as given by equation (4.1) below

$$\Psi_{\underline{k}}(\underline{r}) = \sum_{n=1}^{N} \exp(i\underline{k}\cdot\underline{r})\,\Phi_n(\underline{r}-\underline{r}_n) \qquad (4.1)$$

Where Φ_n is the molecular wavefunction of the molecule whose center is at $\underline{r}_n$, and N is the number of molecules in the crystal. Φ_n is understood to be oriented in the crystal in the same way as is molecule n. Otherwise, Φ_n is the same function for all n.

4. The molecular orbitals are linear combinations (Hückel) of single Slater carbon-atom 2P orbitals.

$$\Phi_n = \sum_i C_{ni} u_i \qquad (4.2)$$

The coefficients C_{ni} are determined from the secular equations given by Hückel[2] with overlap between the u_i neglected.

The parameter used in the atomic orbitals is that given by Slater[3],

$$u_i = \left(\frac{\alpha^5}{\pi}\right)^{1/2} r_i \cos(\xi_i) \exp(-\alpha r_i) \qquad (4.3)$$

with $\alpha = 1.64$ a.u. $= 3.08 \times 10^8\ cm^{-1}$

The calculation of the excess electron or excess hole band energies requires knowledge of the detailed behavior of the molecular wavefunctions at large distances. The use of a single Slater wavefunction seriously underestimates the magnitude of the tails of the wavefunction and therefore is inappropriate for such calculation[4].

5. Intermolecular overlap may be neglected.

6. The potential of a neutral molecule may be taken as the sum of the Goeppert-Mayer and Sklar[5] potentials of carbon atom.

$$V_n = \sum_i V_i \qquad (4.4)$$

Using Slater-type orbitals, V_i is given by

$$V_i = -e^2 r_i^{-1}\left[4 + 6(\alpha r_i) + 4(\alpha r_i)^2 + \frac{4}{3}(\alpha r_i)^3\right]\exp(-2\alpha r_i) \qquad (4.5)$$

7. Only two-center integrals need be considered. Although three-center integrals where the centers are on three different molecules are truly negligible because the interatomic distances are very large, the terms in which the potential and one wavefunction are on the same molecule, while the other wavefunction is on a different molecule are not negligibly small, as will be shown in this work.

The results of the calculations of LeBlanc show that both bands are highly anisotropic and each is found to be approximately 0.56KT wide at room temperature.

Thaxton[6] et al extended LeBlanc's calculation to other aromatic hydrocarbons. Katz[4] et al, although adopting the same general technique of LeBlanc, refined the calculations by avoiding some of the invalid assumptions as follows. They considered the actual crystal with two molecules per unit cell, and hence obtained the symmetrical and antisymmetrical bands. The wavefunction is therefore written as $\Psi_\pm = \sum_{l=0}^{2N-1} (\pm)^l \exp(i\underline{k}\cdot\underline{r}_l)\,\Phi(\underline{r}-\underline{r}_l)$

Where the index l labels the molecules which are now numbered so that the molecule at the corner of the cell has an even index while the one at the center of the cell has an odd index.

To account properly for the behavior of the molecular wavefunctions at the large intermolecular distances relevant to the problem considered, Katz et al used carbon atomic orbitals represented by the best available Hartree-Fock SCF carbon 2P ground state function involving a linear combination of four Slater-type functions. These atomic orbitals are given by equation (4.7) below

$$U_i(\underline{r}) = \hat{n}_i \cdot \underline{r} \sum_{j=1}^{4} a_j \left(\frac{\alpha_j}{\pi}\right)^{1/2} \exp(-\alpha_j r) \qquad (4.7)$$

Where $\hat{n}_i$ is the unit vector defining the direction of the 2P orbital. The coefficients a_j and orbital exponents α_j are those given by Clementi and Roothaan[7]. Katz et al calculated the bandwidths to be of the order of 0.1 e.v. in the $\underline{a}^{-1}$ and $\underline{b}^{-1}$ directions, the symmetric and antisymmetric bands are degenerate at the zone edge. The electron bands are appreciably split in the $\underline{c}^{-1}$ direction, but not the hole bands. Silbey et al[8] modified the calculation of Katz as follows,

(a) The effect of molecular vibrations is included by taking the molecular wavefunctions as the product of an electronic part and a vibrational part. This representtion corresponds to the weak-coupling limit of vibronic interaction, i.e., the nuclear part of the Hamiltonian is diagonalized before the crystal field part. Using this approximation, they took symmetrized wavefunctions of the entire crystal with an excess or deficency of one electron in the form

$$\Psi_{\pm}(\underline{K}) = \sum_{\ell=0}^{2N-1} (\pm)^{\ell} \exp(i\underline{K}\cdot\underline{r}_{\ell}) \, \mathcal{A} \, \phi_{\ell}^{k}(1)$$
$$\times \prod_{i=0}^{2N-1} (\phi_i^1(i,1) \cdots \overline{\phi}_i^{q}(i,2a)\chi_i), \qquad (4.8)$$

Where ϕ^k is the lowest unoccupied molecular orbital of a molecule for electrons and the highest occupied molecular

orbital for holes, the ϕ_i are the a occupied molecular orbitals of molecule i the bar over ϕ means that the electron in that molecular orbital has β spin, and χ_i is the ground state vibrational wavefunction of the molecule. It is assumed that all the vibrational wavefunctions are the same except for that of the molecule with an excess electron or hole. It should be noted here that the wavefunction (4.8) is the wavefunction of the entire crystal with an excess electron (or hole) and not that of the excess electron (or hole) alone. This formalism implies, of course, that every electron or hole band is split into many bands, each characterized by a vibrational wavefunction.

The $K=0$ levels of these bands will be separated by the vibrational quantum, which in aromatic molecules is of the order of 0.2 e.v. Their calculation gave bandwidths of the order of 0.01 e.v. a d thus the bands are well separated.

(b) The potential of the η^{th} neutral molecule was taken to be

$$V'_\eta(\underline{r}-\underline{r}_\eta) = V_\eta(\underline{r}-\underline{r}_\eta) - \frac{a}{i=1} K_\eta^i \qquad (4.9)$$

Where $V_\eta(\underline{r}-\underline{r}_\eta)$ is the Goeppert-Mayer and Sklar potential used by Katz, K_η^i is the exchange potential of the i^{th} molecular orbital on the η^{th} molecule.

In their original paper they calculated the mobility tensor, in both the constant free time and constant free path approximations, and the widths of excess electron and excess hole bands using different vibrational overlap. However, the program used to calculate the exchange effects on the energy was in error. In a later erratum[9] they corrected the program for the exchange energy. In calculating the mobility tensor and the bandwidths they only considered the case where the vibrational overlap squared has the value 1.0. With this correction they concluded that the calculated ratios of the components

of the mobility tensor are in fair agreement with experiment for the hole, but not for the electron.

Glaeser and Berry[10] calculated the band structure taking into account the exchange effects and the effects of polarization, by the excess electron (or hole), of the electrons on neighboring molecules. They took the tight-binding wavefunctions to be a linear combination of localized crystal functions ψ_ℓ as follows

$$\Psi_{\pm}(\underline{k}) = \sum_{\ell} (\pm)^{\ell} \exp(i\underline{k}\cdot\underline{r}_\ell)\,\psi_\ell, \qquad (4.10)$$

The summation alternating over equivalent and inequivalent molecules to give the even and odd symmetry-adapted functions[4].

The localized crystal wavefunction ψ_ℓ is taken to be an antisymmetrized product of molecular wavefunctions, in which one molecule is either a negative or a positive ion and the remainder are perturbed (polarized) by the ionic molecule. Symbolically the wavefunction corresponding to the electron or hole being on molecule "i" was taken as follows

$$\Psi_i = \mathcal{A}\,\psi_i(2a\pm1)\prod_{j\neq i}\psi_j^{(i)}(2a) \qquad (4.11)$$

"a" being the number of filled orbitals in the neutral molecule, $\psi_i(2a\pm1)$ denotes the wavefunction of the appropriate molecular ion, and $\psi_j^{(i)}$ The wavefunction of the molecule j in the field of this ion.

Each polarized orbital χ was written as the renormalized sum of the unperturbed orbital plus a sum, over the three principal directions of the molecule, of the first excited orbital which can be mixed in by the field of the ion.

$$\chi_j^{(i)} = \Big(\chi_j + \sum_x \delta_x^{(i)}\chi_j^{(x)}\Big)\Big/\Big(1+\sum_x|\delta_x^{(i)}|^2\Big)^{1/2} \qquad (4.12)$$

The perturbation coefficients $\delta_x^{(i)}$ were expressed in terms of the known anisotropic polarizability[11] and the oscillator strengths of the dipole-allowed transitions

of the molecules. The transfer integrals were expressed as three separate types of terms, each of which is reduced by the same factor representing the overlap of polarized wavefunctions (corresponding to two different locations of the electron or hole).

$$J_{ij} = [\mathcal{E}(\text{resonance}) + \Delta\mathcal{E}(\text{resonance}) + \mathcal{E}(\text{electrostatic})]\,S \qquad (4.13)$$

Where $\mathcal{E}$ (resonance) is the sum of terms involving the neutral molecule potential (for electrons) or positive ion-molecule potential (for holes) and terms coming from intermolecular electron exchange, as given by Silbey et al[8] $\Delta\mathcal{E}$ (resonance) gives the correction to these terms which results from the use of polarized orbitals. $\mathcal{E}$(electrostatic) represents the off-diagonal element of the long-range interaction between the excess charge and the induced dipoles on neighboring molecules. S is the product of overlaps of neutral molecules polarized by a charge at i with neutral molecules polarized by a charge at j. Drift mobility tensor was calculated both in the constant relaxation time and constant free path models.

The Glaeser and Berry calculations show that the anisotropy of the mobility as predicted by the band theory is in quite good agreement with the experimental anisotropy except in the c' direction for electrons. However, these calculations result in a free path which is significantly smaller than the molecule-to-molecule distance and a free time which is not significantly larger than the lifetime associated with the uncertainity principle. These two difficulties make the results of the band theory as calculated by Glaeser and Berry not consistent with the inital requirements of the model.

Chojnacki[12] made calculations similar to those of Thaxton et al but included all integrals between molecules containing carbon atoms closer than 10 A from each other in the two-center resonance integrals between molecule 1 and molecule ℓ. His results did not introduce any new features.

B. Current work.

In this work the general procedure followed by Katz et al was used to calculate the intermolecular resonance integrals and their change with pressure.

Method of calculation.

A one electron crystal wavefunction as given by equation (4.6) was used. The Hamiltonian appropriate to an excess electron (or hole) has the form

$$H = \left(\frac{-\hbar}{2m}\right)\nabla^2 + V(\underline{r}) \qquad (4.14)$$

Where $V(\underline{r})$, which determines the crystal field, was approximated by

$$V(\underline{r}) = \sum_n V_n(\underline{r}-\underline{r}_n) \qquad (4.15)$$

With V_n the Hartree potential of an isolated neutral molecule. For an isolated molecular ion the Hamiltonian is

$$H^0_\ell = \left(\frac{-\hbar^2}{2m}\right)\nabla^2 + V_\ell, \qquad (4.16)$$

from which follows that

$$e_0 = \int \phi^* H^0 \phi \, d\tau \qquad (4.17)$$

is the energy of the isolated negative ion relative to infinite separation of the electron and the neutral molecule. The energy is a double valued function of $\underline{K}$ and is calculated from $E_+ = \int \psi_+^* H \psi_+ d\tau / \int \psi_+^* \psi_+ d\tau$

$$E_- = \int \psi_-^* H \psi_- d\tau / \int \psi_-^* \psi_- d\tau \qquad (4.18)$$

After simplification by use of several systematic approximations, with the neglect of three-center intermolecular integrals and overlap integrals multiplied by e_n

or e_ℓ, the substitution of equations (4.14), (4.15), (4.16) and (4.17) into equation (4.18) leads to

$$E_\pm = e_o + \sum_n{}' e_n + \sum_\ell (\pm)^\ell \cos(\underline{K}\cdot\underline{r}_\ell)\, e_\ell \qquad (4.19)$$

Where the sums are taken over all molecules except the one with the center located at the origin. Note that those three-center integrals whose centers lie on three different molecules were neglected. The intermolecular resonance integrals e_ℓ were evalulated when only two-center integrals were considered and when the contribution of the three-center integrals, where one wavefunction and the potential are on the same molecule, were taken into account as well.

The symbols appearing in equation (4.19) are defined as follows

$$e_o = \int \Phi^* H^o \Phi \, d\tau \qquad (4.20)$$

$$e_n = \int \Phi^*(\underline{r}) V_n(\underline{r}-\underline{r}_m)\Phi(\underline{r})\, d\tau \qquad (4.21)$$

$$e_\ell = \int \Phi^*(\underline{r}-\underline{r}_\ell) V_\ell(\underline{r}-\underline{r}_\ell)\Phi(\underline{r})\, d\tau \qquad (4.22)$$

In order to discuss the $\underline{K}$ variation of the energy bands, it is necessary only to examine the last term in equation (4.19).

$$E'_\pm(\underline{K}) = E_\pm(\underline{K}) - e_o - \sum_n{}' e_n = \sum_\ell (\pm)^\ell \cos(\underline{K}\cdot\underline{r}_\ell)\, e_\ell \qquad (4.23)$$

All the integrals between the molecules on the corner and centers of the bases of the unit cell were calculated. This is equivalent to the calculation of the integrals between the molecule in the position numbered 1 in Fig. 4.2 and the molecules in positions 2 through 13. Because of its location, molecule 14 has also been included in the calculation. Neglecting the interactions with other molecules (The nearest neglected molecule has no atoms closer than 7.5 A.), the energy dependence on $\underline{K}$ is

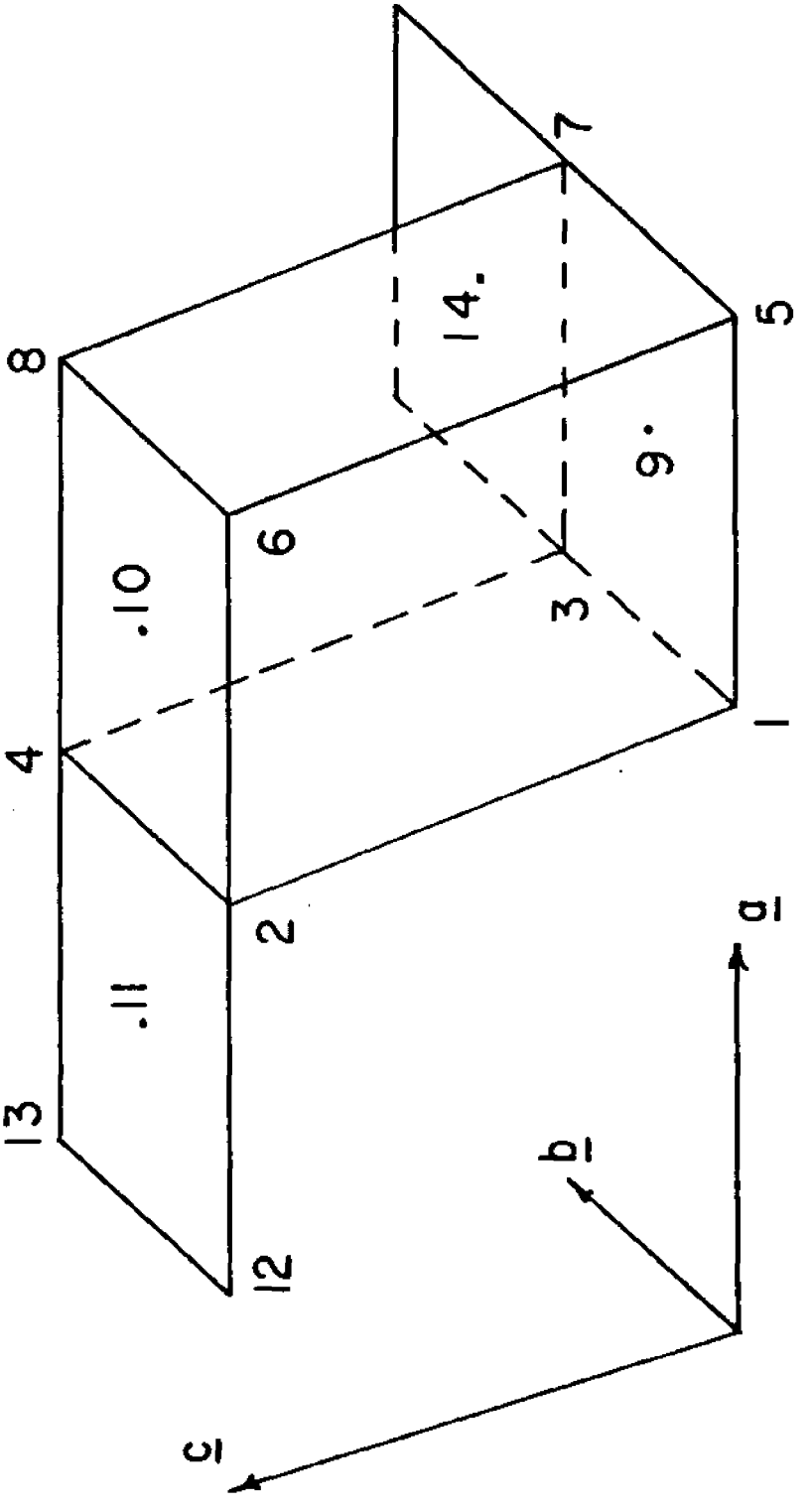

FIG. 4.2

$$E'_{\pm}(\underline{K}) = 2E_2\cos(\underline{K}\cdot\underline{c}) + 2E_3\cos(\underline{K}\cdot\underline{b}) + 2E_4[\cos(\underline{K}\cdot(\underline{b}+\underline{c})) + \cos(\underline{K}\cdot(\underline{b}-\underline{c}))] + 2E_5\cos(\underline{K}\cdot\underline{a}) + 2E_6\cos(\underline{K}\cdot(\underline{a}+\underline{c})) + 2E_7[\cos(\underline{K}\cdot(\underline{a}+\underline{b})) + \cos(\underline{K}\cdot(\underline{a}-\underline{b}))] + 2E_8[\cos(\underline{K}\cdot(\underline{a}+\underline{b}+\underline{c})) + \cos(\underline{K}\cdot(\underline{a}-\underline{b}+\underline{c}))] \pm 2E_9[\cos(\underline{K}\cdot\tfrac{1}{2}(\underline{a}+\underline{b})) + \cos(\underline{K}\cdot\tfrac{1}{2}(\underline{a}-\underline{b}))] \pm 2E_{10}[\cos(\underline{K}\cdot(\tfrac{1}{2}(\underline{a}+\underline{b})+\underline{c})) + \cos(\underline{K}\cdot(\tfrac{1}{2}(\underline{a}-\underline{b})+\underline{c}))] + 2E_{11}[\cos(\underline{K}\cdot(\tfrac{1}{2}(\underline{b}-\underline{a})+\underline{c})) + \cos(\underline{K}\cdot(\underline{c}-\tfrac{1}{2}(\underline{a}+\underline{b})))] + 2E_{12}\cos(\underline{K}\cdot(\underline{c}-\underline{a})) + 2E_{13}[\cos(\underline{K}\cdot(\underline{b}-\underline{a}+\underline{c})) + \cos(\underline{K}\cdot(\underline{c}-\underline{a}-\underline{b}))] + 2E_{14}[\cos(\underline{K}\cdot\tfrac{1}{2}(\underline{a}+3\underline{b})) + \cos(\underline{K}\cdot\tfrac{1}{2}(\underline{a}-3\underline{b}))]$$

(4.23)

Where the 13 E_i are resonance integrals between molecules 1 and i such as given by e_ℓ in equation (4.22)

Numerical calculation

The first step in making numerical calculations from equation (4.22) is the selection of a suitable molecular wavefunction for the molecular ion. The simplest approximation to the molecular wavefunction would place the extra electron in the first unoccupied molecular orbital of the neutral molecule and describe the electronic motion as if the interaction between electron and molecule caused no change in the orbital in question. Thus, Balk et al[13] have shown that the properties of isolated negative aromatic ions can be understood if the orbital occupied by the excess electron is described by the Hückel coefficients characteristic of the first unoccupied orbital of the neutral molecule.

It is interesting to note that Hückel functions are not unreasonable approximations to self-consistent field functions with differential overlap neglected.
The Balk approximation rests on two considerations:

(a) Pople[142] proved that the Coulson and Rushbrooke theorem[14b] remains valid in the more general SCF scheme, i.e., the π electrons are uniformly distributed in the ground state and in singly excited states.

(b) Given the uniform charge distribution cited, it may be guessed that the addition of one electron will not grossly change the charge distribution of the original electrons. Certainly this approximation can only be considered if the π electron system is large.

In the mononegative ion, excitations are then described in terms of promotion of the extra electron, the remaining system being considered to be the original molecule in the ground state or in an excited state. It should be noted that even if the suppositions made are exactly true, the neglect of exchange between the extra electron and the core electrons prevents the orbital described from becoming the one electron self-consistent field orbital.

It is clear that the Balk approximation will be best if the neutral core remains the same and only excitations of the extra electron are considered. Indeed, these are just the terms considered in the present calculation of $E(\underline{K})$. Before proceeding, however, it is necessary to remark that the Pariser-Parr or Pople theories of hydrocarbon spectra fail in the calculation of ionization energies although they are very successful in describing the atomic spectra. Hoyland and Goodman [151] have traced the difficulties to three factors.

(a) The effect of π-electron-ionization or capture on the framework of the molecule;
(b) The changes in π-basis functions upon electron ionization or capture;
(c) Changes in the π electron molecular orbitals through construction of a new Hartree-Fock Hamiltonian for the resulting ion and subsequent reminimization of the energy.

By combining the Pariser-Parr formulation of π electron theory[16] with Roothaan's self-consistent field theory and assumptions of orbital deformation, excellent agreement between computed and measured ionization potentials was obtained by Hoyland and Goodman.

Because of the importance of the choice of the molecular wavefunctions, we have made the calculations in this work using the wavefunctions computed by Hoyland and Goodman.

Now that all the assumptions have been mentioned, it remains to consider the approximations involved in obtaining numerical results from equation (4.22). The molecular oribtals of a positive or negative ion are approximated by a linear combination of neutral carbon $2p_z$ wavefunctions u_i

$$\Phi_\eta = \sum_i C_{ni} u_i \qquad (4.25)$$

Where the C_{ni} are the coefficients given by Hoyland and Goodman [15].

As already mentioned, the use of single Slater orbitals characterized by a single orbital exponent is inappropriate. The Slater-type function has only one adjustable parameter and this is chosen to minimize the energy of the atom. Since the tail (large R) of the wavefunction makes only a small contribution to the energy of the atom, it is very poorly represented by the usual Slater function. The integrals of greatest interest in the present calculation involve atoms centered on different molecules, and it is the large R portion of the wavefunction which is of interest here.

Katz et al tried to obtain a reasonable approximation to the tail of the wavefunction by trying to fit a single Slater-type function to the atomic SCF functions, adjusting the orbital exponent to give the best representation at large distance. However, using the best available neutral

carbon atom SCF 2P function they found that a good fit can not be obtained in the region 1-4 A using a wavefunction characterized by a single orbital exponent. Since the resonance integrals are very sensitive to the detailed form of the wavefunction, they used the best available carbon atom wavefunction represented in the form of a linear combination of four Slater wavefunctions. The same wavefunction was used in the present work, as given by equation (4.26)

$$U_i(\underline{r}) = (\underline{n}_i \cdot \underline{r}) \sum_{j=1}^{4} a_j \left(\frac{\alpha_j}{\pi}\right)^{1/2} \exp(-\alpha_j r) \qquad (4.26)$$

Where $\underline{n}_i$ is the unit vector defining the direction of the 2P orbital. The coefficients a_j and orbital exponents α_j are those given by Clementi and Roothaan.

The potential energy of the molecule is a linear combination of neutral-carbon-atom potentials. These are derived from classical electrostatic arguments using the Hartree method by averaging over the four (2S, $2P_x$, $2P_y$ and $2P_z$) electrons. The potential energy of a neutral molecule is therefore written as

$$V_n = \sum_i V_i \qquad (4.27)$$

Where V_i is the Goeppert-Mayer a d Sklar[5] potential of carbon atom i. Using equation (4.26) for U_i, V_i is given by equation (4.28)

$$V_i = -\frac{e^2}{r_i}\left(\sum_{k,\ell=1}^{4} \frac{a_\ell \alpha_\ell^{5/2} a_k \alpha_k^{5/2}}{\beta_{k\ell}^5}\right)^{-1} \sum_{k,\ell} \exp(-2\beta_{k\ell} r_i) \times \frac{a_k \alpha_k^{5/2} a_\ell \alpha_\ell^{5/2}}{\beta_{k\ell}^5}\left[\frac{4}{3}(\beta_{k\ell} r_i)^3 + 4(\beta_{k\ell} r_i)^2 + 6(\beta_{k\ell} r_i) + 4\right] \qquad (4.28)$$

Where $\beta_{k\ell} = \frac{1}{2}(\alpha_k + \alpha_\ell)$, substituting equations (4.26), (4.27), and (4.28) into equation (4.22), it becomes

$$e_\ell = \int \Phi^*(\underline{r}) V(\underline{r}) \Phi(\underline{r} - \underline{r}_\ell)\, d\tau$$
$$= \sum_{i,j,m=1}^{14} C_{\alpha i} C_{\beta j} \int U_i(\underline{r} - \underline{r}_i) V_m(\underline{r} - \underline{r}_m) U_j(\underline{r} - \underline{r}_\ell - \underline{r}_j)\, d\tau \qquad (4.29)$$

Le Blanc and Thaxton neglected those terms for which i does not equal m. They only considered two-center integrals and neglected all three-center integrals. As will be seen from the results of this work the three-center integrals where one wavefunction and the potential are on the same molecule can have significant contribution.

All of the calculations by other investigators discussed above were based on the calculation of Katz et al. Their investigation used both two-center and three-center integrals in a calculation based on the Hückel approximation. For comparison, they used two-center integrals only in calculations based on Hückel, Hoyland and Goodman models. Three-center integrals have not been used in the Hoyland and Goodman model.

In this work the Hoyland and Goodman approximation was used and calculations were done with two and three-center integrals and, for comparison, with two-center integrals only.

The two-center integrals were simplified by expanding in the form

$$\pi^{-1}\frac{(\underline{n}_i\cdot\underline{R}_{ij})(\underline{n}_j\cdot\underline{R}_{ij})}{R_{ij}^2}S_{ij}+$$

$$(2\pi)^{-1}\left[(\underline{n}_i\cdot\underline{n}_j)-\frac{(\underline{n}_i\cdot\underline{R}_{ij})(\underline{n}_j\cdot\underline{R}_{ij})}{(R_{ij})^2}\right]C_{ij} \qquad (4.30)$$

Where $\underline{n}_i$ and $\underline{n}_j$ are the unit vectors defining the direction of orbitals u_i and u_j, $\underline{R}_{ij}$ is the vector from atom i to atom j and

$$S_{ij}=\int r_i r_j \cos(\gamma_i)\cos(\gamma_j)v_i\left[\sum_\rho a_\rho \alpha_\rho^{5/2}\exp(-\alpha_\rho r_i)\right]\times \qquad (4.31)$$
$$\left[\sum_m a_m \alpha_m^{5/2}\exp(-\alpha_m r_j)\right]d\tau$$

$$C_{ij}=\int d\tau\, r_i r_j \sin\gamma_i \sin\gamma_j\, v_i\left[\sum_\rho a_\rho \alpha_\rho^{5/2}\exp(-\alpha_\rho r_i)\right]\times \qquad (4.32)$$
$$\left[\sum_m a_m \alpha_m^{5/2}\exp(-\alpha_m r_j)\right]$$

Where γ_i and γ_j are the angles $\underline{r}_i$ and $\underline{r}_j$ make with $\underline{R}_{ij}$.

These integrals were performed analytically and expressed as

Table 4.1

Hoyland and Goodman Coefficients C_{ni}

Atom No.i	C_{ni}	
	electrons	holes
1	0.29063	0.28891
2	-0.19657	0.19498
3	-0.19657	-0.19498
4	0.29063	-0.28891
5	0.29063	-0.28891
6	-0.19657	-0.19498
7	-0.19657	0.19498
8	0.29063	0.28891
9	-0.47703	-0.48180
10	-0.47703	0.48180
11	0.11451	-0.11155
12	0.11451	0.11155
13	0.11451	0.11155
14	0.11451	-0.11155

Table 4.2

Atomic orbital coefficients a_i and orbital exponents α_i for carbon atom as given by Clementi and Roothaan.

α_i in atomic units		a_i	
electrons	holes	electrons	holes
0.9372	1.1060	0.31916	0.68350
1.4147	0.5074	0.50063	0.05445
2.5545	2.3590	0.25045	0.35041
6.3021	6.2000	0.01097	0.01237

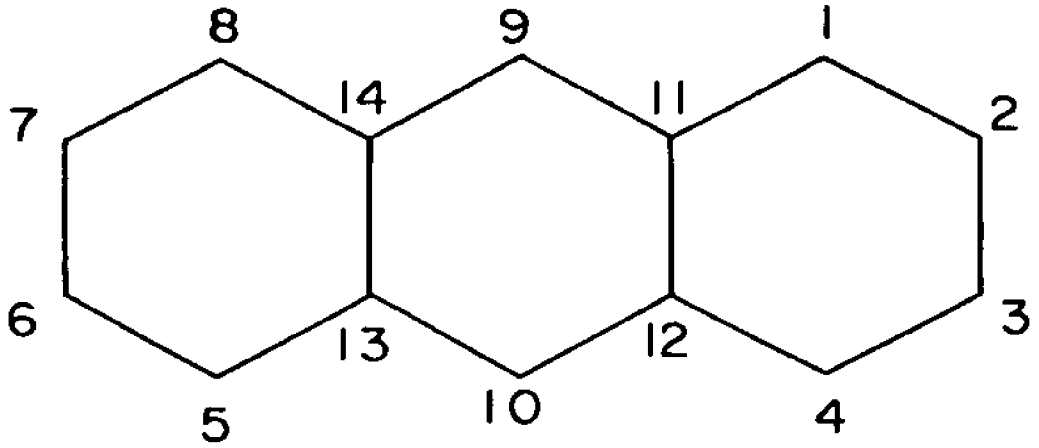

FIG. 4.3

anthracene molecule

a power series in the distance R_{ij} between the two atoms i and j. All integrals involving coordinates of atoms closer than 10 A were included. These power series were then evaluated at different pressures using a Xerox $\Sigma 7$ computer, it took about one hour at every pressure to evaluate the 13 required e_ℓ.

No such simplifications were possible in case of the three-center integrals and they had to be evaluated by a three-dimensional Gaussian integration, using 8000 points. Only those integrals in which the potential and wavefunction on the same molecule were on near-neighbor atoms were performed, and of them, only those where the distance between the two wavefunctions was less than 6.5 A. It took 25 computer hours to calculate the contribution of three-center integrals to the 13 e_ℓ at one pressure.

For reference purposes we tabulate the values of the Hoyland and Goodman coefficients used as well as the coefficients a_i and the orbital exponents α_i as given by Clementi and Roothaan. These constants are given in tables 4.1 and 4.2. The coefficients are labeled according to figure 4.3.

Atomic coordinates within a molecule were those measured by Sinclair, Robertson and Mathieson[17] using x-ray diffraction.

Numerical results

Tables 4.3 through 4.7 give the intermolecular resonance integrals at different pressures in units of 10^{-4} e.v.

Table 4.3

Intermolecular resonance integrals at different pressures in units of 10^{-4} e.v.

pressure P kilobars	electrons		holes	
		e_2		
	2 and 3-center integrals	2 center integrals	2 and 3-center integrals	2 center integrals
0.0	0.2744	0.1851	-0.4953	-0.2509
1.0		0.3705		-0.2128
2.0	0.7287	0.5775	-0.4394	-0.1678
3.0		0.8079		-0.1152
4.0	1.2750	1.064	-0.3151	-0.0538
5.0		1.3470		0.0175
6.0	1.9570	1.6600	-0.1527	0.0991
		e_3		
0.0	74.25	70.13	-125.9	-114.2
1.0		72.78		-118.3
2.0	79.95	75.53	-135.1	-122.5
3.0		78.39		-126.8
4.0	86.11	81.35	-145.1	-131.4
5.0		84.42		-136.0
6.0	92.74	87.61	-155.7	-140.9

Table 4.4

Intermolecular resonance integrals at different pressures in units of 10^{-4} e.v.

pressure P kilobars	e_4 electrons 2 and 3-center integrals	e_4 electrons 2 center integrals	e_4 holes 2 and 3-center integrals	e_4 holes 2 center integrals
0.0	-0.0251	-0.0251	-0.1291	-0.1291
1.0		-0.0270		-0.1375
2.0	-0.0280	-0.0280	-0.1478	-0.1478
3.0		-0.0286		-0.1597
4.0	-0.0314	-0.0314	-0.1710	-0.1710
5.0		-0.0334		-0.1814
6.0	-0.0353	-0.0353	-0.1921	-0.1921
		e_5		
0.0	0.2146	0.2146	0.2733	0.2733
1.0		0.2170		0.2828
2.0	0.2191	0.2191	0.3079	0.3079
3.0		0.2186		0.3348
4.0	0.2173	0.2173	0.3681	0.3681
5.0		0.2159		0.4040
6.0	0.2298	0.2298	0.4305	0.4305

Table 4.5

Intermolecular resonance integrals at different pressures in units of 10^{-4} e.v.

pressure P kilobars	electrons		holes	
	2 and 3-center integrals	2-center integrals	2 and 3-center integrals	2-center integrals
		e_6		
0.0	-0.4893	-0.5032	-3.230	-2.622
1.0		-0.5664		-2.853
2.0	-0.6279	-0.6339	-3.838	-3.113
3.0		-0.7114		-3.395
4.0	-0.8041	-0.7984	-4.573	-3.708
5.0		-0.8999		-4.054
6.0	-1.195	-1.009	-4.651	-4.423
		e_7		
0.0	0.0273	0.0273	0.0729	0.0729
1.0		0.0265		0.0785
2.0	0.0224	0.0224	0.0814	0.0814
3.0		0.0161		0.0824
4.0	0.0133	0.0133	0.0911	0.0911
5.0		0.0089		0.0992
6.0	0.0090	0.0090	0.1118	0.1118

Table 4.6

Intermolecular resonance integrals at different pressures in units of 10^{-4} e.v.

pressure P kilobars	electrons		holes	
	2 and 3-center integrals	2-center integrals	2 and 3-center integrals	2-center integrals
		e_8		
0.0	0.0193	0.0193	-0.0183	-0.0183
1.0		0.0185		-0.0169
2.0	0.0173	0.0173	-0.0159	-0.0159
3.0		0.0180		-0.0173
4.0	0.0194	0.0194	-0.0192	-0.0192
5.0		0.0205		-0.0222
6.0	0.0209	0.0209	-0.0271	-0.0271
		e_9		
0.0	-124.5	-115.5	-103.3	-85.59
1.0		-119.5		-87.52
2.0	-133.2	-123.6	-107.9	-89.44
3.0		-127.8		-91.36
4.0	-142.4	-132.1	-112.3	-93.28
5.0		-136.5		-95.19
6.0	-152.1	-141.1	-116.8	-97.07

Table 4.7

Intermolecular resonance integrals at different pressures in units of 10^{-4} e.v.

pressure P kilobars	e_{10} electrons 2 and 3-center integrals	e_{10} electrons 2-center integrals	e_{10} holes 2 and 3-center integrals	e_{10} holes 2-center integrals
0.0	1.5911	1.183	28.96	23.95
1.0		1.3370		25.66
2.0	2.041	1.507	33.17	27.48
3.0		1.695		29.42
4.0	2.565	1.902	37.87	31.49
5.0		2.131		33.69
6.0	3.138	2.382	43.13	36.03
		e_{11}		
0.0	0.0119	0.0119	0.0054	0.0054
1.0		0.0132		0.0063
2.0	0.0143	0.0143	0.0077	0.0077
3.0		0.0160		0.0100
4.0	0.0187	0.0187	0.0121	0.0121
5.0		0.0196		0.0130
6.0	0.0198	0.0198	0.0133	0.0133

e_{12} and e_{13} were zero for both holes and electrons. Also e_{14} for electrons was less than $.0027 \times 10^{-4}$ e.v. and e_{14} for holes was less than $.015 \times 10^{-4}$ e.v.

Therefore it was possible for the present purposes to neglect $e_8, e_{11}, e_{12}, e_{13}$, and e_{14}.

In order to see how the band structure changes with pressure we consider the special cases when $\underline{K}$ is parallel to a reciprocal lattice vector, $\underline{a}^{-1}$, $\underline{b}^{-1}$, or $\underline{c}^{-1}$.

$$E'_{\pm}(\underline{K} \| \underline{a}^{-1}) = A + B\cos(\underline{K}\cdot\underline{a}) \pm C\cos(\underline{K}\cdot\underline{a}/2) \qquad (4.33)$$

$$E'_{\pm}(\underline{K} \| \underline{b}^{-1}) = D + E\cos(\underline{K}\cdot\underline{b}) \pm F\cos(\underline{K}\cdot\underline{b}/2) \pm E_{14}\cos(\underline{K}\cdot 3\underline{b}/2) \qquad (4.34)$$

$$E'_{+}(\underline{K} \| \underline{c}^{-1}) = G_1 + H\cos(\underline{K}\cdot\underline{c})$$

$$E'_{-}(\underline{K} \| \underline{c}^{-1}) = I + J\cos(\underline{K}\cdot\underline{c}) \qquad (4.35)$$

Where the constants A through J are given by equations (4.36).

$$A = 2(E_2 + E_3 + 2E_4),$$
$$B = 2(E_5 + E_6 + 2E_7 + 2E_8 + E_{12} + 2E_{13}),$$
$$C = 4(E_9 + E_{10} + E_{11} + E_{14}),$$
$$D = 2(E_2 + E_5 + E_6 + E_{12}),$$
$$E = 2(E_3 + 2E_4 + 2E_7 + 2E_8 + 2E_{13}),$$
$$F = 4(E_9 + E_{10} + E_{11}),$$
$$G_1 = 2(E_3 + E_5 + 2E_7 + 2E_9 + 2E_{14}),$$
$$H = 2(E_2 + 2E_4 + E_6 + 2E_8 + E_{12} + 2E_{13} + 2(E_{10} + E_{11}))$$
$$I = 2(E_3 + E_5 + 2E_7 - 2E_9 - 2E_{14}),$$
$$J = 2(E_2 + 2E_4 + E_6 + 2E_8 + E_{12} + 2E_{13} - 2(E_{10} + E_{11})) \qquad (4.36)$$

It should be noted here that although $E(\underline{K})$ as given by equations (4.33) and (4.34) might seem to have a periodicity of $2\underline{a}^{-1}$ and $2\underline{b}^{-1}$, however, this is not so as we now show

$$\psi_+(\underline{K}+\underline{a}^{-1}) = \psi_-(\underline{K}),$$
$$\psi_-(\underline{K}+\underline{a}^{-1}) = \psi_+(\underline{K}), \qquad (4.37)$$

$$\psi_+(\underline{K}+\underline{b}^{-1}) = \psi_-(\underline{K})$$
$$\psi_-(\underline{K}+\underline{b}^{-1}) = \psi_+(\underline{K}) \qquad (4.38)$$

and when $\underline{K} = \frac{1}{2}\underline{a}^{-1}$ or $\underline{K} = \frac{1}{2}\underline{b}^{-1}$ equation (4.6) gives

$$\psi_+(\underline{K}) = \psi_-^*(\underline{K}) \qquad (4.39)$$

which proves ψ_+ and ψ_- have the same energy at $\frac{1}{2}\underline{a}^{-1}$ and $\frac{1}{2}\underline{b}^{-1}$. Thus in going from the first to the second Brillouin zone ψ_+ and ψ_- cross and interchange roles in the $\underline{a}^{-1}$ and $\underline{b}^{-1}$ directions, and there is therefore the expected periodicity of $\underline{a}^{-1}$ and $\underline{b}^{-1}$.

Figures (4.4) through (4.5) give the shape of the band, when $\underline{K}$ is parallel to $\underline{a}^{-1}$, $\underline{b}^{-1}$, $\underline{c}^{-1}$, for both holes and electrons when only two-center integrals are considered in calculating the intermolecular resonance integrals. Figures (4.6) and (4.7) give the shape of the band when both two and three-center integrals are considered.

As can be seen from these figures the $\underline{a}^{-1}$ and $\underline{b}^{-1}$ bands meet at $\frac{1}{2}\underline{a}^{-1}$ and $\frac{1}{2}\underline{b}^{-1}$ as shown before. At $\underline{K} = \frac{1}{2}\underline{a}^{-1}$ and $\underline{K} = \frac{1}{2}\underline{b}^{-1}$, the two bands are expected to be degenerate because of the existance of a twofold screw axis in the $\underline{b}$ direction and a glide plane in the $\underline{a}$ direction, the group of $\underline{K}$ has only a two-dimensional irreducible representation[18] at $\frac{1}{2}\underline{a}^{-1}$ and $\frac{1}{2}\underline{b}^{-1}$.

Figure captions

Figures 4.4 through 4.7 give the shape of the energy bands for an excess hole and an excess electron. figure 4.4 gives the hole bands energy in units of e.v."A" denotes the antisymmetric band while "S" denotes the symmetric one. in this figure only two-center integrals are included. figure 4.6 gives the same bands when both two and three-center integrals are included. figures 4.5 and 4.7 give the corresponding bands for an excess electron.figure 4.5 gives the case of two-center integrals only while figure 4.7gives the case of two and three-center integrals.

Figures 4.8 through 4.11 give the change of the bandwidths with pressure.the bandwidths are given in e.v.
the curves are labeled according to the following scheme,
"1" is the case when $\underline{k}$ is parallel to $\underline{a}^{-1}$.
"2" is the case when $\underline{k}$ is parallel to $\underline{b}^{-1}$
"3" is the case when $\underline{K}$ is parallel to $\underline{c}^{-1}$
Figures 4.8 and 4.10are for the hole bands when only two-center integrals and when two and three-center integrals are included respectively.
figures 4.9 and 4.11 give the respective cases for electrons.

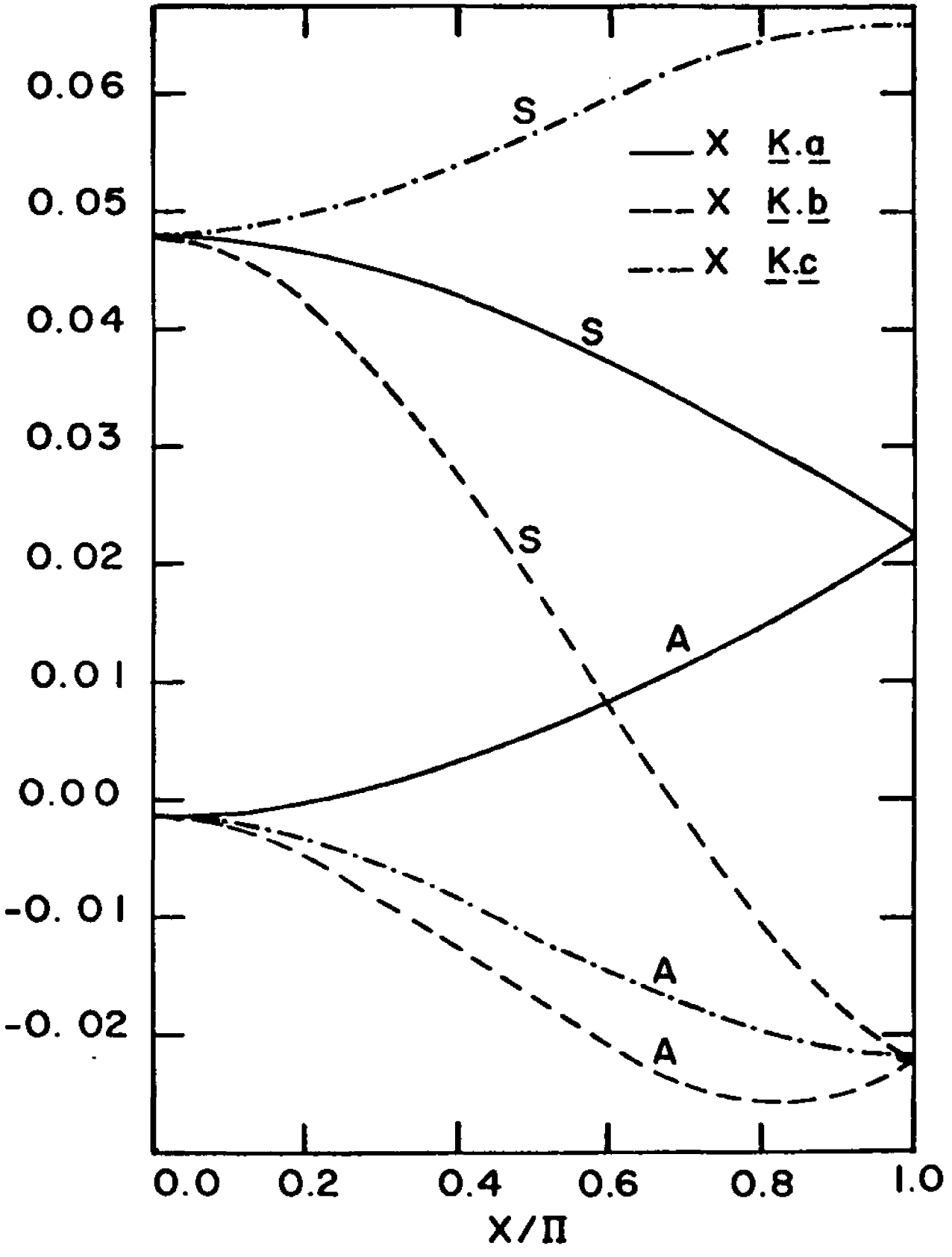
0.06
0.05
0.04
0.03
0.02
0.01
0.00
-0.01
-0.02
S
S
S
A
A
A
X K.a
X K.b
X K.c
0.0
0.2
0.4
0.6
0.8
1.0
X/Π

FIG. 4.4

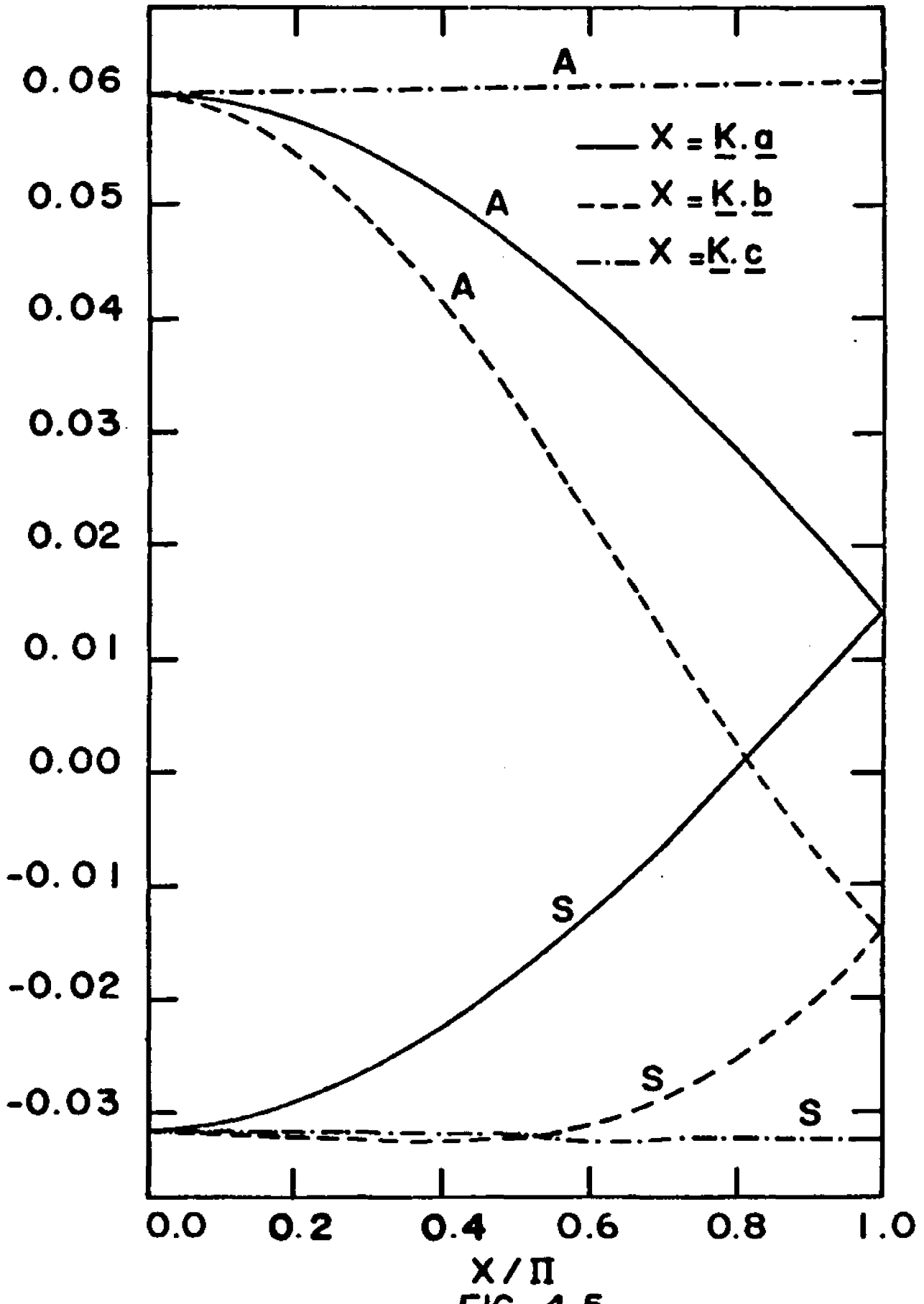
0.06
0.05
0.04
0.03
0.02
0.01
0.00
-0.01
-0.02
-0.03
A
A
A
S
S
S
X = K.a
X = K.b
X = K.c
0.0
0.2
0.4
0.6
0.8
1.0
X / Π

FIG. 4.5

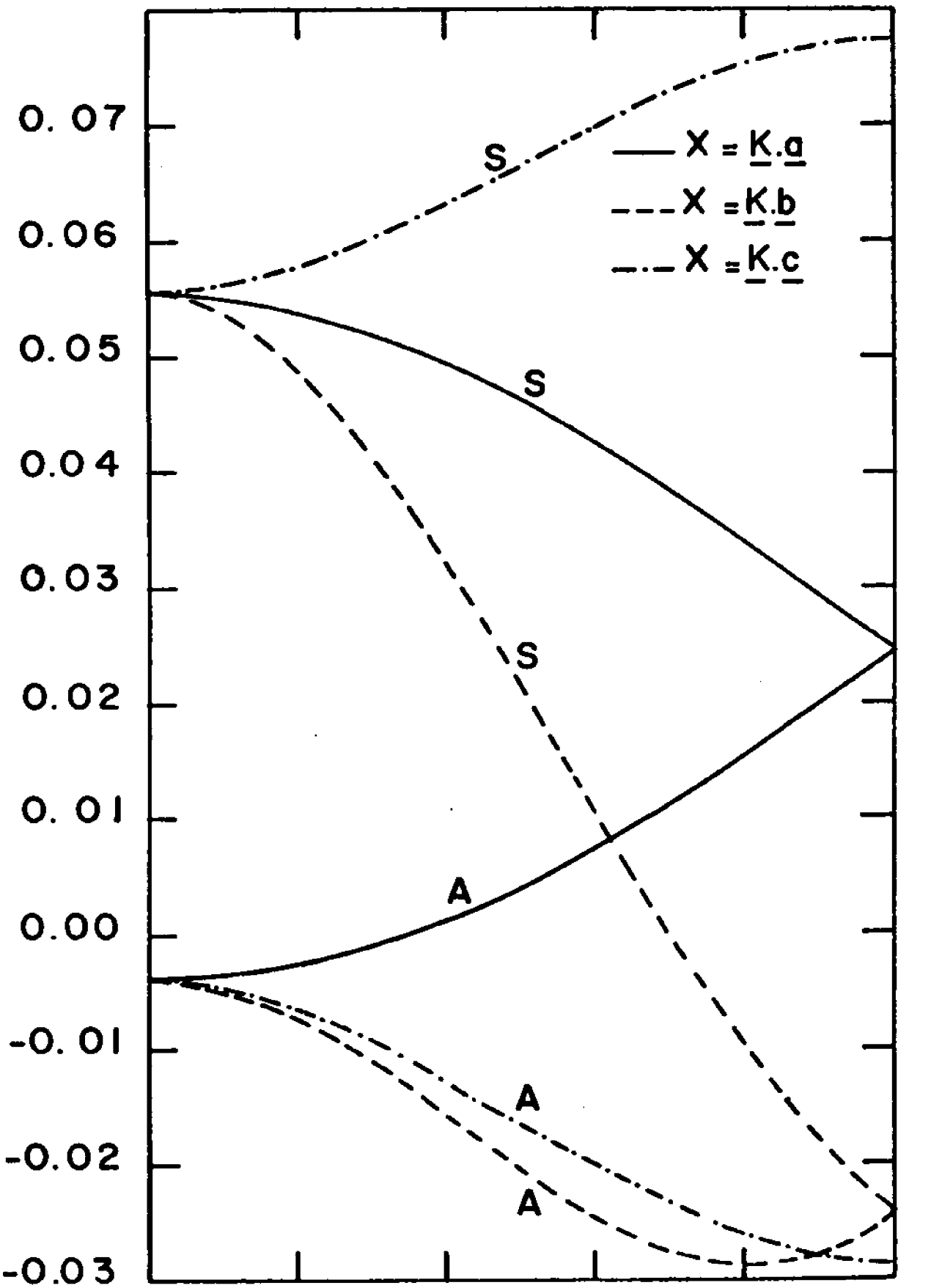
0.07
0.06
0.05
0.04
0.03
0.02
0.01
0.00
-0.01
-0.02
-0.03
0.0
0.2
0.4
0.6
0.8
1.0
X / Π
X = K.a
X = K.b
X = K.c
S
S
S
A
A
A

FIG. 4.6

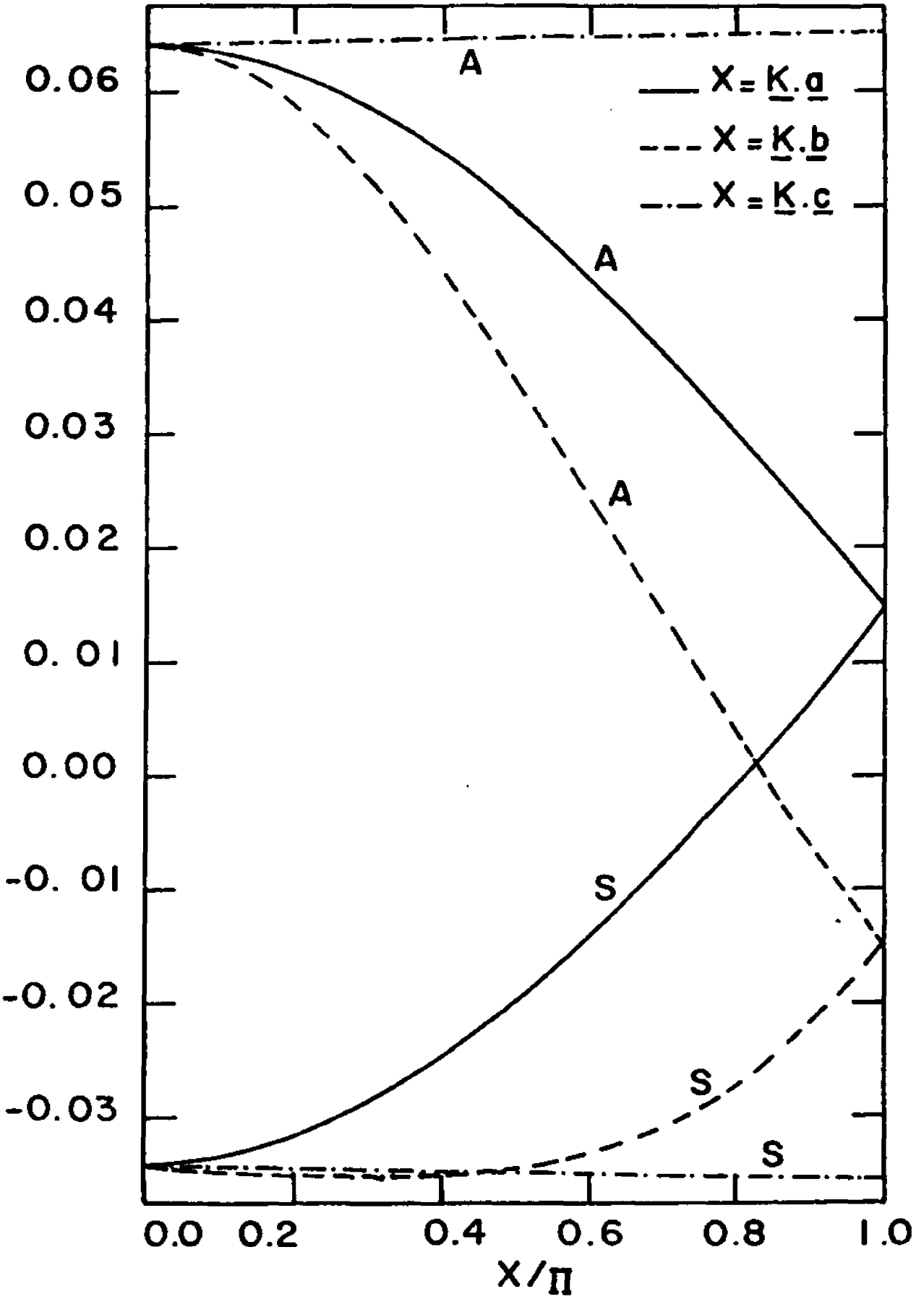
0.06
0.05
0.04
0.03
0.02
0.01
0.00
-0.01
-0.02
-0.03
0.0
0.2
0.4
0.6
0.8
1.0
X/Π
X = K.a
X = K.b
X = K.c
A
A
A
S
S
S

FIG. 4.7

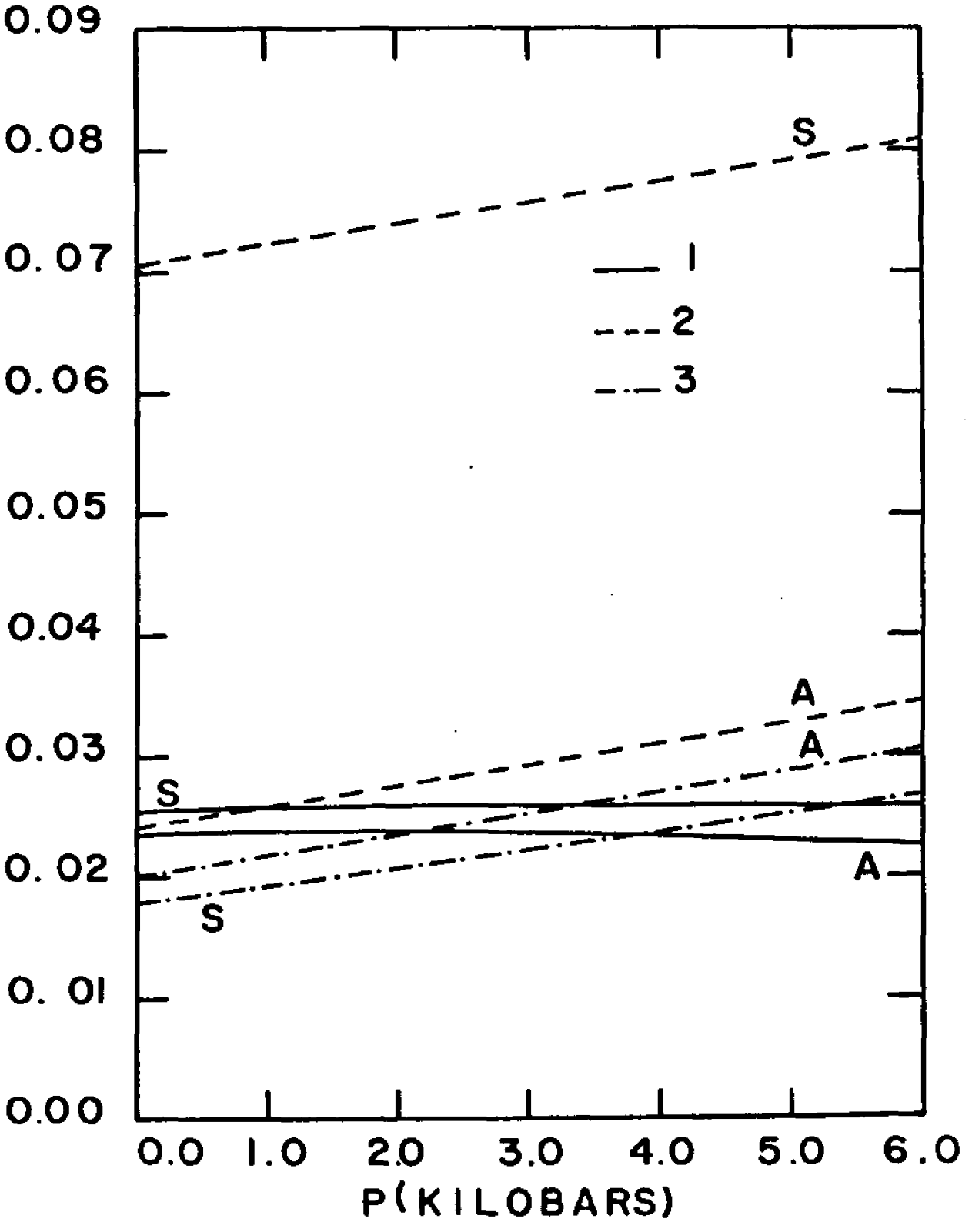
0.09
0.08
0.07
0.06
0.05
0.04
0.03
0.02
0.01
0.00
S
1
2
3
A
A
S
A
S
0.0
1.0
2.0
3.0
4.0
5.0
6.0
P(KILOBARS)

FIG. 4.8

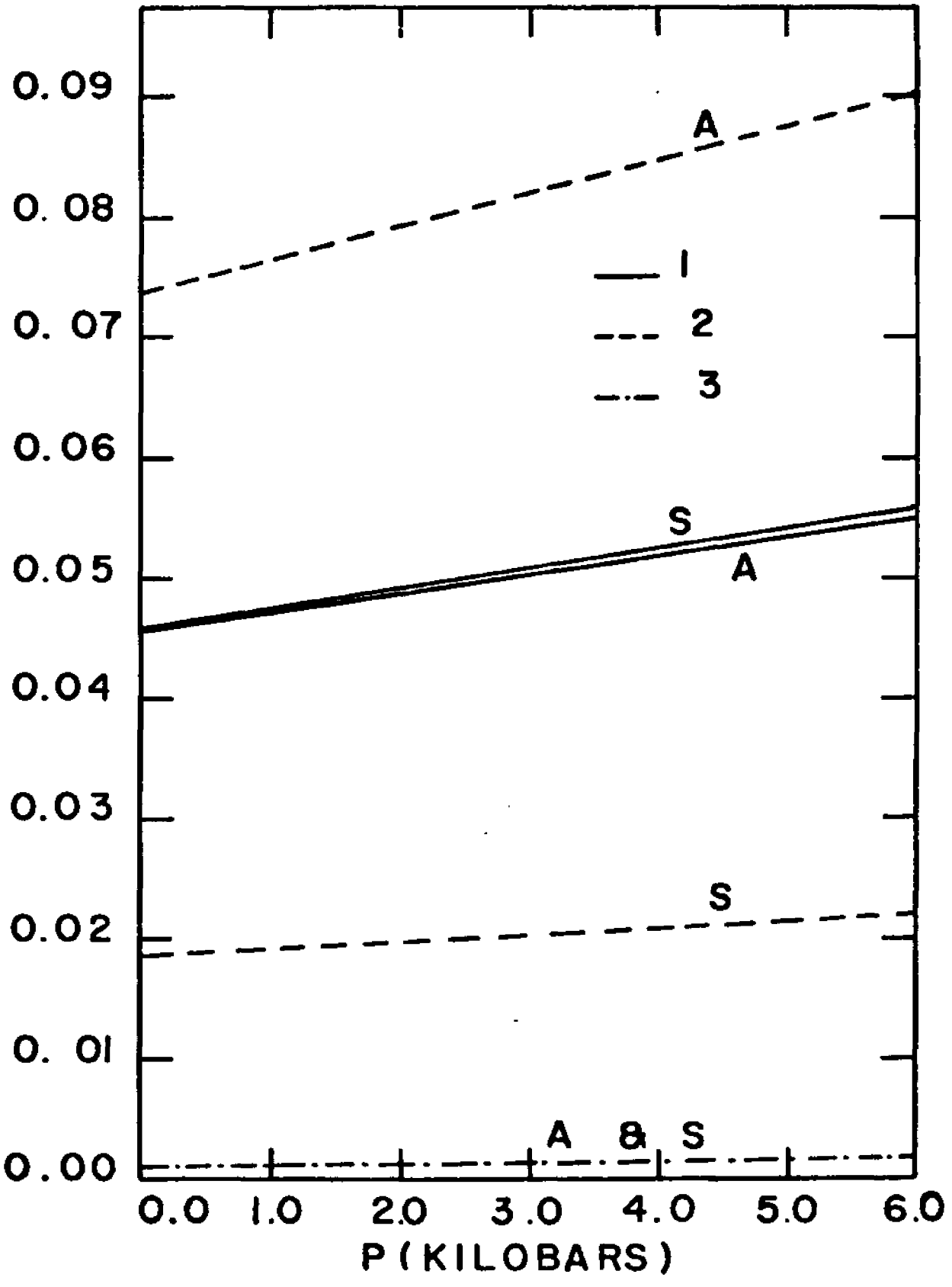
0.09
0.08
0.07
0.06
0.05
0.04
0.03
0.02
0.01
0.00
A
1
2
3
S
A
S
A & S
0.0
1.0
2.0
3.0
4.0
5.0
6.0
P (KILOBARS)

FIG. 4.9

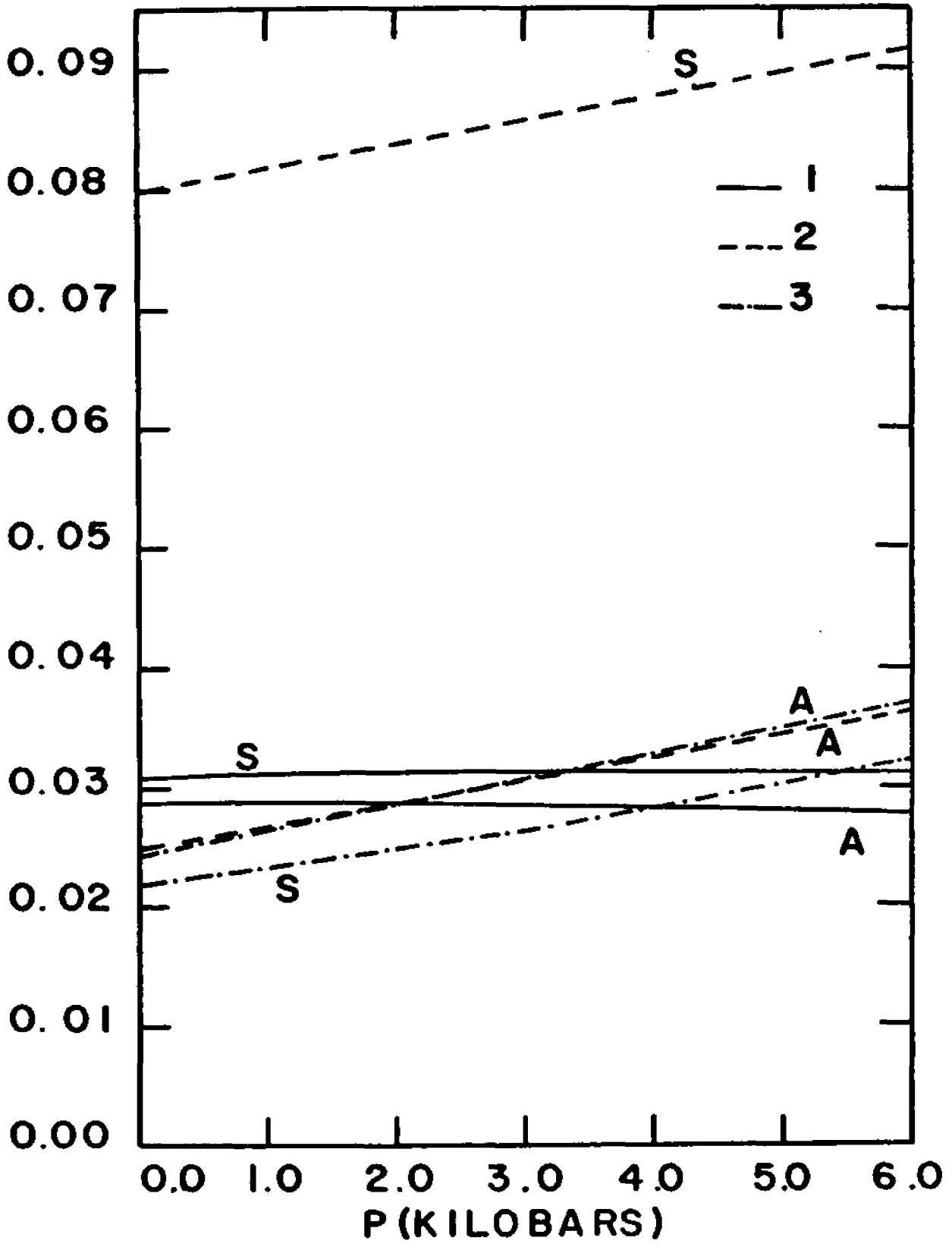
0.09
0.08
0.07
0.06
0.05
0.04
0.03
0.02
0.01
0.00
S
1
2
3
A
A
S
A
S
0.0
1.0
2.0
3.0
4.0
5.0
6.0
P(KILOBARS)

FIG. 4.10

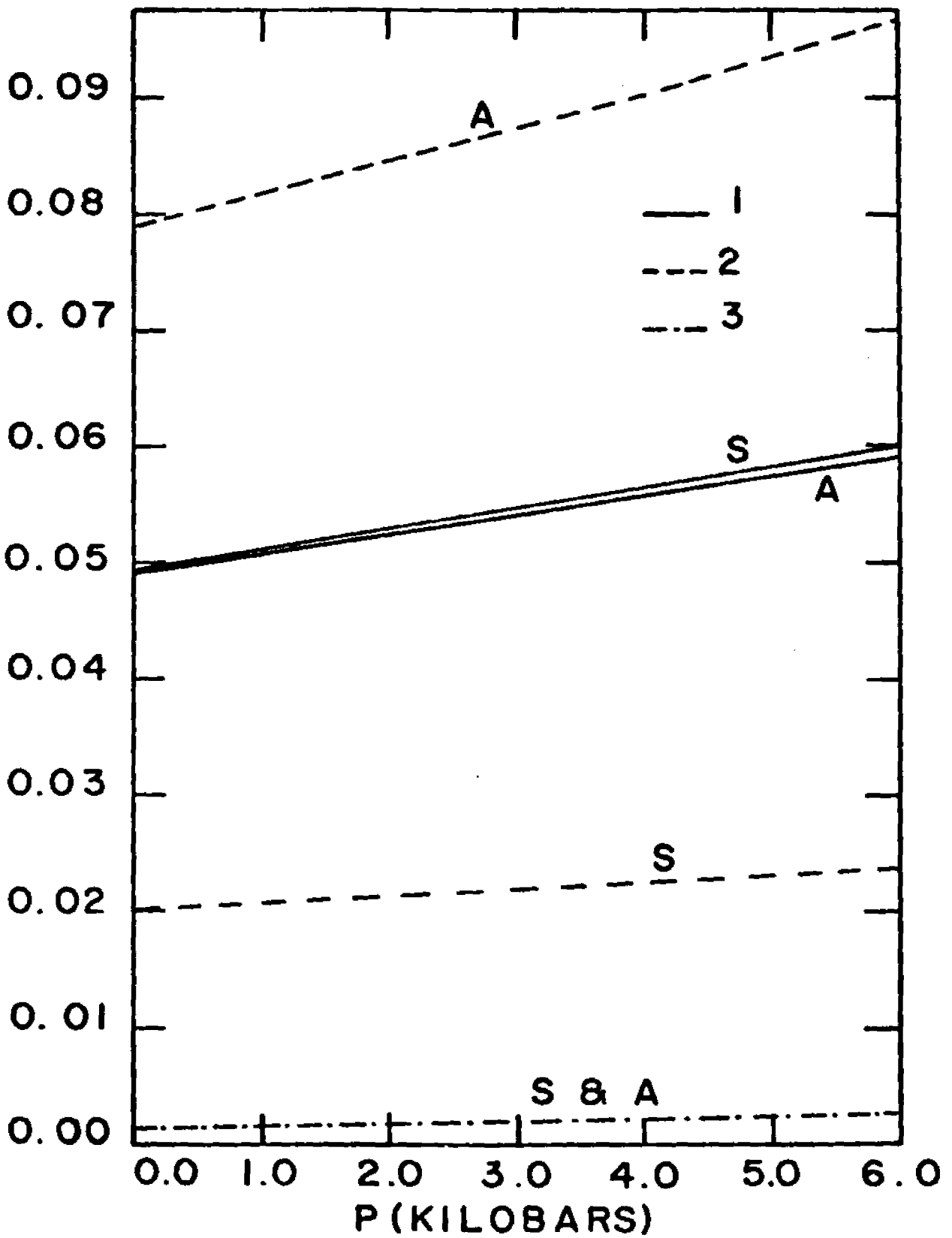
0.09
0.08
0.07
0.06
0.05
0.04
0.03
0.02
0.01
0.00
A
1
2
3
S
A
S
S & A
0.0
1.0
2.0
3.0
4.0
5.0
6.0
P (KILOBARS)

FIG. 4.11

Figures (4.8) and (4.9) give the change of the bandwidths with pressure for both holes and electrons when only two-center integrals are considered. Figures (4.10) and (4.11) include the contribution due to the three-center integrals. We notice that for holes the bandwidths increase appreciably in the $\underline{b}^{-1}$ and $\underline{c}^{-1}$ directions while it hardly changes at all in the $\underline{a}^{-1}$ direction. For electrons the bandwidths increase in all three directions. Although the absolute change in the bandwidths for electrons in the $\underline{c}^{-1}$ direction is very small, yet since the bands are very narrow to start with, such a change is relatively important. Table (4.8), (4.9) and (4.10) give the bandwidths vs. pressure.

II. Mobility Calculations.

(a) Drift mobility.

The drift mobility for electrons was shown in Chapter II to be given by $\mu_{ij} = \frac{-e}{KT} \langle \tau v_i v_j \rangle$

In the simplified model of the constant isotropic relaxation time $\tau(\underline{k}) = \tau_0$. While in the model of a constant mean free path $\tau(\underline{k})|\underline{v}(\underline{k})| = \lambda_0$. Therefore in these two models the drift mobility is given by equations (4.40) and (4.41) respectively

$$\mu_{ij} = \frac{-e\tau_0}{KT} \langle v_i v_j \rangle \qquad (4.40)$$

$$\mu_{ij} = -\frac{e\lambda_0}{KT} \langle v_i v_j / |\underline{v}(\underline{k})| \rangle \qquad (4.41)$$

Since the energy is a periodic function of $\underline{K}$ it suffices to do the integration over the first Brillouin zone. To explain how the calculation was done we show the case of constant relaxation time

$$\langle v_i v_j \rangle = \frac{\int \left\{ \frac{\partial E_+}{\partial K_i} \frac{\partial E_+}{\partial K_j} \exp(-\beta E_+(\underline{k})) + \frac{\partial E_-}{\partial K_i} \frac{\partial E_-}{\partial K_j} \exp(-\beta E_-(\underline{k})) \right\} d\underline{k}}{\hbar^2 \int \left\{ \exp(-\beta E_+(\underline{k})) + \exp(-\beta E_-(\underline{k})) \right\} d\underline{k}} \qquad (4.42)$$

where $\beta = \frac{1}{KT}$

And the region of integration is the first Brillouin zone, as will be shown below. It should be noted that the energy of the hole is measured downward from the top

Table 4.8

Change of bandwidths with pressure
in units of 10^{-1} e.v.

direction	pressure kilobars	symmetric band: 2 and 3-center integrals		symmetric band: 2-center integrals	
		electrons	holes	electrons	holes
$\underline{a}^{-1}$	0.0	0.493	0.309	0.458	0.255
	1.0			0.478	0.257
	2.0	0.526	0.312	0.490	0.258
	3.0			0.506	0.259
	4.0	0.562	0.314	0.523	0.260
	5.0			0.540	0.260
	6.0	0.600	0.311	0.558	0.259
		antisymmetric band			
	0.0	0.491	0.286	0.456	0.238
	1.0			0.471	0.238
	2.0	0.523	0.2855	0.487	0.237
	3.0			0.503	0.236
	4.0	0.557	0.282	0.519	0.235
	5.0			0.535	0.232
	6.0	0.592	0.279	0.552	0.229

Table 4.9

Change of bandwidths with pressure in units of 10^{-1} e.v.

direction	pressure	symmetric band			
		2 and 3-center integrals		2-center integrals	
		electrons	holes	electrons	holes
b^{-1}	0.0	0.203	0.799	0.186	0.704
	1.0			0.192	0.721
	2.0	0.215	0.840	0.197	0.738
	3.0			0.203	0.756
	4.0	0.227	0.879	0.208	0.773
	5.0			0.214	0.791
	6.0	0.239	0.918	0.220	0.808
		antisymmetric band			
	0.0	0.789	0.249	0.738	0.244
	1.0			0.764	0.259
	2.0	0.844	0.283	0.790	0.274
	3.0			0.818	0.290
	4.0	0.904	0.321	0.846	0.308
	5.0			0.875	0.326
	6.0	0.967	0.364	0.905	0.346

Table 4.10

Change of bandwidths with pressure in units of 10^{-1} e.v.

direction	pressure	symmetric band			
		2 and 3-center integrals		2-center integrals	
		electrons	holes	electrons	holes
c^{-1}	0.0	0.0117	0.218	0.008	0.179
	1.0			0.0097	0.192
	2.0	0.0165	0.247	0.0116	0.206
	3.0			0.0137	0.220
	4.0	0.0222	0.282	0.0160	0.236
	5.0			0.0186	0.252
	6.0	0.0279	0.324	0.0214	0.269
		antisymmetric band			
	0.0	0.0138	0.246	0.0109	0.204
	1.0			0.0117	0.219
	2.0	0.0161	0.283	0.0125	0.234
	3.0			0.0134	0.251
	4.0	0.0189	0.324	0.0144	0.268
	5.0			0.0155	0.287
	6.0	0.0223	0.366	0.0167	0.307

of the band and consequently the signs of the hole energy in Tables (4.3) through (4.7) must be changed. We now construct the first Brillouin zone

$$\underline{a}^{-1} = \frac{2\pi(\underline{b}\times\underline{c})}{\underline{a}\cdot(\underline{b}\times\underline{c})} \qquad \text{etc.} \qquad (4.43)$$

where

$$\underline{a} = a\,\hat{a}$$
$$\underline{b} = b\,\hat{b}$$
$$\underline{c} = c\,(\cos(\beta)\,\hat{a} + \sin(\beta)\,\hat{c}') \qquad (4.44)$$

therefore

$$\underline{a}^{-1} = \frac{2\pi}{a\sin(\beta)}\left[\sin(\beta)\hat{a} - \cos(\beta)\,\hat{c}'\right]$$
$$\underline{b}^{-1} = \frac{2\pi}{b}\,\hat{b}$$
$$\underline{c}^{-1} = \frac{2\pi}{c\sin(\beta)}\,\hat{c}' \qquad (4.45)$$

The first Brillouin zone constructed from the reciprocal lattice vectors $\underline{a}^{-1}$, $\underline{b}^{-1}$, and $\underline{c}^{-1}$ is shown in figure (4.1) referred to the orthogonal set of axes $\underline{a}, \underline{b}, \underline{c}'$.

A three dimensional trapezoidal rule integration subroutine was developed by the investigators using 1728 points to evaluate the components of the drift mobility tensor in both the constant relaxation time and the constant mean free path models as well as the change of these components with pressure.

Tables (4.11) through (4.12) give the change of the drift mobility components with pressure for both holes and electrons in the constant relaxation time model. Tables (4.13) through (4.14) give the drift mobility components in the constant free path model. In both models only two-center integrals are considered.

When the contributions of the three-center integrals are taken into account the results are given in Tables (4.15) and (4.16). The results in Tables (4.11) through (4.14) are in good agreement with the calculation done by Katz

Table 4.11

Drift mobility components in units of $10^{10} cm^2/sec^2$. In the constant relaxation time model. Only two center integrals are included.

component	pressure	holes		electrons	
			ratio to atmospheric pressure value		ratio to atm. pressure value
$\langle V_a^2 \rangle$	0.0	77.03	1.000	161.3	1.000
	1.0	78.66	1.021	168.9	1.050
	2.0	80.24	1.042	176.7	1.095
	3.0	81.80	1.062	184.6	1.144
	4.0	83.20	1.080	192.6	1.194
	5.0	84.64	1.099	200.8	1.241
	6.0	85.92	1.115	209.3	1.297
$\langle V_b^2 \rangle$	0.0	197.3	1.000	111.1	1.000
	1.0	207.7	1.053	116.2	1.046
	2.0	218.5	1.108	121.4	1093
	3.0	229.6	1.164	126.8	1.141
	4.0	241.8	1.226	132.3	1.190
	5.0	253.9	1.287	137.9	1.241
	6.0	267.2	1.354	143.7	1.293

Table 4.12

Drift mobility components in units of $10^{10} cm^2/sec^2$. In the constant relaxation time model. Only two center integrals are included.

component	pressure	holes	ratio to atm. pressure value	electrons	ratio to atm. pressure value
$\langle V_{c1}^2 \rangle$	0.0	32.64	1.000	.088	1.000
	1.0	36. 8	1.124	.124	1.410
	2.0	41.19	1.262	.175	1.979
	3.0	46.21	1.416	.241	2.726
	4.0	51.76	1.586	.327	3.698
	5.0	57.93	1.775	.438	4.951
	6.0	64.69	1.982	.579	6.549
$\langle V_a V_{c1} \rangle$	0.0	-6.83	1.000	-.0237	1.000
	1.0	-7.75	1.135	-.0388	1.635
	2.00	-8.79	1.287	-.0608	2.565
	3.00	-9.94	1.455	-.0896	3.777
	4.0	-11.20	1.64	-.127	5.367
	5.0	-12.62	1.848	-.177	7.485
	6.0	-14.19	2.077	-.244	10.23

Table 4.13
Drift mobility components in the constant mean free path model in units of 10^5 cm/sec. Only two center integrals are included.

component	pressure	holes	ratio to atm. pressure value	electrons	ratio to atm. pressure value
$\langle V_a^2 \vert \underline{V} \vert \rangle$	0.0	3.966	1.000	8.762	1.000
	1.0	3.942	0.994	8.966	1.023
	2.0	3.916	0.988	9.169	1.047
	3.0	3.886	0.980	9.371	1.070
	4.0	3.849	0.970	9.571	1.092
	5.0	3.813	0.961	9.770	1.115
	6.0	3.768	0.950	9.973	1.138
$\langle V_b^2 \vert \underline{V} \vert \rangle$	0.0	9.608	1.000	5.803	1.000
	1.0	9.866	1.027	5.916	1.019
	2.0	10.13	1.054	6.029	1.039
	3.0	10.39	1.081	6.143	1.058
	4.0	10.66	1.110	6.256	1.078
	5.0	10.935	1.138	6.368	1.097
	6.0	11.22	1.168	6.481	1.117

Table 4.14

Drift mobility components in the constant mean free path model in uints of 10^5 cm/sec. Only two center integrals are included.

component	pressure	holes	ratio to atm. pressure value	electrons	ratio to atm. pressure value
$\langle V_c^3 \| \underline{V} \| \rangle$	0.0	2.029	1.000	.009	1.000
	1.0	2.199	1.083	.0131	1.432
	2.0	2.380	1.173	.0184	2.019
	3.0	2.574	1.269	.0251	2.757
	4.0	2.777	1.369	.0336	3.684
	5.0	2.995	1.476	.0441	4.839
	6.0	3.221	1.588	.0572	6.267
$\langle V_a V_c' \| \underline{V} \| \rangle$	0.0	-0.282	1.000	.0025	1.000
	1.0	-0.312	1.108	-0.0033	-1.342
	2.0	-0.345	1.224	-.0044	-1.789
	3.0	-0.380	1.349	-.0058	-2.358
	4.0	-0.417	1.481	-.0076	-3.078
	5.0	-0.458	1.625	-.0097	-3.973
	6.0	-0.501	1.778	-.0125	-5.086

Table 4.15

Drift mobility components in the constant relaxation time model in units of $10^{10} cm^2/sec^2$. Two and three center integrals are included.

component	pressure	holes	ratio to atm. pressure value	electrons	ratio to atm. pressure value
$\langle V_a^2 \rangle$	0.0	107.2	1.000	183.6	1.000
	2.0	111.5	1.040	200.8	1.094
	4.0	115.0	1.073	218.7	1.191
	6.0	118.3	1.104	237.5	1.294
$\langle V_b^2 \rangle$	0.0	229.5	1.000	121.7	1.000
	2.0	253.3	1.104	132.5	1.089
	4.0	279.7	1.219	143.9	1.182
	6.0	308.2	1.343	155.9	1.281
$\langle V_{c1}^2 \rangle$	0.0	48.05	1.000	.1697	1.000
	2.0	60.62	1.262	.3285	1.936
	4.0	75.48	1.571	.5873	3.461
	6.0	91.94	1.913	.959	5.653
$\langle V_a V_{c1} \rangle$	0.0	-9.976	1.000	-.048	1.000
	2.0	-12.86	1.290	-.113	2.359
	4.0	-16.22	1.63	-.222	4.635
	6.0	-20.36	2.041	-.396	8.262

Table 4.16

Drift mobility components in the constant mean free path model in units of 10^5cm/sec.

component	pressure	holes	ratio to atm. pressure value	electrons	ratio to atm. pressure value
$\langle v_a^2 \vert \underline{v} \vert \rangle$	0.0	4.886	1.000	9.389	1.000
	2.0	4.828	0.988	9.818	1.046
	4.0	4.733	0.969	10.247	1.091
	6.0	4.636	0.949	10.67	1.137
$\langle v_b^2 \vert \underline{v} \vert \rangle$	0.0	9.946	1.000	6.014	1.000
	2.0	10.46	1.051	6.235	1.037
	4.0	11.01	1.107	6.455	1.073
	6.0	11.59	1.165	6.673	1.110
$\langle v_c^2 \vert \underline{v} \vert \rangle$	0.0	2.657	1.000	.0175	1.000
	2.0	3.107	1.169	.0337	1.920
	4.0	3.595	1.353	.0580	3.306
	6.0	4.069	1.531	.0894	5.095
$\langle v_a v_c \vert \underline{v} \rangle$	0.0	-0.370	1.000	-.0040	1.000
	2.0	-0.448	1.210	-.0069	1.719
	4.0	-0.5371	1.450	-.01145	2.844
	6.0	-0.647	1.748	-.01789	4.44

et al except for the following differences:

i. The mobility calculated by Katz in the c' direction for holes seems to be systematically smaller than our mobility by a factor of 2. This was also the case for naphthalene. Therefore we believe that Katz had a mistake in his calculation which introduced that factor of 2. As will be discussed below this correction brings the calculated anisotropy of the mobility at atmospheric pressure closer to the experimental values.

ii. Katz seems to have a mistake in the sign of $\langle V_a V_{c'} | V | V \rangle$ for holes but the absolute value is in agreement with our value.

Figures (4.12) through (4.15) give the change of the drift mobility tensor for both holes and electrons with pressure in the constant relaxation time and constant mean free path models. In these figures only two-center integrals were considered.

In Figures (4.16) through (4.19) the contribution of the three-center integrals were considered as well.

Comparison with experiment

As mentioned before, Kepler[19] measured the drift mobility for holes and for electrons in anthracene as well as its change with pressure at 3 kilobars. More recently Takashi et al[20] measured the drift mobility of electrons in anthracene as a function of pressure up to 6.6 kilobars. In order to facilitate the comparison of the calculation of this work with the experimental data we tabulate our calculated mobilities at atmospheric pressure and the experimental values in Table 4.17.

Figure captions

Figure 4.12 gives the change of the components of the drift mobility tensor of holes in the constant relaxation time model with pressure.

Figure 4.13 gives case for electrons.

figures 4.14 and 4.15 give the change of the mobility components for holes and electrons respectively in the constant mean free path model.

In figures 4.12 through 4.15 only two-center integrals were included. When two and three-center integrals are included figures 4.16 through 4.19 give the corresponding quantities respectively.

In figures 4.12 through 4.19 the vertical axis gives the ratio of the components of mobility at a pressure p to their values at $p=0$.

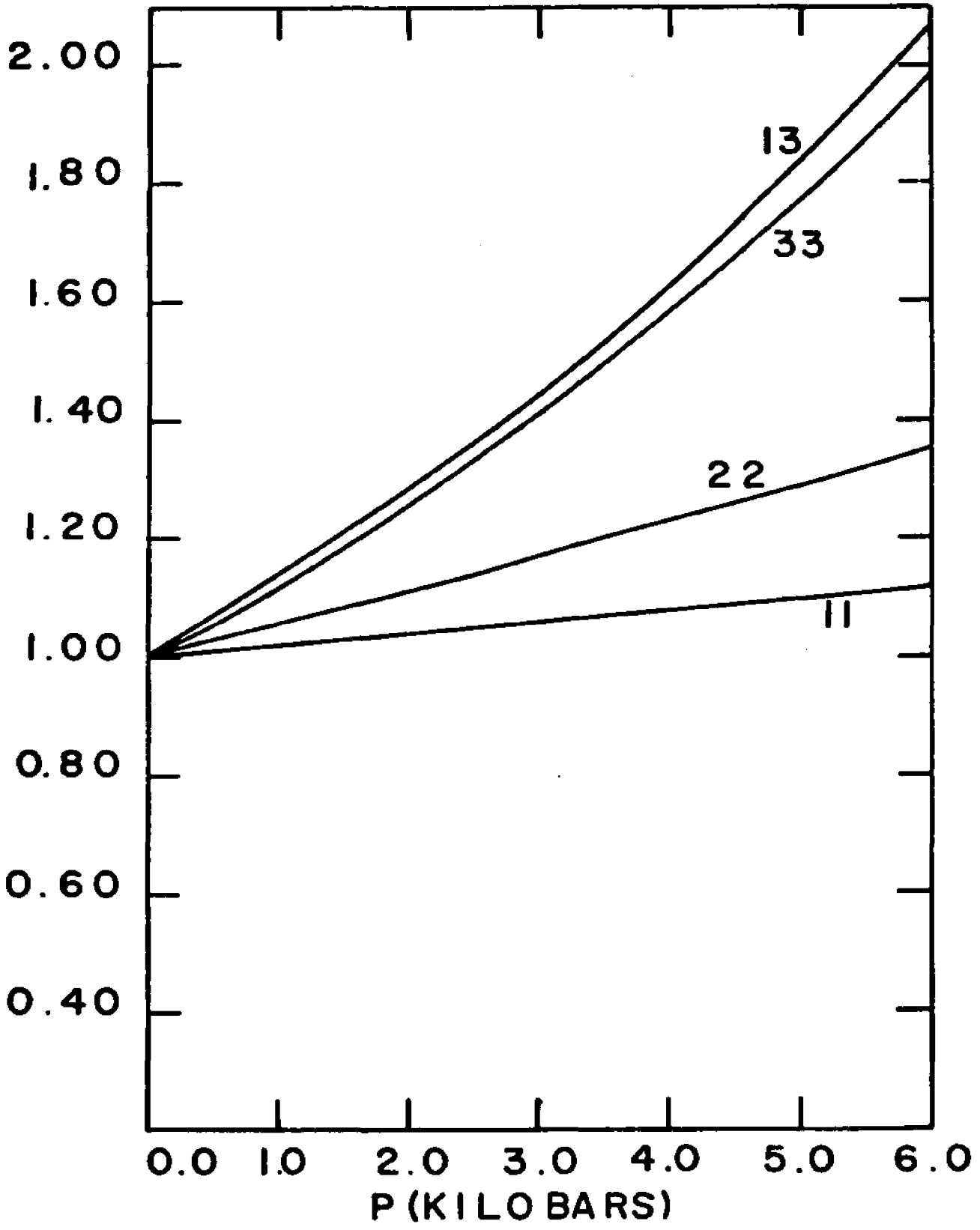
2.00
1.80
1.60
1.40
1.20
1.00
0.80
0.60
0.40
13
33
22
11
0.0
1.0
2.0
3.0
4.0
5.0
6.0
P (KILOBARS)

FIG. 4.12

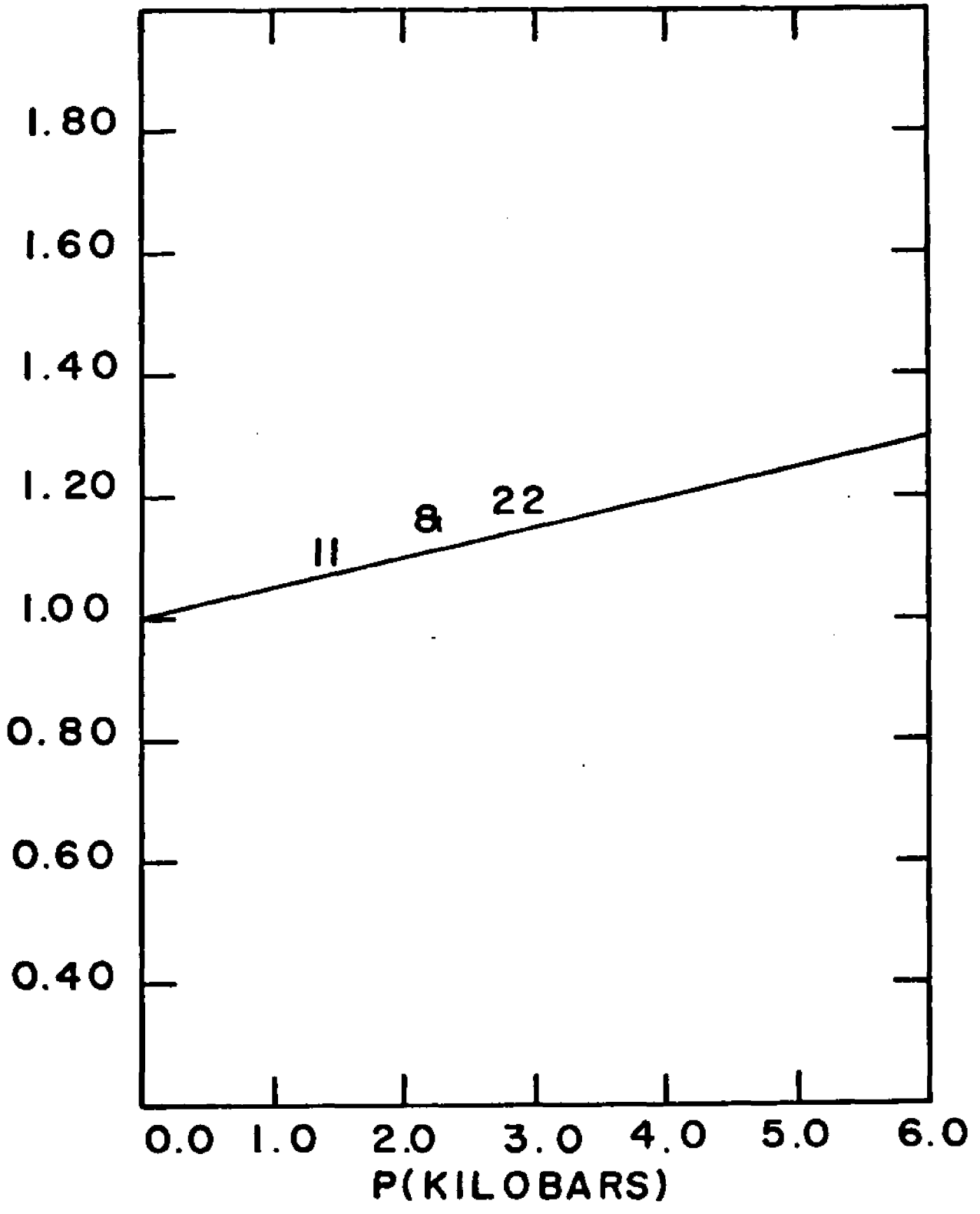
1.80
1.60
1.40
1.20
1.00
0.80
0.60
0.40
11 & 22
0.0 1.0 2.0 3.0 4.0 5.0 6.0
P(KILOBARS)

FIG. 4.13

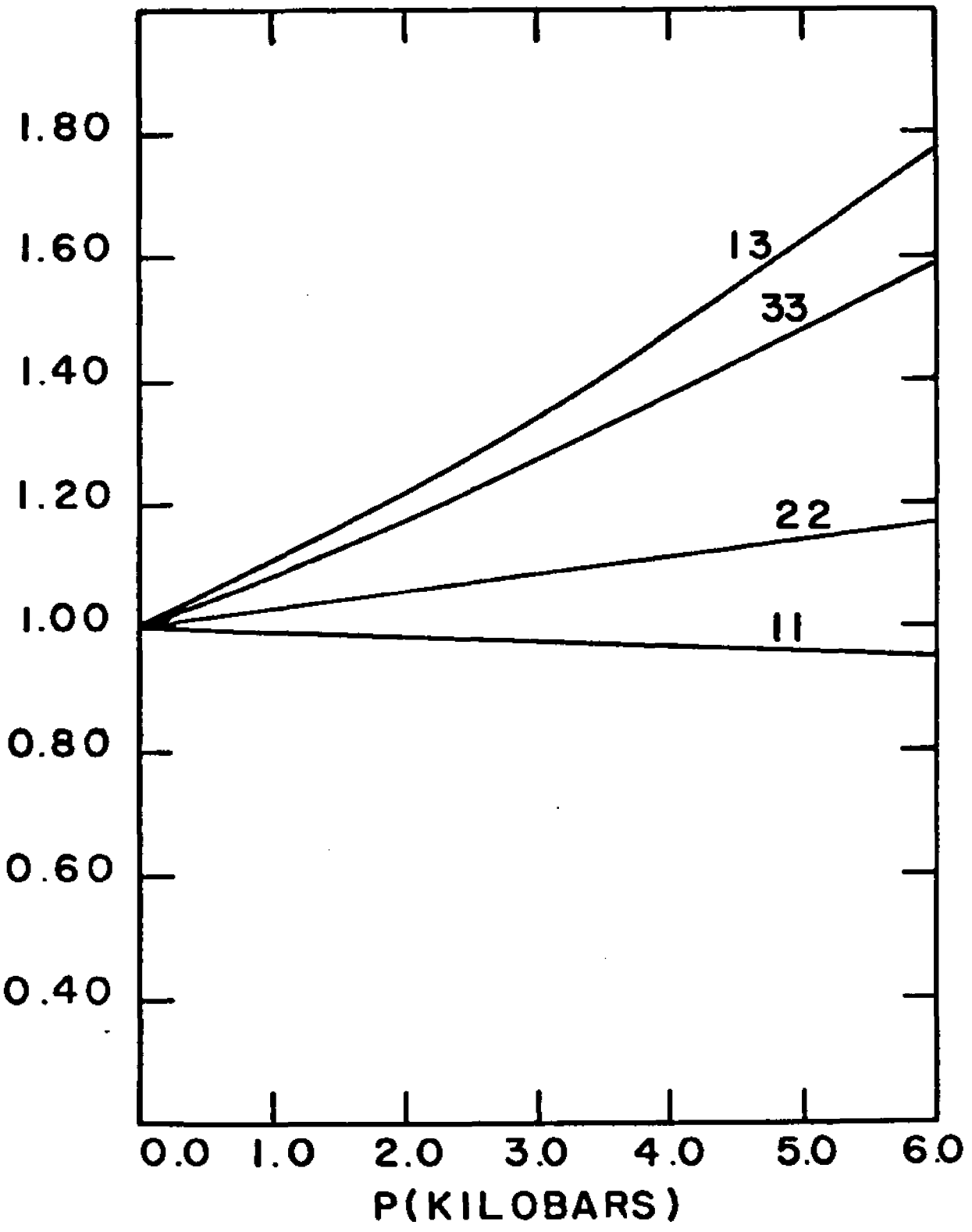
1.80
1.60
1.40
1.20
1.00
0.80
0.60
0.40
13
33
22
11
0.0
1.0
2.0
3.0
4.0
5.0
6.0
P(KILOBARS)

FIG. 4.14

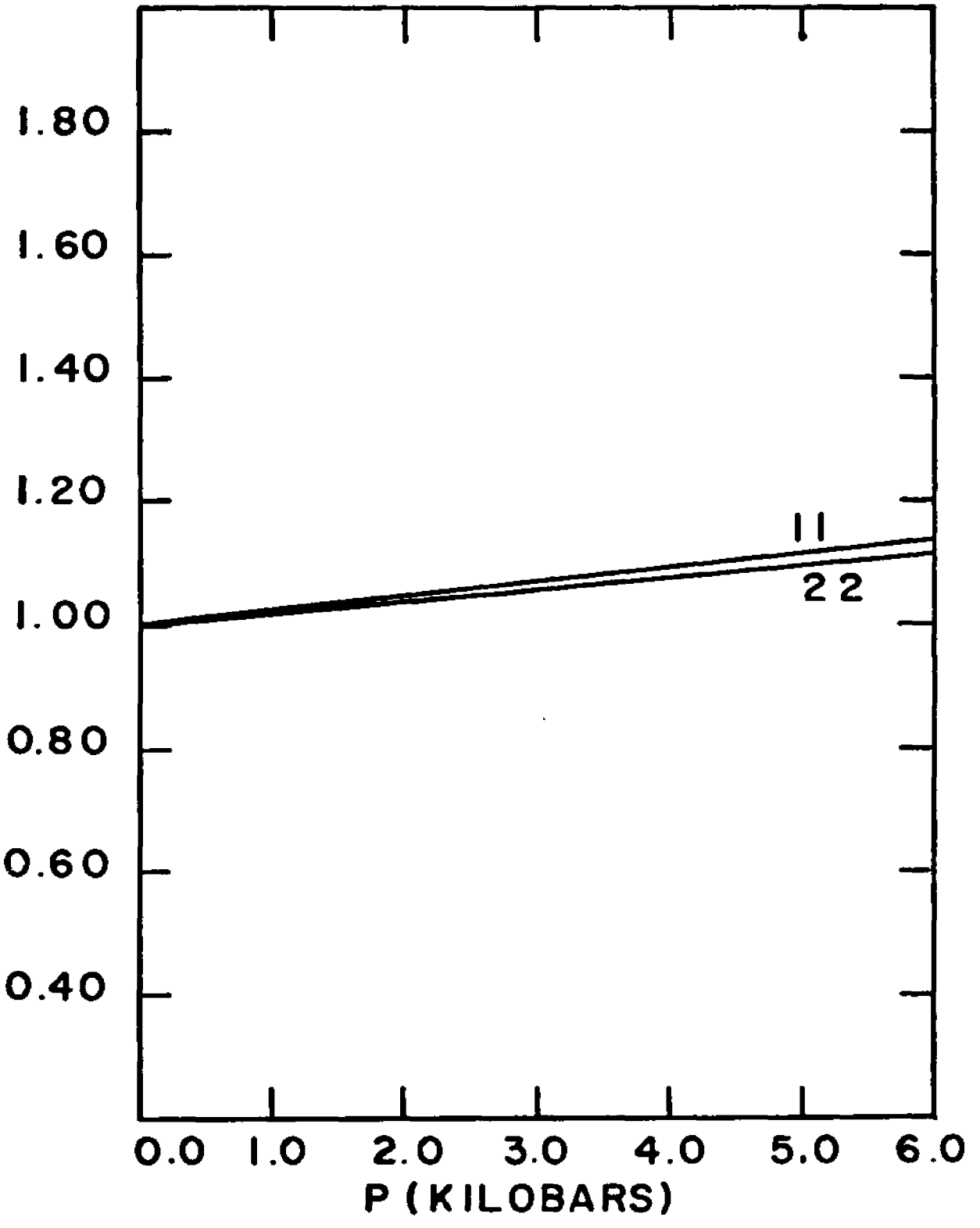
1.80
1.60
1.40
1.20
1.00
0.80
0.60
0.40
11
22
0.0
1.0
2.0
3.0
4.0
5.0
6.0
P (KILOBARS)

FIG. 4.15

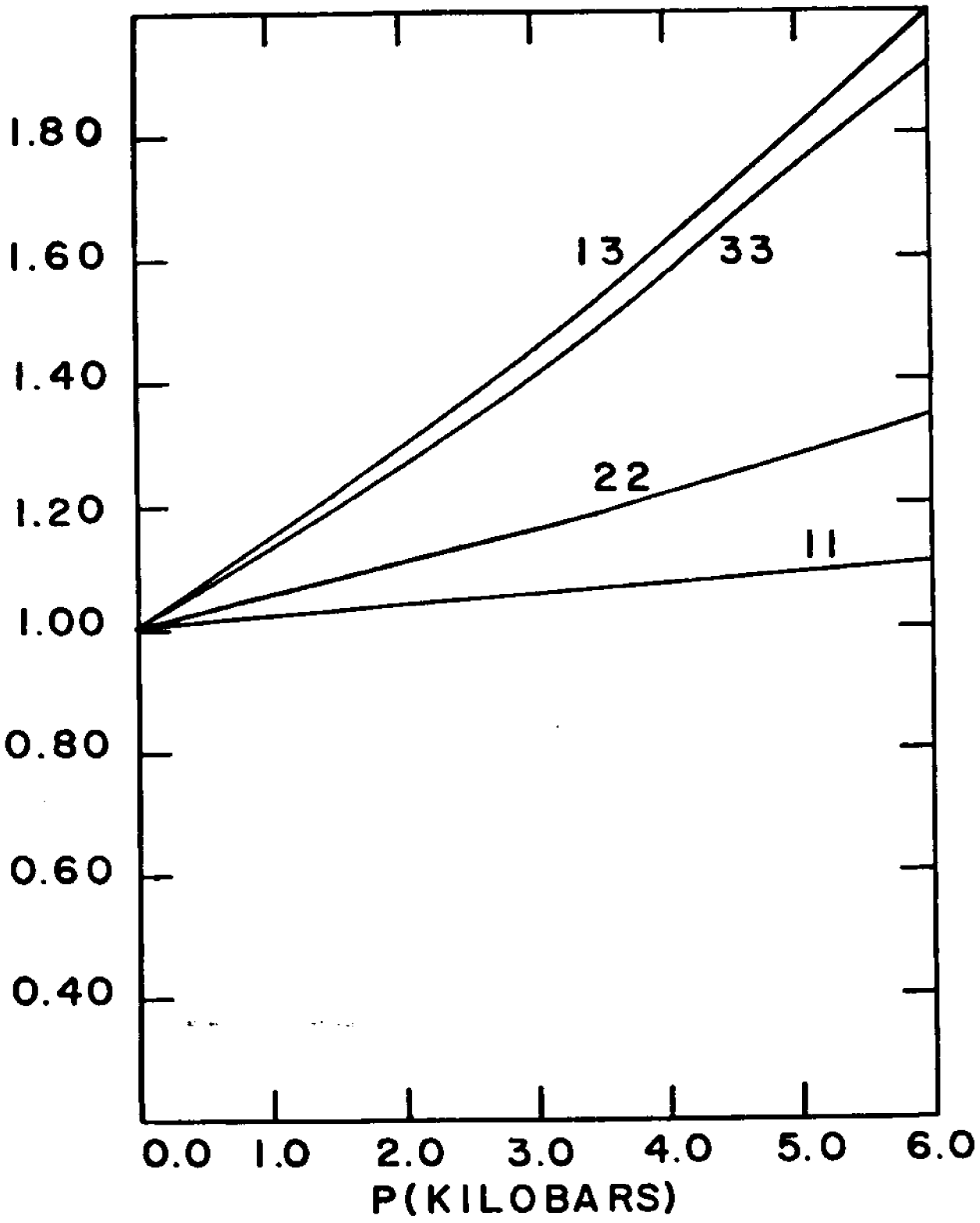
1.80
1.60
1.40
1.20
1.00
0.80
0.60
0.40
13
33
22
11
0.0
1.0
2.0
3.0
4.0
5.0
6.0
P(KILOBARS)

FIG. 4.16

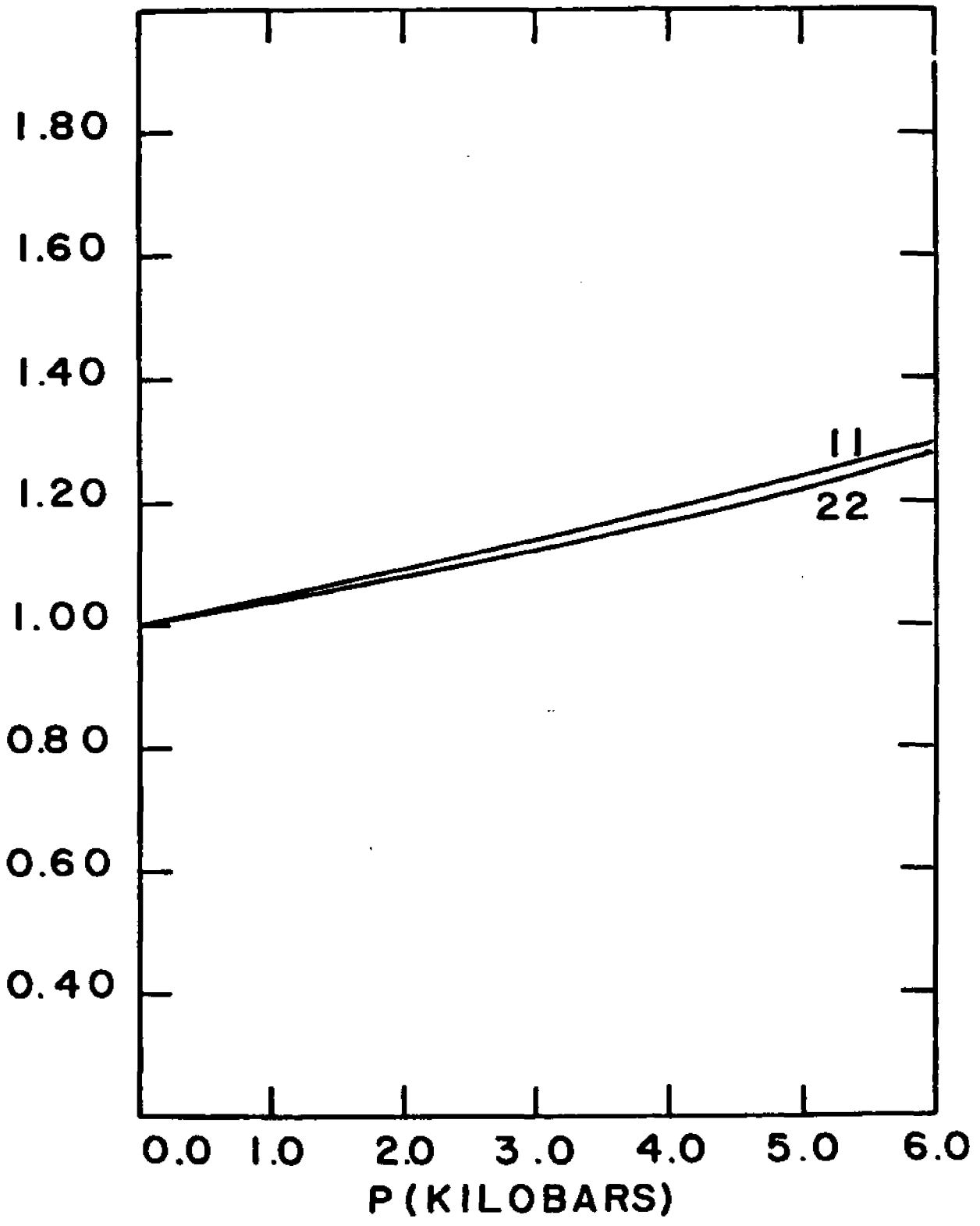
1.80
1.60
1.40
1.20
1.00
0.80
0.60
0.40
11
22
0.0
1.0
2.0
3.0
4.0
5.0
6.0
P(KILOBARS)

FIG. 4.17

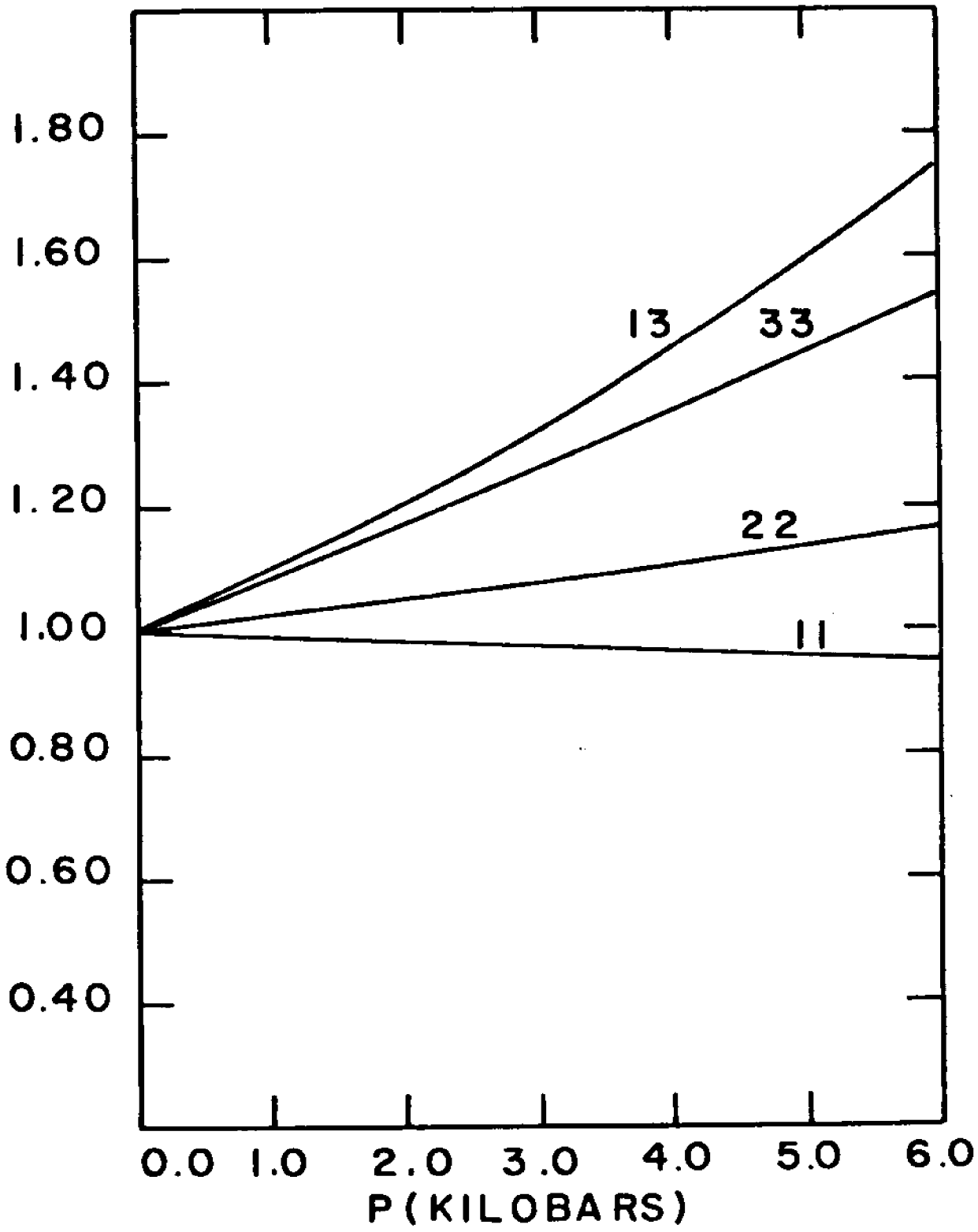
1.80
1.60
1.40
1.20
1.00
0.80
0.60
0.40
13
33
22
11
0.0
1.0
2.0
3.0
4.0
5.0
6.0
P(KILOBARS)

FIG.4.18

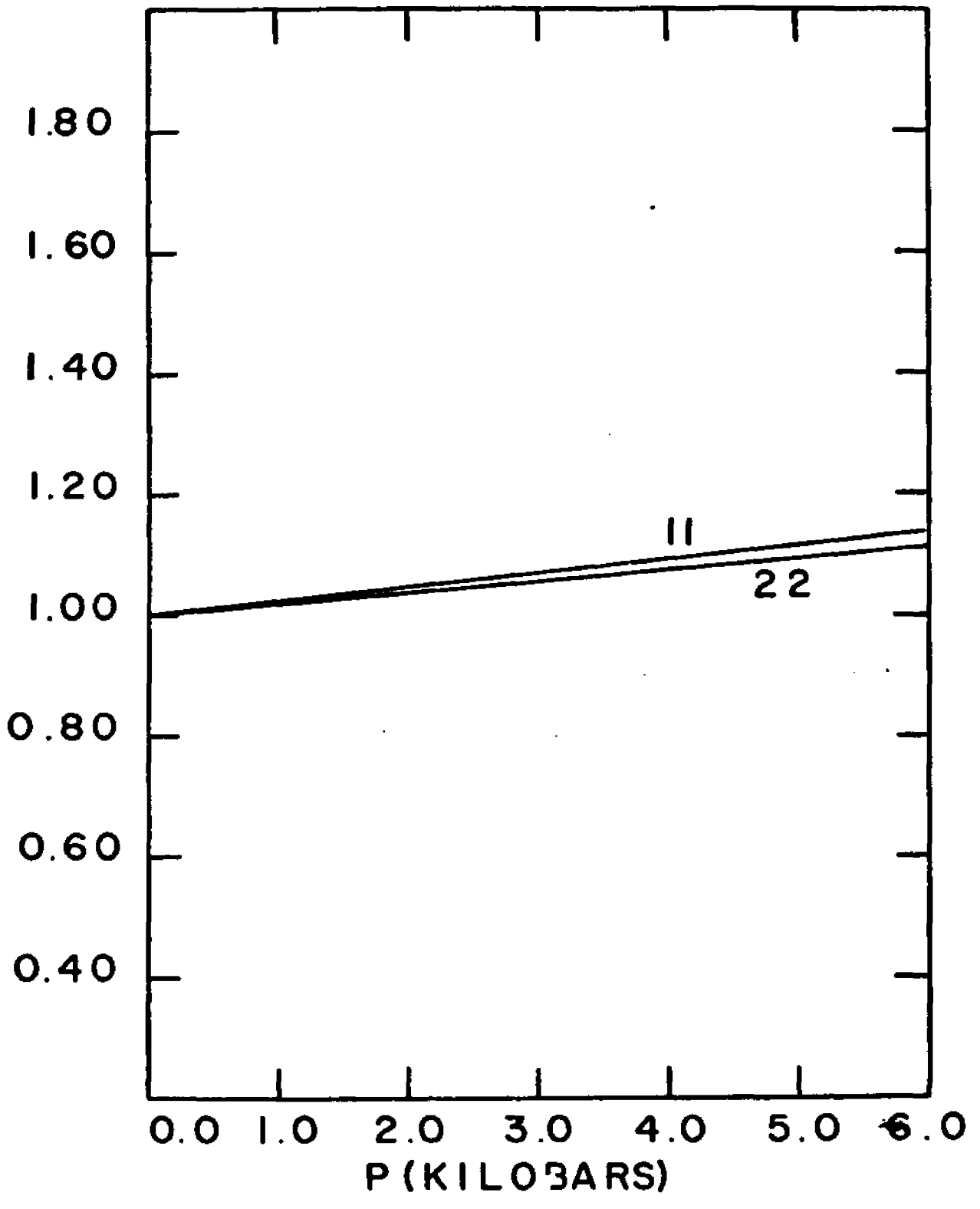
1.80
1.60
1.40
1.20
1.00
0.80
0.60
0.40
11
22
0.0
1.0
2.0
3.0
4.0
5.0
6.0
P (KILOBARS)

FIG. 4.19

Table 4.17

Comparison of the theoretical and experimental anisotropy of the drift mobility of anthracene at atmospheric pressure.

	two and three-center integrals		two-center integrals		experimental value	
	constant γ	constant λ	constant γ	constant λ	I	II
	holes					
μ_a	1.00	1.00	1.00	1.00	1	
μ_b	2.1	2.0	2.56	2.4	2.0	
$\mu_{c'}$	0.45	0.54	0.42	0.51	0.8	
	electrons					
μ_a	1.00	1.00	1.00	1.00	1.0	1.0
μ_b	0.66	0.64	0.69	0.66	0.59	0.64
$\mu_{c'}$	0.001	0.002	0.0005	0.001	0.23	0.28

I. Kepler

II. Takashi Kajiwara et al

The ratio of the mobilities at 3 kilobars to the atmospheric pressure values are tabulated in Table 4.18.

From Table 4.18 we see that the constant free path model predicts no change of the mobility with pressure in the a direction for hole contrary to the experimentally observed increase. Therefore we conclude that this model is not appropriate to describe the drift mobility. On the other hand the constant relaxation time model predicts that the mobility increases in all three directions in a qualitative agreement with experiment. In fact this model gives the exact value of the change of the drift mobility of holes in the c′ direction as that determined experimentally. However, it gives a smaller change in the mobility in the a and b directions than the experimental data. For the case of electrons the model also gives an increase in the mobility in the a and b directions in qualitative agreement with experiment, although the increase is also smaller than that found experimentally. The model fails however to describe the mobility of electrons in the c′ direction. However, no theoretical calculation have succeeded in predicting the correct value of the mobility in this direction. Going back to Table 4.17 we find that the anisotropy of the mobility of holes in the ab plane as calculated in the constant relaxation time model is in excellent agreement with the experimental data. However in the c′ direction the model gives a mobility smaller than the experimental value by about 45%. However it should be noted here that in spite of this difference this value of mobility is closer than any theoretical value available in the literature to the experimental value of mobility in the c′ direction. For electrons the anisotropy in the ab plane is again in very good agreement with experiment.

We would also like to point out here that the difference between the theoretical and experimental value of the drift mobility of the holes in the c′ direction might be due to the simple assumption of an isotropic relaxation time.

Table 4.18

Comparison of the theoretical and experimental dependence of the drift mobility of anthracene on pressure at 3 kilobars

	Two and three-center integrals		Two-center integrals		Experimental value	
	constant τ	constant λ	constant τ	constant λ	I	II
			holes			
μ_a/μ_{a0}	1.06	0.98	1.062	0.98	1.4	
μ_b/μ_{b0}	1.16	1.075	1.16	1.08	1.4	
$\mu_{c'}/\mu_{c'0}$	1.41	1.26	1.42	1.269	1.4	
			electrons			
μ_a/μ_{a0}	1.14	1.07	1.14	1.07	1.4	1.33
μ_b/μ_{b0}	1.135	1.055	1.14	1.06	1.3	1.26
$\mu_{c'}/\mu_{c'0}$	— —	— —	— —	— —	1.0	1.0

We now test the band model for internal consistency. The uncertainity in the energy given by $\hbar/\tau$ must be smaller than the band width. By comparing the present theoretical values of the mobility in the ab plane with the experimental ones we find that ($\tau = 2.3 \times 10^{-14}$ sec.) for holes and electrons. Therefore $\Delta E = \frac{\hbar}{\tau} = .027$ e.v. a value comparable with the bandwidths in the ab plane.

Therefore we conclude that the band theory in the constant relaxation time model, other than failing to give the experimental value of the drift mobility of electrons in the c′ direction, gives the closest theoretical approximation to the values of the components of the drift mobility tensor as well as their change with pressure.

The polaron model used by Glaeser and Berry does not yield as good values for the anisotropy of the drift mobility at atmospheric pressure as our band calculation. Furthermore, their rejection of the band model as being internally inconsistent is rendered invalid by the above calculation.

A refinement of the band model might resolve the remaining differences between theory and experiment.

(b) Hall Mobility

It was shown in Chapter II that the Hall mobility is given by

$$\mu_H \Big|_{\substack{B\parallel z \\ I\parallel x}} = \frac{q}{2} \frac{\langle \tau^2 (V_x^2 M^{-1}_{yy} + V_y^2 M^{-1}_{xx} - 2 V_x V_y M^{-1}_{yx}) \rangle}{\langle \tau V_y^2 \rangle} \qquad (4.46)$$

Where the averaging processes are done over the first Brillouin zone because of the periodicity of the energy as explained before.

LeBlanc(21) evaluated the ratio of the Hall mobility, for the magnetic field parallel to the c′ axis, to the drift mobility by numerical integration in the constant

relaxation time model using Thaxton's intermolecular resonance energy .He also found an approximate analytical expression for the ratio of the Hall to the drift mobility for that direction of the magnetic field. This approximation is valid fo $KT \gg W$, the bandwidth. Thaxton's and Katz's energies predict $\mu_H/\mu_D \simeq -8$ and $\mu_H/\mu_D \simeq -1$, respectively for electrons and holes at room temperature. The negative sign of μ_H/μ_D means that carriers rotate in the wrong direction in the magnetic field and it results from the fact that states with negative effective mass are weighted more heavily in the numerator of equation (4.46) than those with positive effective mass.

Toombs[22] did a crude numerical evaluation of for all possible six directions of the current and the magnetic field using Katz' energies in the constant relaxation time model. His results show that the Hall mobility for both holes and electrons is anomalous in sign when the magnetic field is parallel to the a or c' directions.

In this investigation we have done a complete numerical evaluation of the Hall mobility in the six different directions as well as their change with pressure. The calculations were done in both the constant relaxation time model and the constant mean free path model. In every model the mobilities were calculated using two and three-center integrals and,for comparison,using two-center integrals only.

A trapezoidal rule three-dimensional integration subroutine similar to that used to evaluate the drift mobility was used.

Table (4.19) gives the Hall mobilities for holes and electrons in the constant relaxation time model. This table confirms that in this model the Hall mobility is anomalous in sign for both holes and electrons.when the magnetic field is parallel to a or c'.

Tables (4.21) and (4.22) give the Hall mobilities when

the constant mean free path model is used. The results predict anomalous Hall mobility for holes only when the magnetic field is parallel to the $\underline{c}'$ axis while it predicts no anomaly for electrons.

In Tables (4.19) through (4.22) only two-center integrals in the evaluation of the energy were used. Tables (4.23) through (4.24) give the same quantities when the three-center integrals were considered as well. The anomalies predicted are the same as those of the case of the two-center integrals only.

The ratios of the Hall mobility at different pressures to that at atmospheric pressure given in Tables (4.19) through (4.24) are plotted against pressure in Figures (4.20) through (4.31).

Fig. (4.31) shows that the constant mean free path model predicts that, for electrons when the current is parallel to the b-axis and the magnetic field is parallel to the a-axis, the Hall mobility goes through a maximum at about 2.5 kilobars and a minimum at about 5 kilobars. Such a behavior can easily be verified once a reliable technique is available to measure the Hall mobility in anthracene.

Unfortunately no definite experimental verification for the values of the Hall mobilities in different directions or their pressure dependence is available yet. The reason being the difficulties involved in that kind of a measurement as is discussed in Chapter V.

Table 4.19

Hall mobility* in the constant relaxation time in units of $10^{14} cm^2/sec^2.volt$. Only two center integrals are included.

direction	pressure kilobars	holes	ratio to atm. pressure value	electrons	ratio to atm. pressure value
I//b	0.0	-1.520	1.000	.690	1.000
B//c′	1.0	-1.543	1.015	.692	1.003
	2.0	-1.564	1.029	.694	1.006
	3.0	-1.583	1.041	.695	1.008
	4.0	-1.603	1.055	.696	1.008
	5.0	-1.620	1.066	.695	1.008
	6.0	-1.638	1.077	.694	1.006
I//a	0.0	- 0.594	1.000	1.003	1.000
B//c′	1.0	- 0.585	0.984	1.007	1.004
	2.0	- 0.575	0.967	1.011	1.008
	3.0	- 0.564	0.949	1.013	1.010
	4.0	- 0.5519	0.929	1.014	1.011
	5.0	- 0.540	0.909	1.014	1.011
	6.0	- 0.527	0.887	1.012	1.001
I//c′	0.0	0.430	1.000	-0.00	
B//b	1.0	0.484	1.124		
	2.0	0.543	1.260		
	3.0	0.609	1.414		
	4.0	0.682	1.583		
	5.0	0.762	1.770		
	6.0	0.850	1.974		

* In all tables of Hall mobility at constant τ we are actually giving the ratio μ_H/τ as can be seen from the units.

Table 4.20

Hall mobility in the constant relaxation time model in units of 10^{14} cm^2/sec^2.volt. Only two center integrals are included

direction	pressure kilobars	holes	ratio to atm. pressure value	electrons	ratio to atm. pressure value
B ||b	0.0	1.017	1.000	-0.982	1.000
I ||a	1.0	1.037	1.020	-1.212	1.234
	2.0	1.057	1.040	-1.400	1.422
	3.0	1.076	1.059	-1.541	1.569
	4.0	1.095	1.077	-1.658	1.688
	5.0	1.113	1.095	-1.755	1.787
	6.0	1.130	1.112	-1.844	1.878
I ||c'	0.0	-0.190	1.000	0.000	
B ||a	1.0	-0.206	1.082		
	2.0	-0.223	1.170		
	3.0	-0.241	1.262		
	4.0	-0.259	1.358		
	5.0	-0.278	1.460		
	6.0	-0.298	1.564		
I ||b					
B ||a	0.0	-1.153	1.000	0.396	1.000
	1.0	-1.168	1.014	0.240	0.605
	2.0	-1.183	1.026	0.111	0.281
	3.0	-1.196	1.038	0.006	0.016
	4.0	-1.210	1.049	-0.083	-0.210
	5.0	-1.220	1.058	-0.157	-0.398
	6.0	-1.231	1.068	-0.223	-0.564

Table 4.21

Hall mobility* in the constant mean free path model in units of 10^7 cm/volt.sec. Only two-center integrals are included.

direction	pressure kilobars	holes	ratio to atm. pressure value	electrons	ratio to atm. pressure value
I // b	0.0	-1.590	1.000	-0.459	1.000
B // c′	1.0	-1.492	0.939	-0.562	1.225
	2.0	-1.410	0.886	-0.664	1.448
	3.0	-1.318	0.829	-0.767	1.672
	4.0	-1.212	0.763	-0.874	1.906
	5.0	-1.098	0.690	-0.970	2.114
	6.0	-0.976	0.614	-1.077	2.349
I // a	0.0	7.847	1.000	-37.51	1.000
B // b	1.0	7.714	0.983	-34.71	0.925
	2.0	7.591	0.967	-32.66	0.871
	3.0	7.477	0.953	-33.28	0.887
	4.0	7.342	0.936	-30.25	0.806
	5.0	7.207	0.918	-28.54	0.761
	6.0	7.067	0.901	-28.019	0.747
I // a	0.0	-0.656	1.000	-0.692	1.000
B // c′	1.0	-0.596	0.909	-0.851	1.229
	2.0	-0.545	0.830	-1.010	1.459
	3.0	-0.493	0.751	-1.170	1.690
	4.0	-0.4375	0.667	-1.337	1.931
	5.0	-0.383	0.583	-1.487	2.148
	6.0	-0.328	0.499	-1.658	2.394

* In all tables of Hall mobility at constant λ we are actually giving the ratio μ_H/λ as can be seen from the units.

Table 4.22

Hall mobility in the constant mean free path model in units of 10^7 cm/volt.sec. Only two-center integrals are included.

direction	pressure kilobars	holes	ratio to atm. pressure value	electrons	ratio to atm. pressure value
I // c′	0.0	4.014	1.000	-.039	1.000
B // b	1.0	4.302	1.072	-.051	1.301
	2.0	4.614	1.149	-.066	1.680
	3.0	4.951	1.233	-.089	2.288
	4.0	5.297	1.320	-.106	2.720
	5.0	5.661	1.410	-.128	3.302
	6.0	6.041	1.505	-.1606	4.11
I // c′	0.0	0.183	1.000	-.005	1.000
B // a	1.0	0.232	1.269	-.011	2.212
	2.0	0.278	1.521	-.020	3.939
	3.0	0.322	1.764	-.026	5.138
	4.0	0.370	2.027	-.033	6.638
	5.0	0.420	2.301	-.043	8.628
	6.0	0.475	2.601	-.054	10.69
I // b	0.0	0.865	1.000	-3.188	1.000
B // a	1.0	1.040	1.202	-4.999	1.568
	2.0	1.182	1.367	-6.461	2.027
	3.0	1.300	1.503	-6.285	1.971
	4.0	1.422	1.644	-6.191	1.942
	5.0	1.534	1.774	-6.238	1.957
	6.0	1.655	1.914	-6.070	1.904

Table 4.23

Hall mobility in the constant relaxation time model in units of $10^{14} cm^2/volt.sec^2$

Two and three- center integrals are included

direction	pressure kilobars	holes	ratio to atm. pressure value	electrons	ratio to atm. pressure value
I b	0.0	-1.505	1.000	0.672	1.000
B c′	2.00	-1.541	1.024	0.671	0.998
	4.0	-1.570	1.043	0.666	0.991
	6.0	-1.593	1.058	0.658	0.979
I a	0.0	-0.704	1.000	1.015	1.000
B c′	2.0	-0.679	0.965	1.017	1.002
	4.0	-0.646	0.918	1.013	0.998
	6.0	-0.612	0.870	1.003	0.989
I c′	0.0	0.607	1.000	-.0014	1.000
B b	2.0	0.770	1.268	-.0030	2.174
	4.0	0.957	1.576	-.0056	3.991
	6.0	1.147	1.890	-.0087	6.247
I a	0.0	1.355	1.000	-1.439	1.000
B b	2.0	1.414	1.044	-1.782	1.238
	4.0	1.456	1.075	-2.013	1.399
	6.0	1.477	1.090	-2.103	1.461
I c′	0.0	-0.216	1.000	0.000	
B a	2.0	-0.255	1.182		
	4.0	-0.292	1.355		
	6.0	-0.336	1.558		
I b	0.0	-1.030	1.000	0.253	1.000
B a	2.0	-1.064	1.033	0.025	0.0997
	4.0	-1.082	1.051	-0.134	-0.531
	6.0	-1.126	1.093	-0.248	-0.981

Table 4.24

Hall mobility in the constant mean free path model in units of 10^7 cm/volt.sec. Two and three-integrals are included

direction	pressure kilobars	holes	ratio to atm. pressure value	electrons	ratio To atm. pressure value
I b	0.0	-0.759	1.000	-0.753	1.000
B c′	2.0	-0.543	0.715	-0.957	1.272
	4.0	-0.314	0.414	-1.167	1.550
	6.0	-0.060	0.079	-1.372	1.822
I a	0.0	8.828	1.000	-38.473	1.000
B b	2.0	8.542	0.968	-33.700	0.876
	4.0	8.241	0.933	-31.224	0.812
	6.0		0.901	-28.503	0.741
I a	0.0	-0.373	1.000	-1.175	1.000
B c′	2.0	-0.251	0.672	-1.507	1.282
	4.0	-0.135	0.362	-1.853	1.576
	6.0	-0.024	0.064	-2.194	1.866
I c	0.0	4.800	1.000	-0.072	1.000
B b	2.0	5.50	1.145	-0.116	1.608
	4.0	6.259	1.304	-0.177	2.459
	6.0	6.983	1.455	-0.239	3.321
I c	0.0	0.389	1.000	-0.012	1.000
B a	2.0	0.523	1.345	-0.033	2.713
	4.0	0.687	1.767	-0.052	4.284
	6.0	0.786	2.021	-0.078	6.447
I b	0.0	1.455	1.000	-4.153	1.000
B a	2.0	1.759	1.209	-6.086	1.466
	4.0	2.104	1.446	-5.776	1.391
	6.0	2.238	1.538	-5.830	1.404

Figure captions

Figures 4.20 through 4.31 give the ratio of the Hall mobilities of holes and electrons at a pressure P to their values at atmospheric pressure.
Each curve is labeled by two digits. The first digit gives the direction of the current and the second one the direction of the magnetic field. The axes a,b,c' are numbered 1,2,3 respectively.
Figure 4.20 gives the change of the Hall mobility of holes in the constant relaxation time model. Only two-center integrals are included. Three directions are given.

Figure 4.21 gives the other three directions of the previous case.

Figure 4.22 gives the change of the Hall mobility of electrons in the constant relaxation time model with pressure. Only two-center integrals are included.

Figures 4.23 and 4.24 give the change of the Hall mobility of holes in the constant mean free path model with pressure. Only two-center integrals are included.

Figure 4.25 gives the change of the Hall mobility of electrons in the constant mean free path model with pressure. Only two-center integrals are included.

Figures 4.26 and 4.27 give the change of the Hall mobilities of holes in the constant relaxation time model with pressure. Two and three-center integrals are included.

Figure 4.28 gives the change of the Hall mobilities of electrons in the constant relaxation time model with pressure. Two and three-center integrals are included.

The Hall mobilities in the constant mean free path model are given in figures 4.29and 4.30 for holes and in figure 4.31 for electrons. Two and three-center integrals are included.

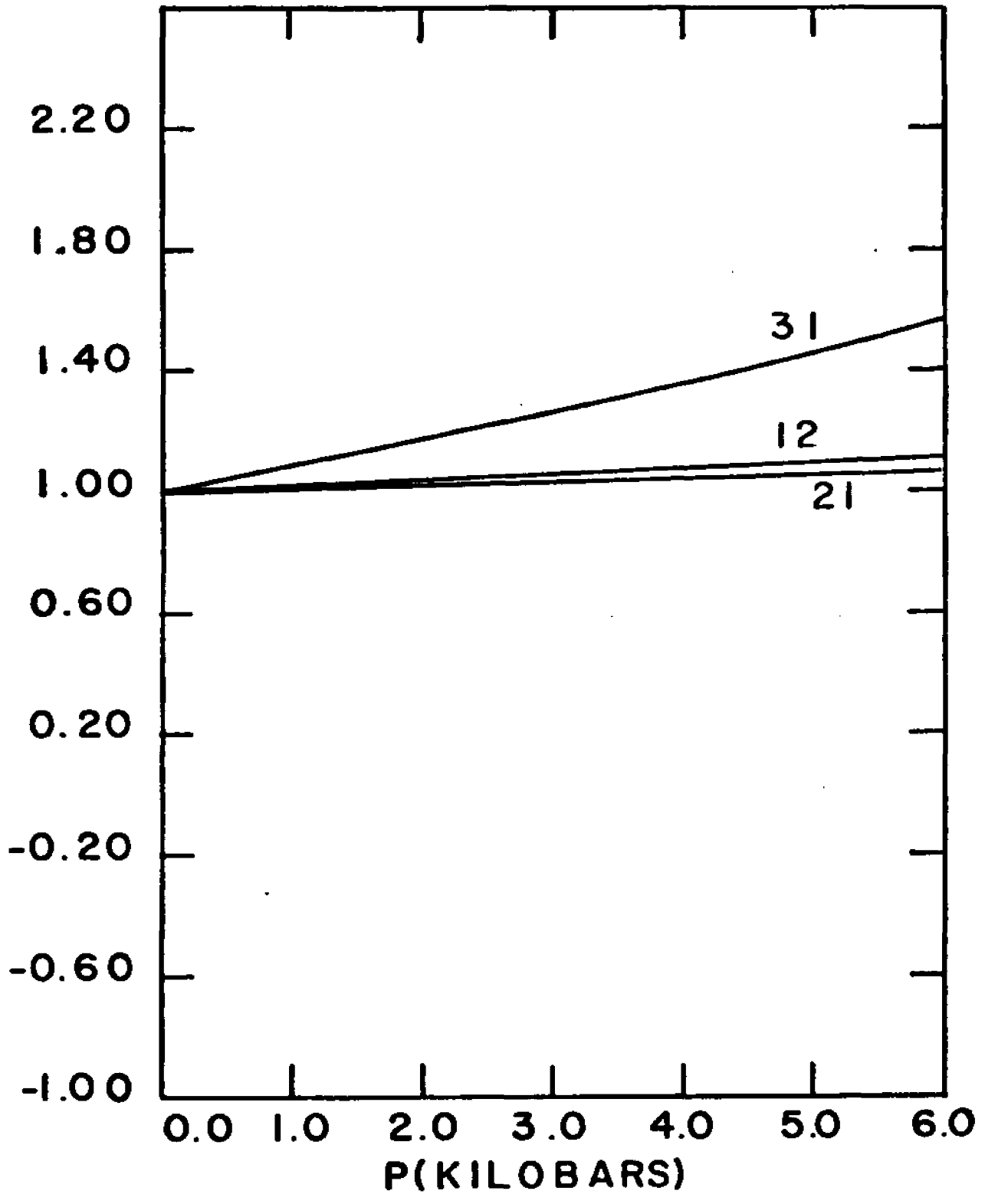
2.20
1.80
1.40
1.00
0.60
0.20
-0.20
-0.60
-1.00
31
12
21
0.0
1.0
2.0
3.0
4.0
5.0
6.0
P(KILOBARS)

FIG. 4.20

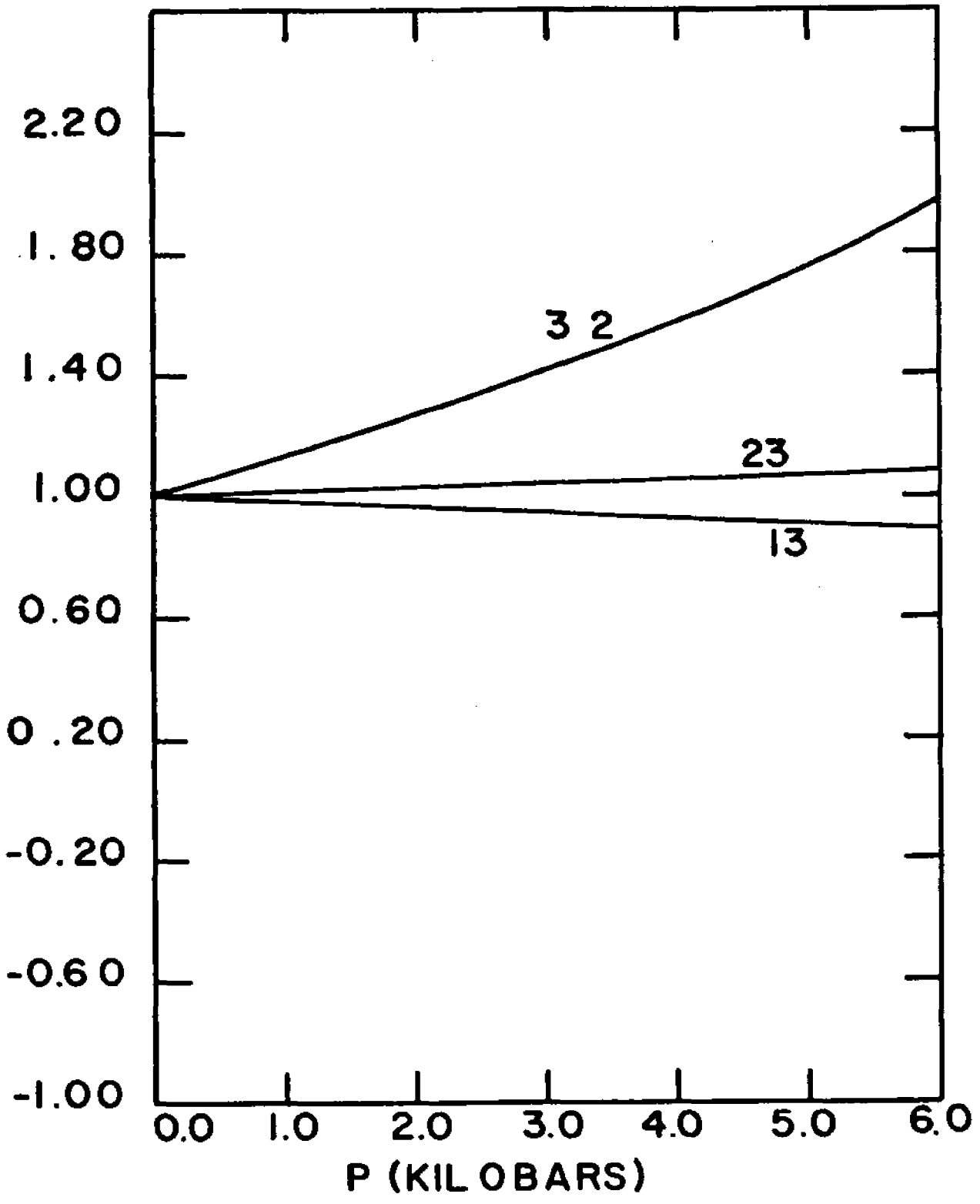
2.20
1.80
1.40
1.00
0.60
0.20
-0.20
-0.60
-1.00
0.0
1.0
2.0
3.0
4.0
5.0
6.0
P (KILOBARS)
32
23
13

FIG. 4.21

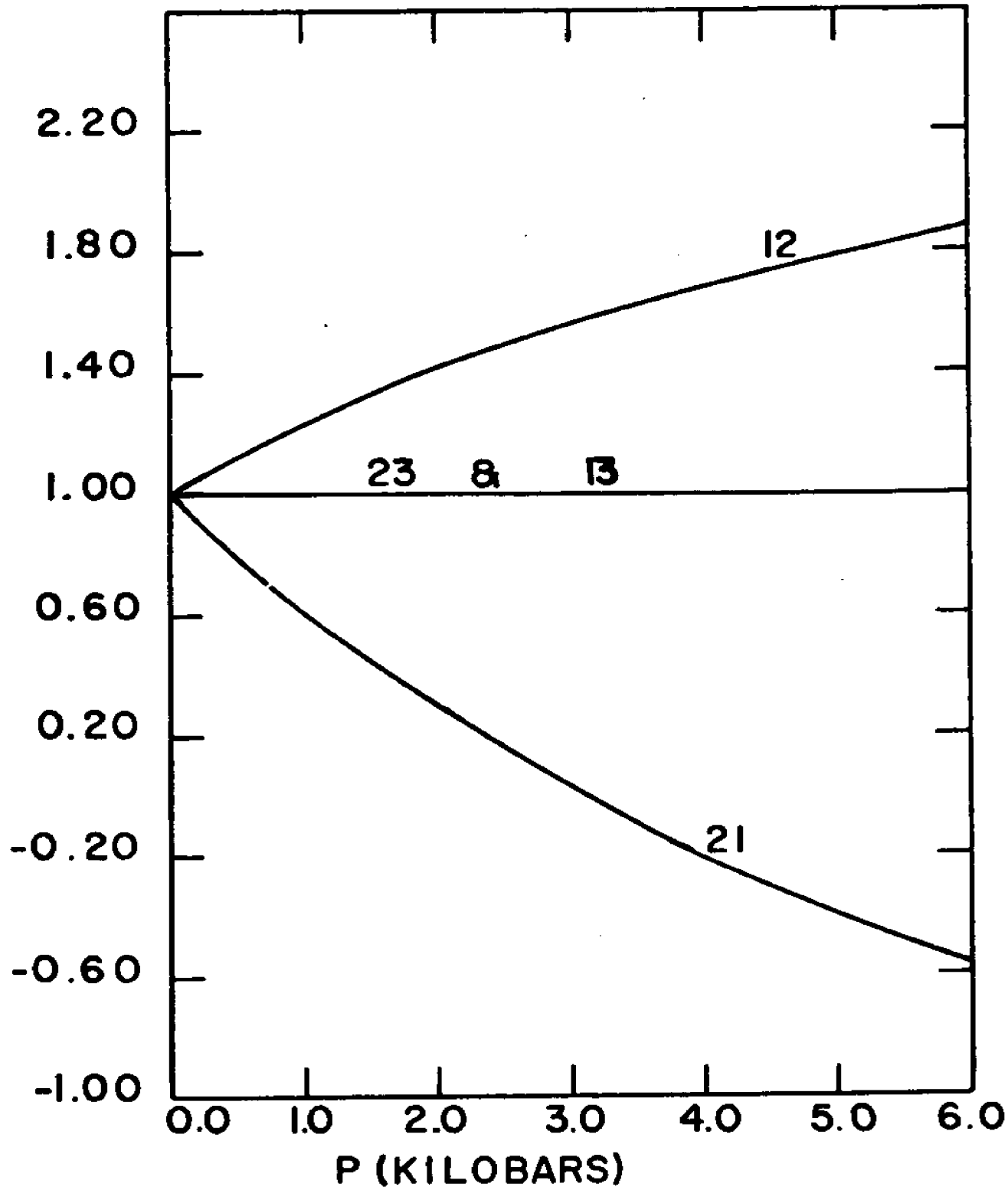
2.20
1.80
1.40
1.00
0.60
0.20
-0.20
-0.60
-1.00
12
23 & 13
21
0.0
1.0
2.0
3.0
4.0
5.0
6.0
P (KILOBARS)

FIG. 4.22

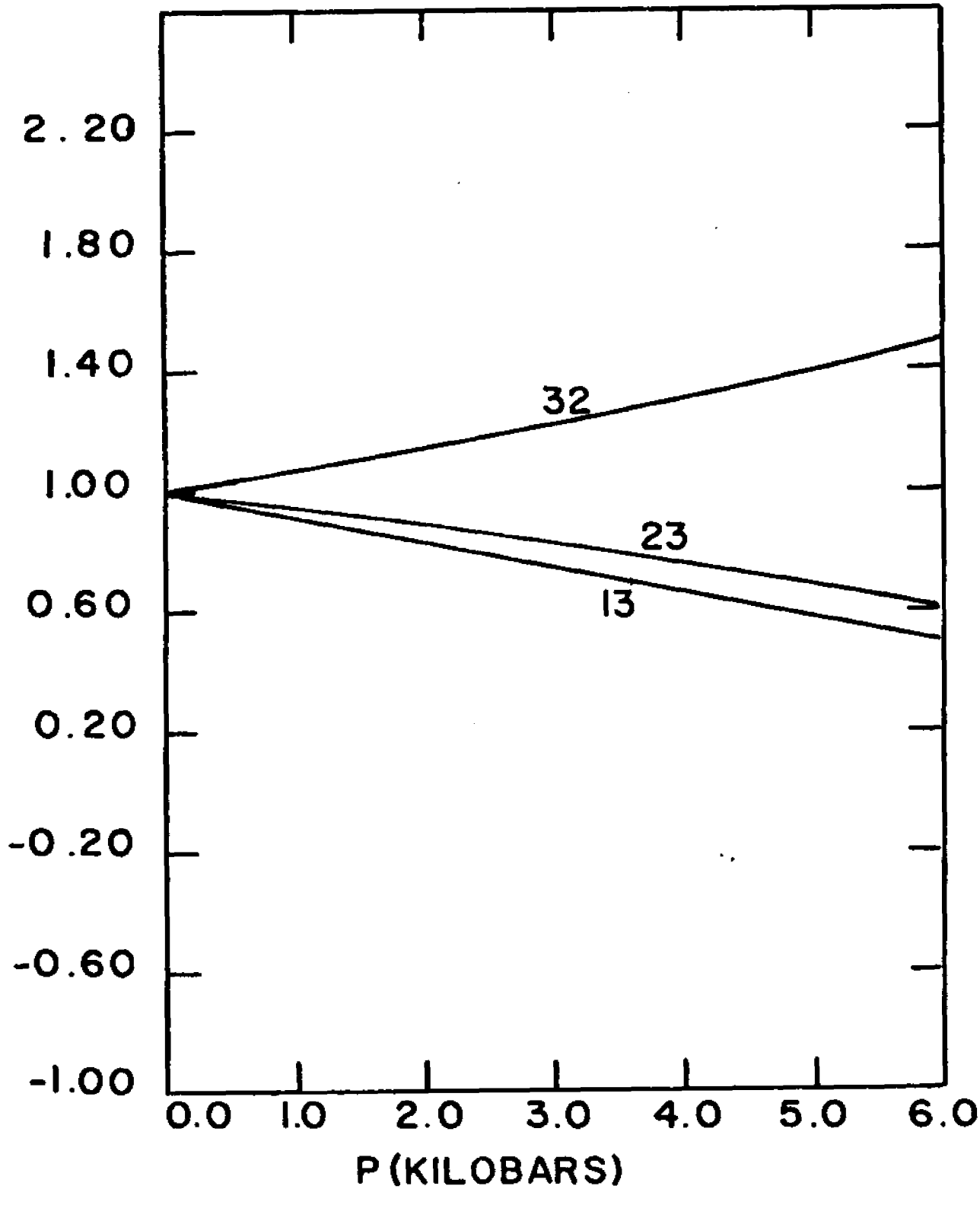
2.20
1.80
1.40
1.00
0.60
0.20
-0.20
-0.60
-1.00
32
23
13
0.0
1.0
2.0
3.0
4.0
5.0
6.0
P (KILOBARS)

FIG. 4.23

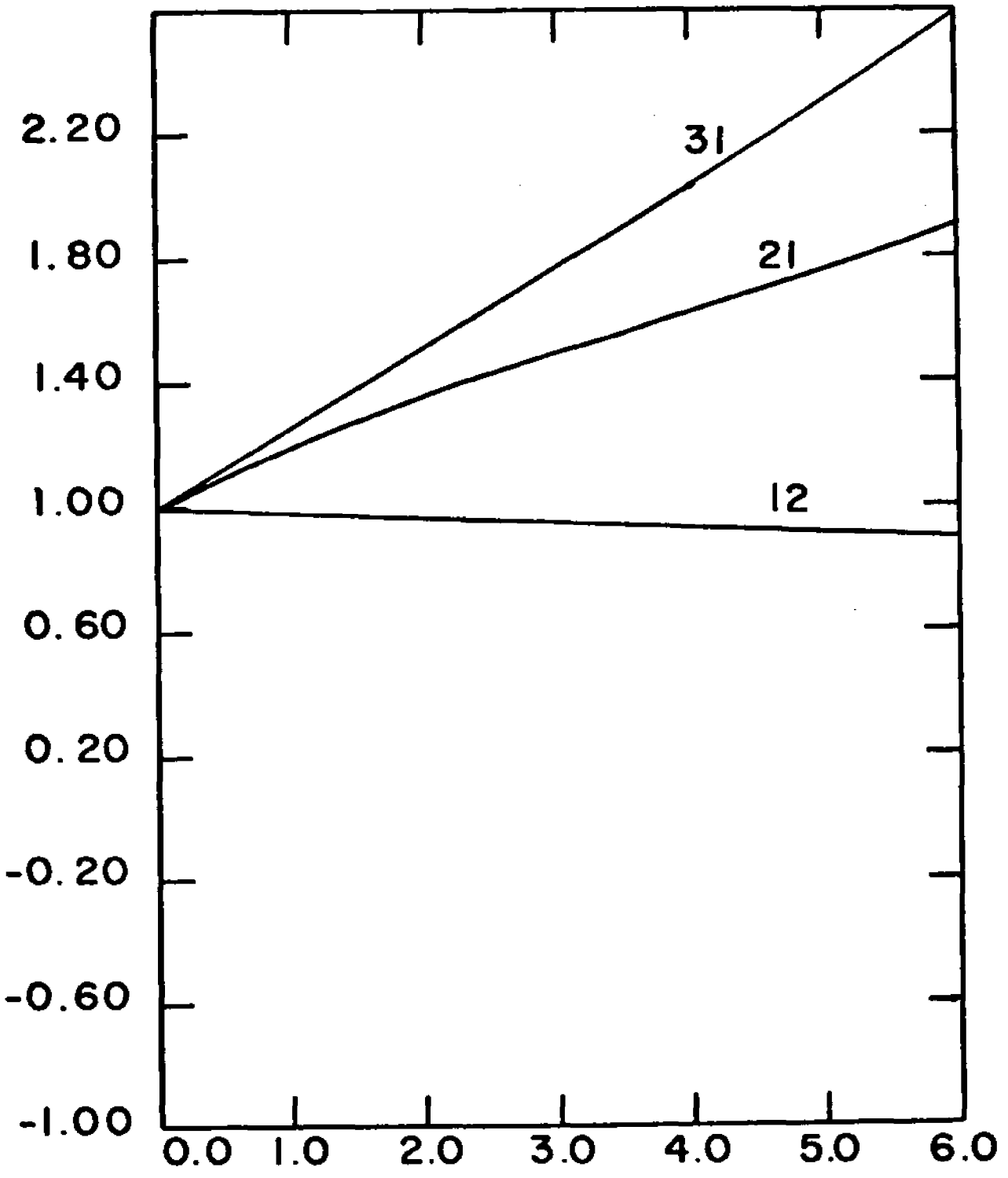
2.20
1.80
1.40
1.00
0.60
0.20
-0.20
-0.60
-1.00
31
21
12
0.0
1.0
2.0
3.0
4.0
5.0
6.0
P(KILOBARS)

FIG. 424

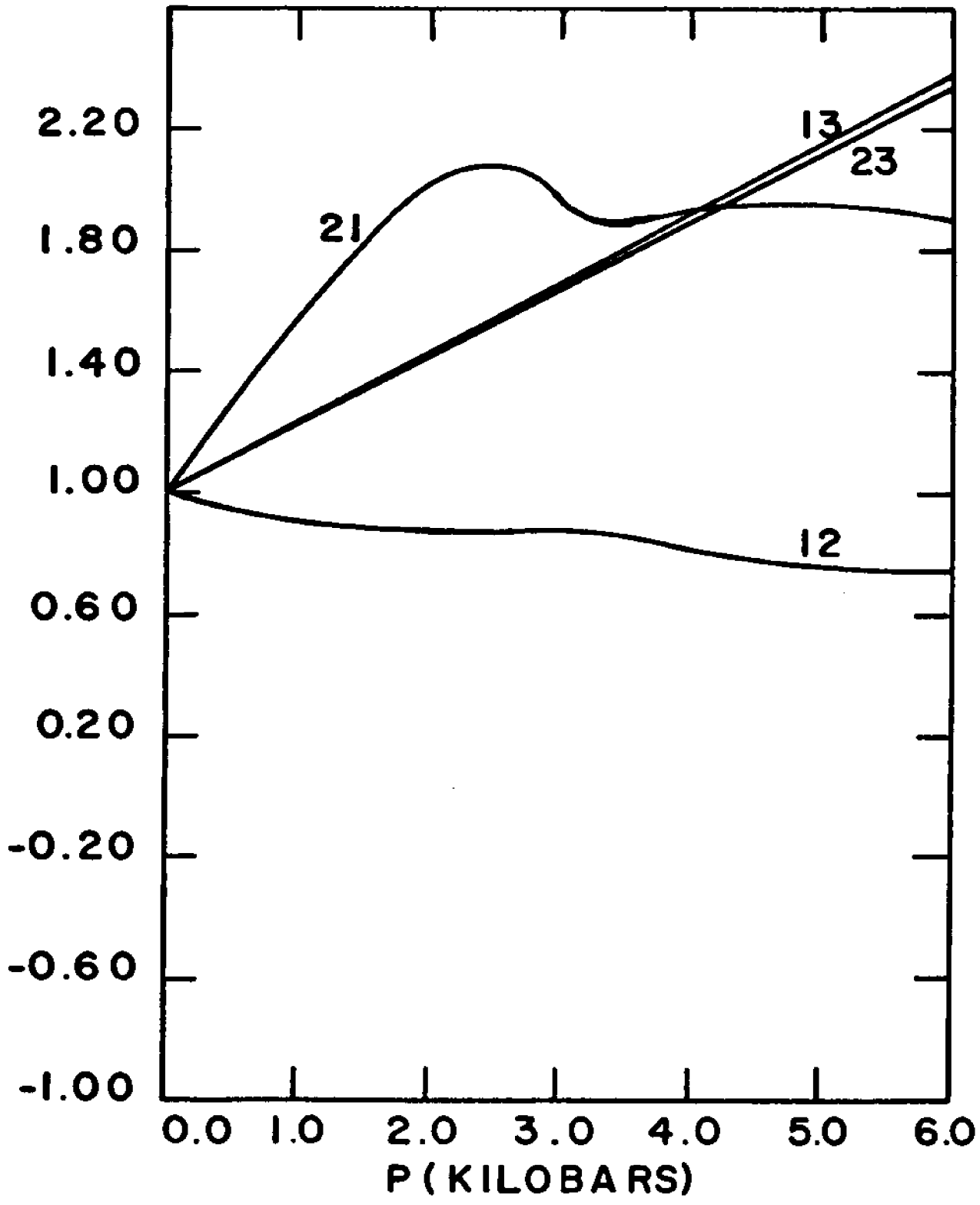
2.20
1.80
1.40
1.00
0.60
0.20
-0.20
-0.60
-1.00
0.0
1.0
2.0
3.0
4.0
5.0
6.0
P(KILOBARS)
13
23
21
12

FIG.4.25

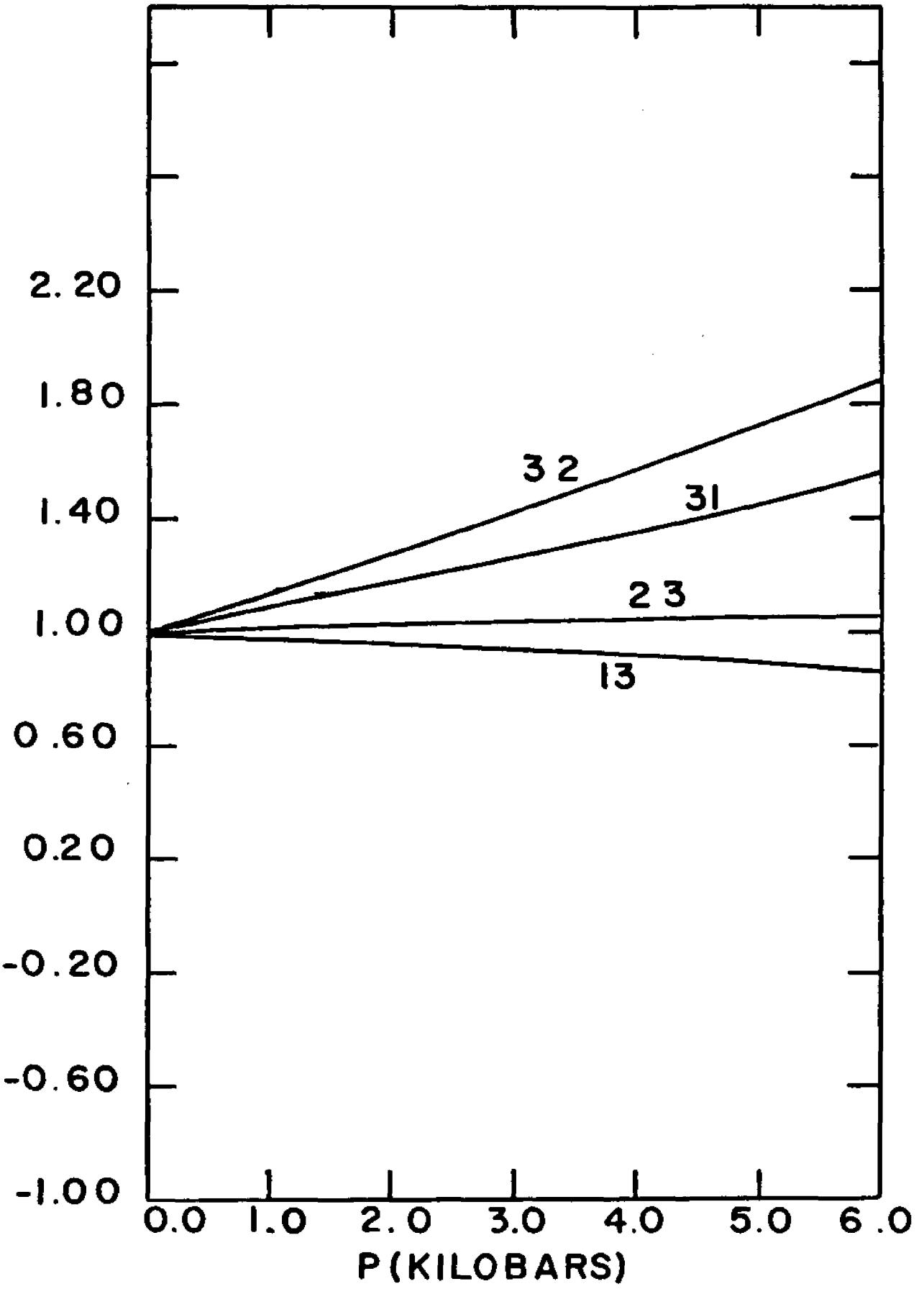
2.20
1.80
1.40
1.00
0.60
0.20
-0.20
-0.60
-1.00
32
31
23
13
0.0
1.0
2.0
3.0
4.0
5.0
6.0
P(KILOBARS)

FIG.4.26

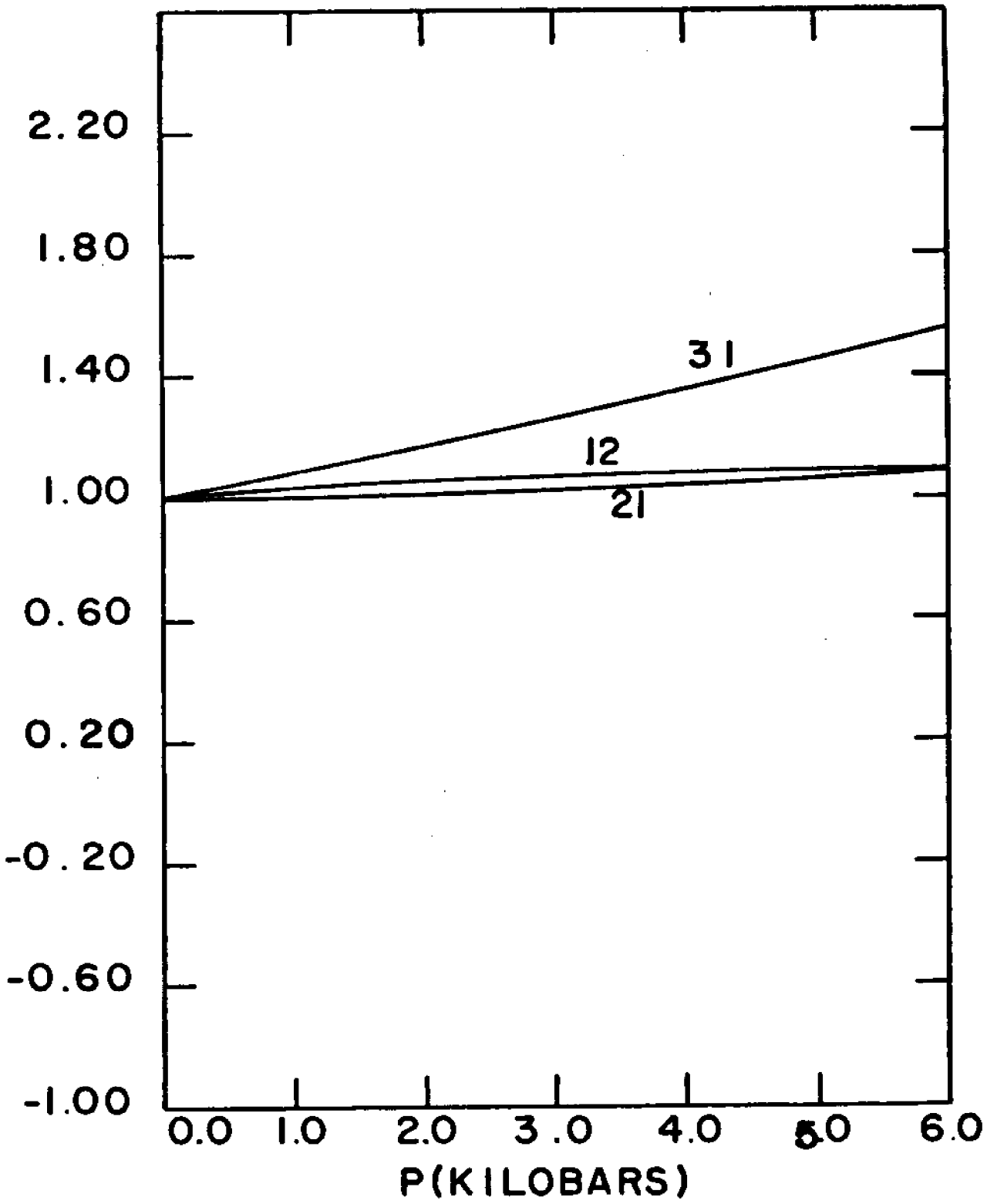
2.20
1.80
1.40
1.00
0.60
0.20
-0.20
-0.60
-1.00
31
12
21
0.0
1.0
2.0
3.0
4.0
5.0
6.0
P(KILOBARS)

FIG.427

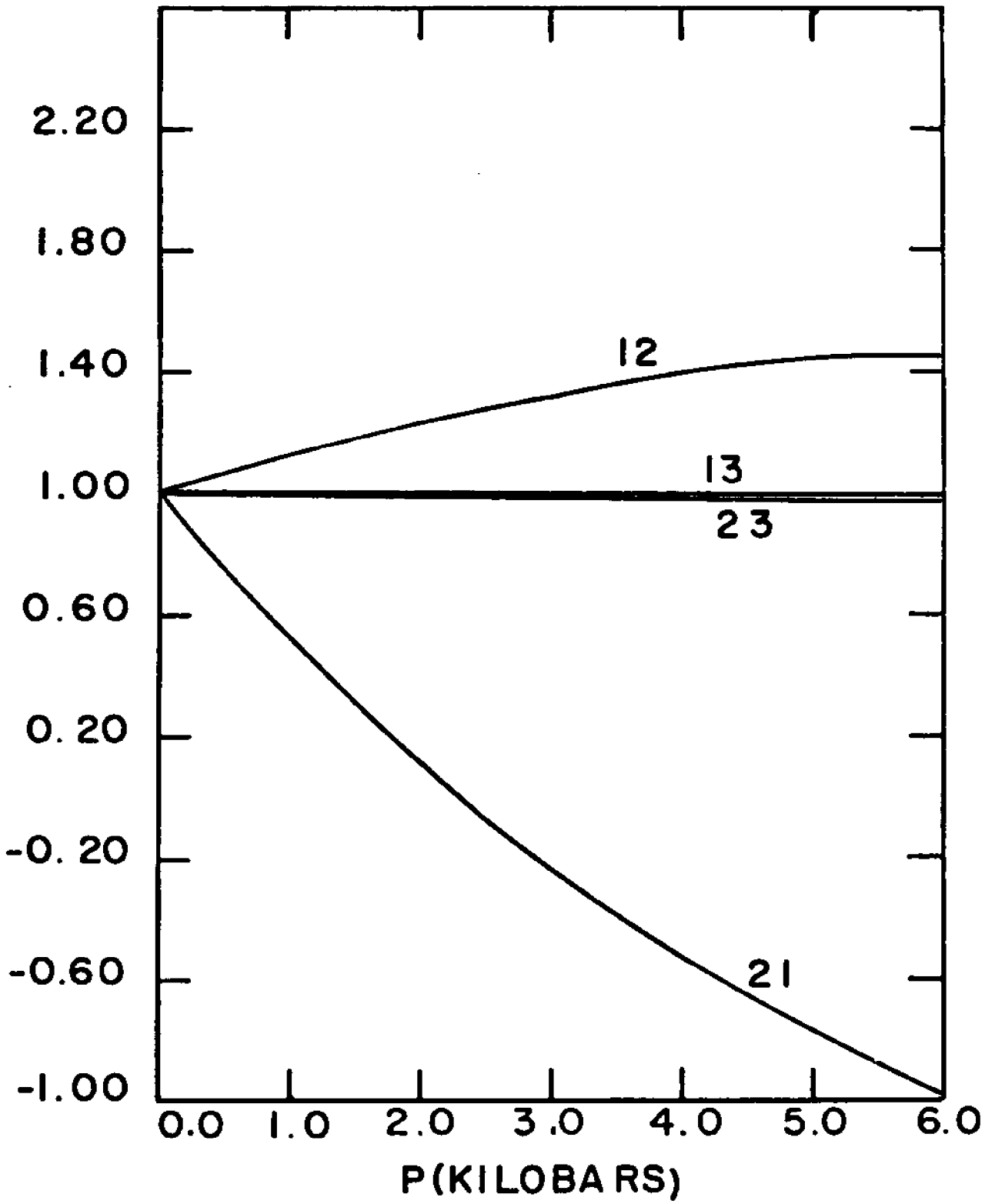
2.20
1.80
1.40
1.00
0.60
0.20
-0.20
-0.60
-1.00
12
13
23
21
0.0
1.0
2.0
3.0
4.0
5.0
6.0
P(KILOBARS)

FIG. 428

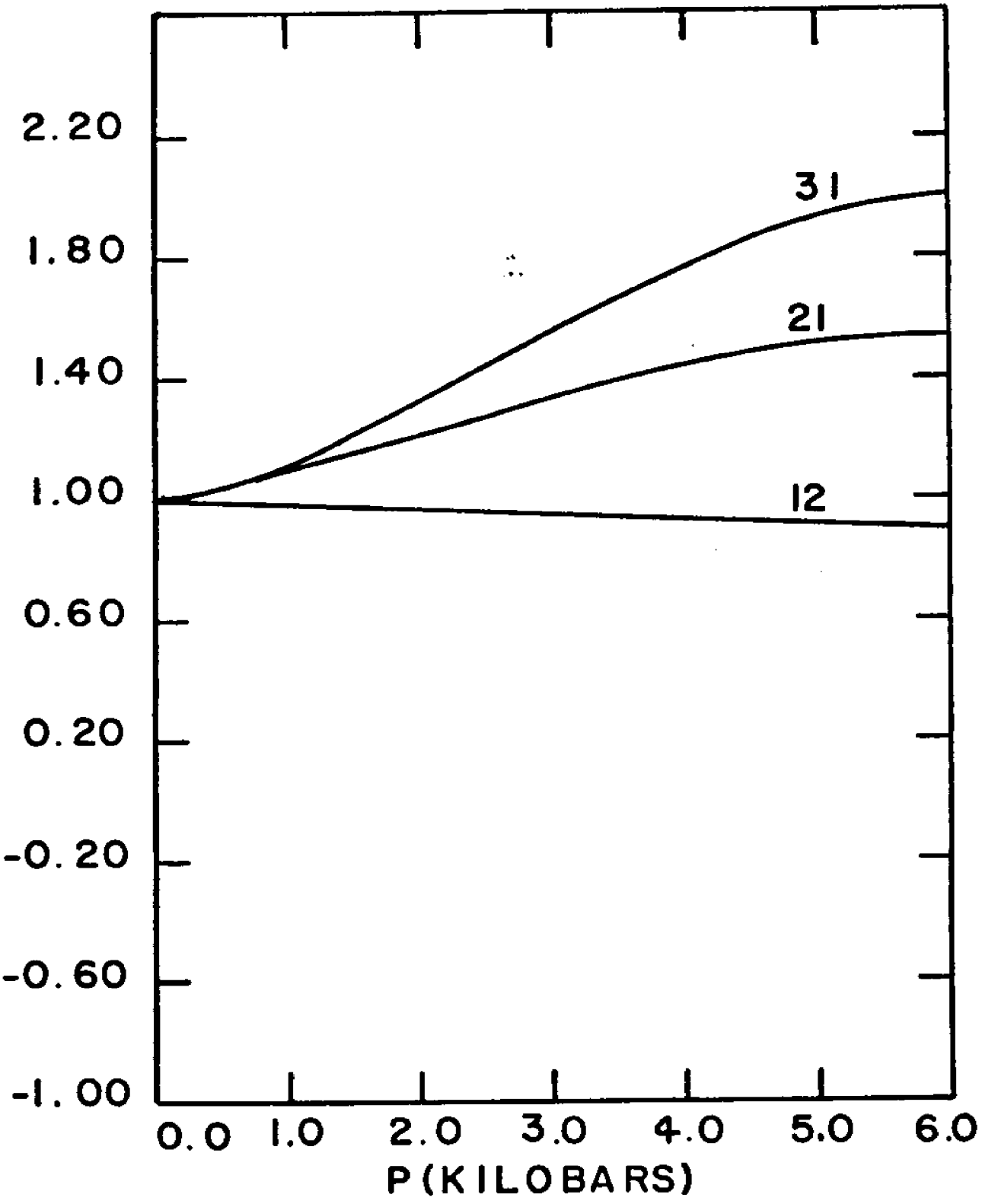
2.20
1.80
1.40
1.00
0.60
0.20
-0.20
-0.60
-1.00
31
21
12
0.0
1.0
2.0
3.0
4.0
5.0
6.0
P(KILOBARS)

FIG. 4.29

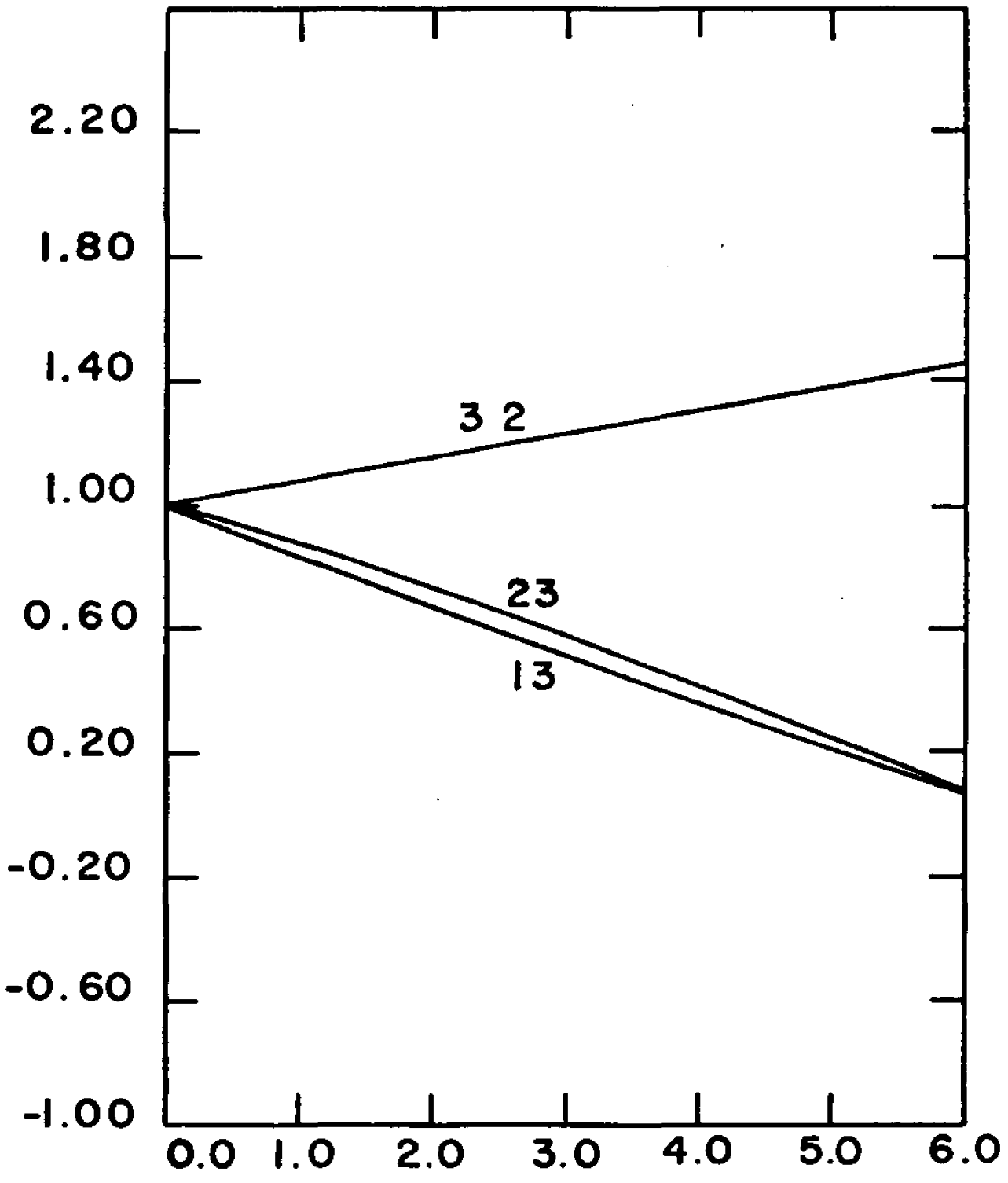
2.20
1.80
1.40
1.00
0.60
0.20
-0.20
-0.60
-1.00
3 2
23
13
0.0
1.0
2.0
3.0
4.0
5.0
6.0
P(KILOBARS)

FIG. 4.30

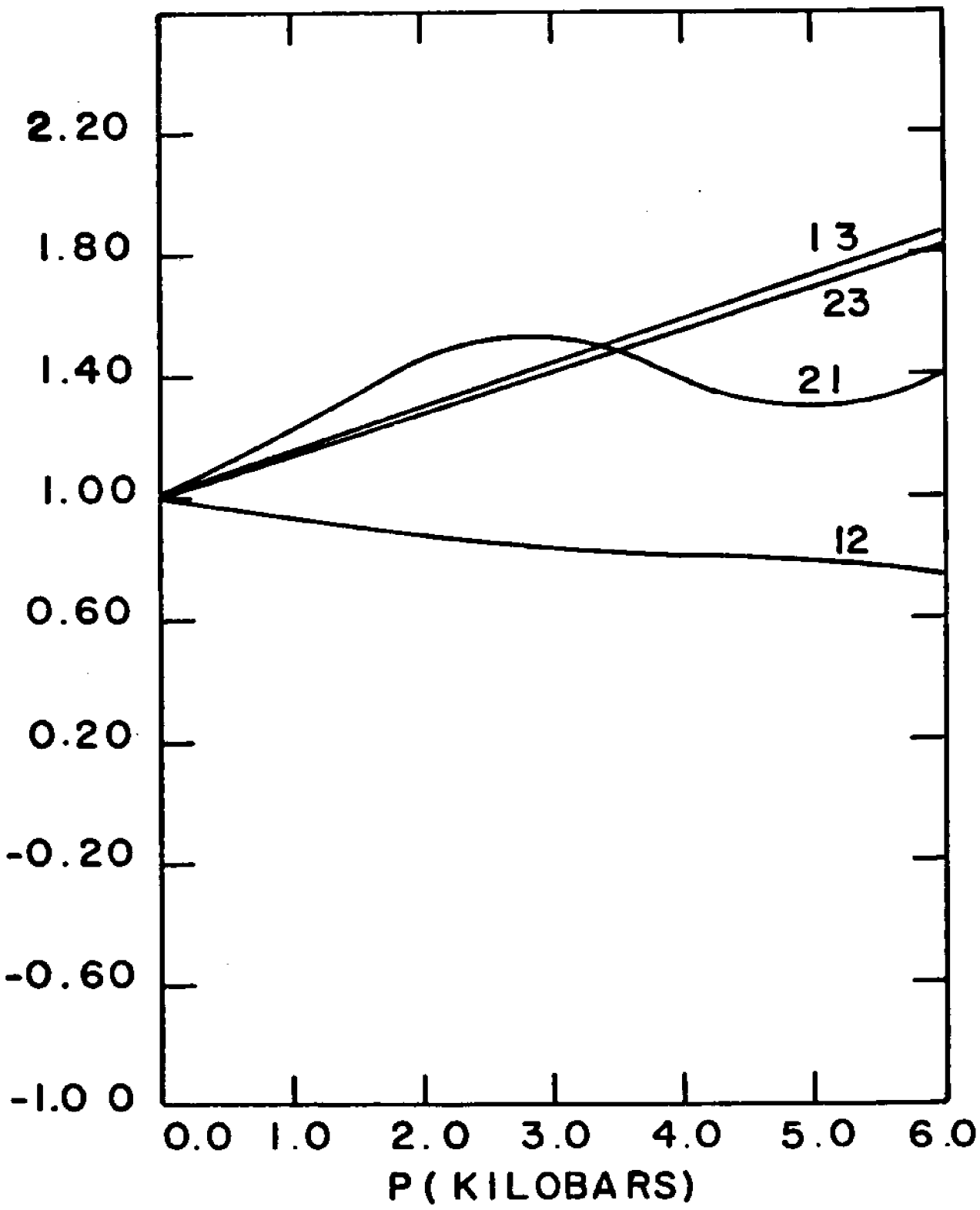
2.20
1.80
1.40
1.00
0.60
0.20
-0.20
-0.60
-1.0 0
0.0
1.0
2.0
3.0
4.0
5.0
6.0
P (KILOBARS)
13
23
21
12

FIG . 4.31

References - Chapter IV

1. O.H.LeBlanc Jr.,J. Chem.Phys. 35 ,1275 (1961).

2. E.Hückel , Z. Physik 76 ,628 (1932).

3. J.C.Slater ,Phys. Rev. 36 ,57 (1930).

4. J.I.Katz , S.A.Rice,S.Choi , and J.Jortner,J.Chem. Phys.39, 1683 (1963).

5. M.Goeppert-Mayer and Sklar,J.chem.Phys.6,645(1938).

6. G.D.Thaxton,R.C.Jarnagin and M.Silver,J.Phys.Chem. 66 , 2461 (1962).

7. E.Clementi and C.C.J.Roothaan,Phys. Rev. 127,1618(1962).

8. R.Silbey,J.Jortner,S.A.Rice,and M.T.Vala Jr.,J.Chem. Phys.42,733 (1965).

9. R.Silbey,J.Jortner,S.A.Rice,and M.T.Vala Jr.,J.Chem. Phys.43,2925 (1965).

10. R.M.Glaeser and R.S.Berry,J.Chem.Phys.44,3797 (1966).

11. R.J.W.LeFevre and K.M.S.Sundaram,J.Chem.Soc. 1963,4442.

12. Chojnaki,Molecular Crystals 3 , 375 (1967),(b)H.Chojnaki Molecular Crystals 5,313 (1969).

13. P.Balk,S.Debruijn,and G.J.Hoijtink,Recueil Trav.Chim. pays bas 76,860 (1957).

14.(a) J.A.Pople,Proc.Phys.soc. (London)A68,81,(1955);
(b) C.A.Coulson and G.S.Rushbrooke,Proc.Cambridge Phil.36,193 (1940).

15.(a) J.R.Hoyland,Thesis No. 61-6790,University Microfilm ,Inc.,Ann Arbor,Michigan,1961.
(b) J.R.Hoyland L.Goodman,J.Chem.Phys.36,12 (1962).

16. R.Pariser and R.G.Parr,J.Chem.Phys.21,466 (1953).

17. C.Sinclair,J.M.Robertson,and A.M.Mathieson,Acta Cryst. 3,251 (1950).

References- Chapter IV

18. V.Heine,Group theory in Quantum Mechanics (Pergamon press New York,1960),chap.VI.

19. (a)R.G.Kepler,Phys. Rev. 119,1226 (1960);(b) R.G.Kepler in Organic Semiconductors conference,edited by J.J.Brophy and J.W.Buttrey (The Macmillan Company New York,1962),p1.

20. Takashi Kajiwra,Hiroo Inokuchi and Shigeru Minomura Bull of the Chem.Soc.Of Jap.vol41,No.8,1783(1968).

21. O.H.LeBlanc Jr.,J.Chem.Phys.39,2395(1963).

22. T.Toombs,Ph.D.Thesis,Princeton University (unpublished 1968).

Chapter V

High Pressure System

As mentioned in the Introduction, one of the important objectives of this work was to develop a high pressure gas system with a non-magnetic cell which can be used not only to measure the Hall mobility and its pressure dependence but more generally it can be used to do any electrical measurement at high pressure which requires a magnetic field and/or optical illumination. In this chapter we describe that unique system. Figure(5.1) is a block diagram of the high pressure system which we now describe in detail.

"A" is an argon gas cylinder of research grade. Argon is used as the pressure transmitting medium. Since anthracene crystal has a very high resistivity, any electrical measurement under pressure requires an insulating medium which has a higher resistivity than the sample, to avoid shunting effect, and is known not to react with the organic compounds. Pure argon is a suitable choice.

"D" is a two stage air-operated compressor (American Instruments Co. # 46-14021) This compressor requires a 90 P.S.I. air supply to operate. It raises the pressure from 2000 P.S.I. at the input to 30,000 P.S.I. at the output.

"T" is a T-shaped connector.

"H" is a dial pressure gage which measures pressures up to 5 kilobars.

"E" is a medium pressure 3-way valve (HIP No. 60-13HF2) which stands pressures up to 60,000 P.S.I. One of its two outlets is used as a vent while the other one is connected to valve "F".

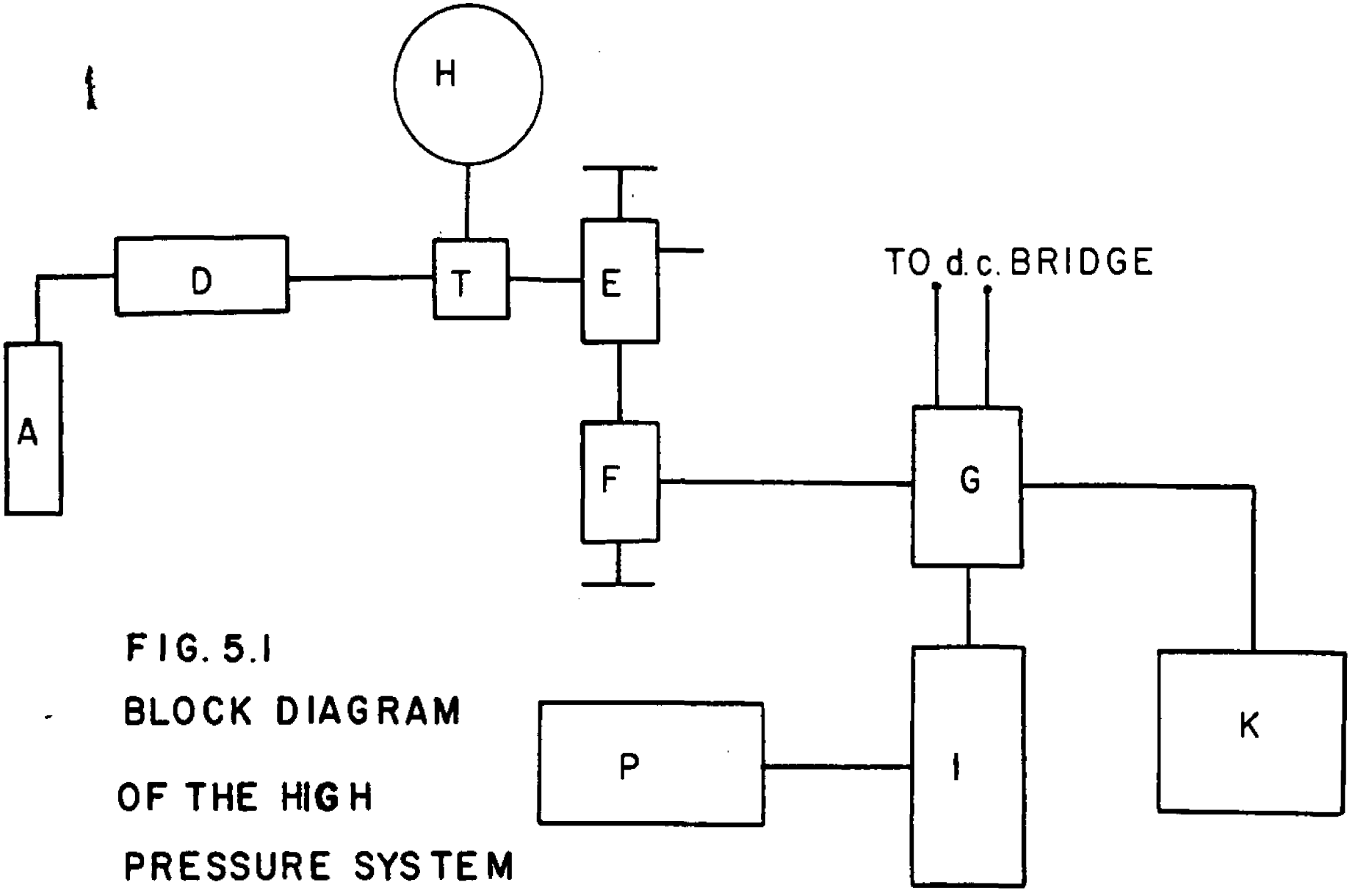

FIG. 5.1
BLOCK DIAGRAM
OF THE HIGH
PRESSURE SYSTEM

"F" is a two-way high pressure valve which can take pressures up to 150, 000 P.S.I. (HIP # 150-11 x F6)

"G" is a high pressure chamber which contains a high pressure gage. This gage is of the form of a coil of manganin wire whose resistance changes linearly with hydrostatic pressure in the pressure range of interest here.

"I" is a pressure intensifier (Harwood Engineering Company, Inc., # A 2.5 J Laboratory type intensifier for gas service up to 200,000 P.S.I.). This is simply a moving piston with oil on the large area end of the piston and the argon gas on the small area end. The ratio of the areas is 15 to 1 resulting in a pressure intensifying by a factor of 15.

"P" is an "Enerpac" oil hand pump which is used to pump up the piston of the intensifier.

"K" is the high pressure cell which contains the sample holder.

In order to understand how this system works, the system can be thought of as consisting of two main sections, a low pressure section and a high pressure one. The low pressure section includes all parts of the system prior to the high pressure valve "F". The pressure in this section never exceeds 30,000 P.S.I. The high pressure section includes the rest of the system. The pressure in this section under working conditions is the high pressure which the sample is subject to. All the tubings before valve "E" are non-magnetic stainless steel tubing of outer diameter of 1/8". The tubing after valve "E" are of 1/16" outer diameter and about .005" inner diameter. The oil tubing from the hand pump to the intensifier has an outer diameter of 1/4". These had to be larger to allow the flow of the viscous hydraulic oil used. To operate the system, the vent is closed, valve "F" is opened and the air compressor is

used to pump the entire system up to 30,000 P.S.I. Valve "F" is then closed and the hand pump "P" is used to intensify the pressure in the high pressure section up to the required working pressure.

Although this whole system was completely assembled during this investigation, two of its major parts, namely, the pressure gage chamber and the pressure cell were manufactured in the local shop. Therefore, we devote the next few pages to discussing the important features of these two parts.

Pressure gage chamber

Figures(5.2) and (5.3) are schematic drawings of the pressure gage chamber. The material used is fully maraged vascomax steel (300 c.v.m.). As shown in figure (5.2) the chamber has three gas outlets. One of them is an inlet coming from the low pressure side, the second one is connected to the intensifier and the third one is connected to the main pressure cell. The upper half of the chamber is designed to allow an electrical lead which is connected to the manganin coil to be available outside the chamber. The other terminal of the coil is connected tothe body of the chamber as a common terminal. The main difficulty in manufacturing this chamber was the critical alignment of the center lines of the outlets.

As far as sealing is concerned, the major difficulty was to pressure seal the top side. There are two surfaces to be sealed there. The surface between the sleeve and the body of the chamber; this was sealed by means of a teflon ring which flows upon applying the pressure to improve the seal. The other surface is the inside surface of the mushroom. This was sealed by means of a metallic cone with a delrin cone on its conical surface, to electrically insulate it from the body of the chamber, which fitted inside the mushroom. The sealing of this inside surface was done by heating the chamber with a heat

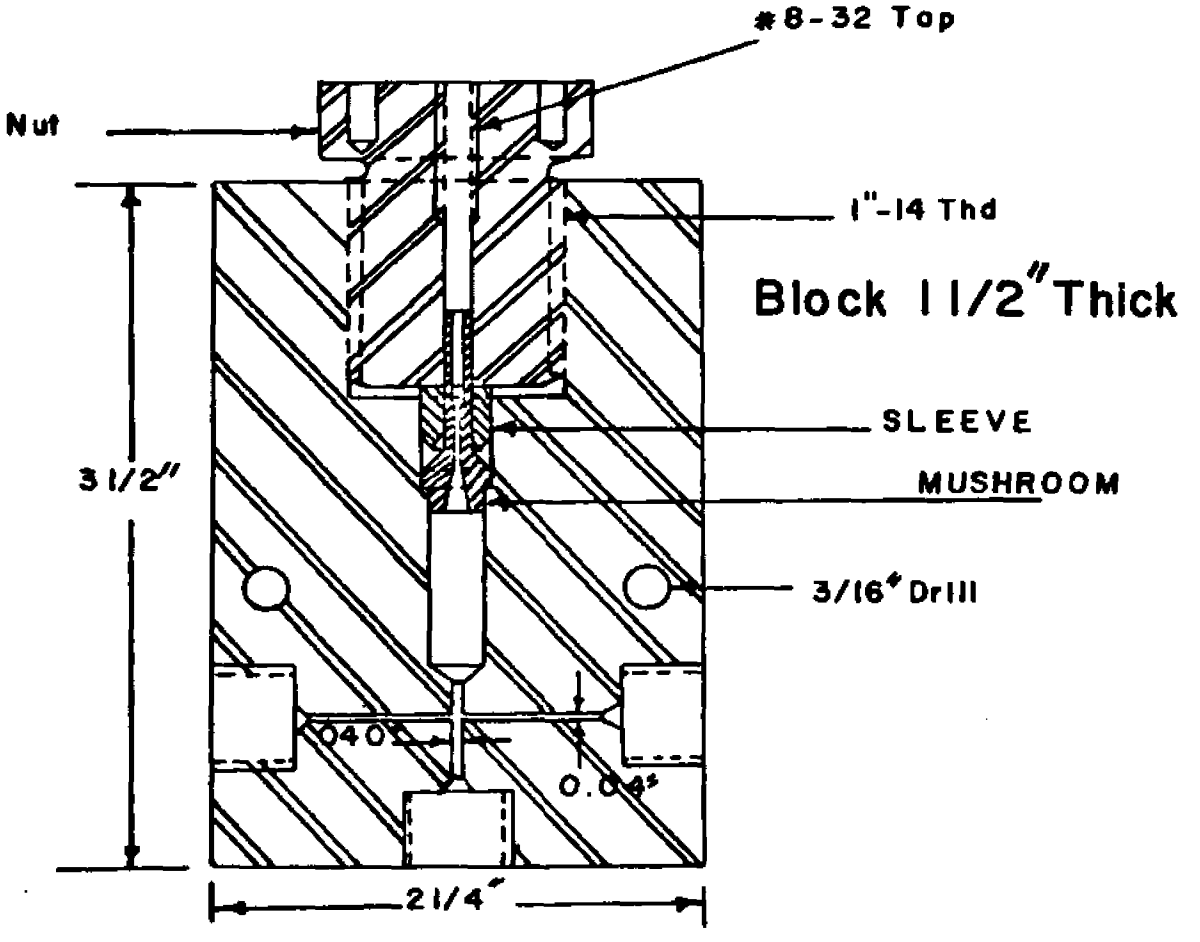

FIG·5.2

PRESSURE GAGE CHAMBER

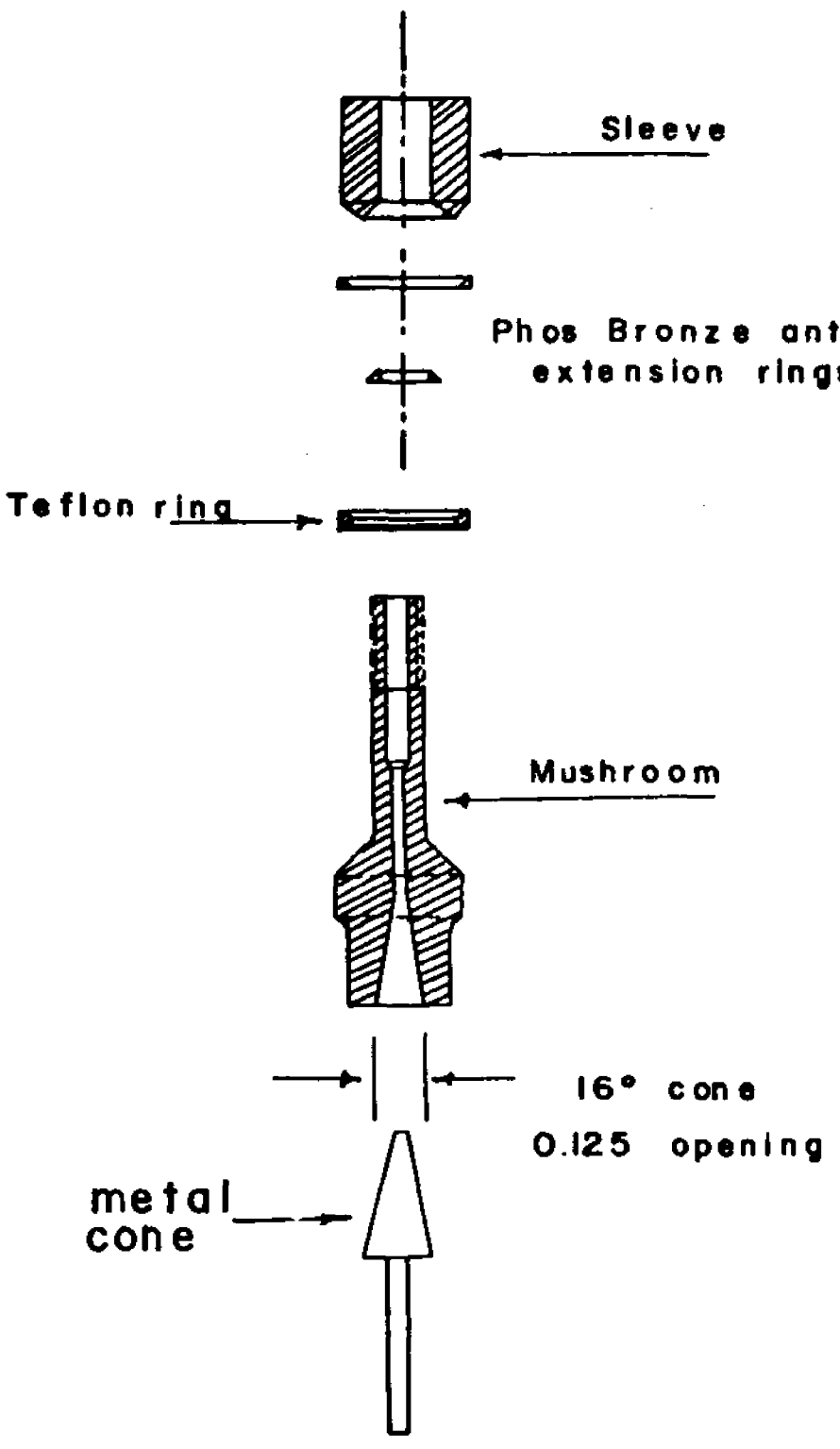

FIG. 5.3

Details of the seal at the top of the gage chamber

gun, while under pressure, to allow the delrin cone to flow and make a tight seal. This metallic cone was used as an electrical terminal of the manganin coil. (This coil was made of #40 wire, it has a total resistance of 170.00 ohms.)

High Pressure Cell

Figure (5.4) is a schematic drawing of the cell. Since this cell is designed to do electrical measurements in the presence of a magnetic field, a non-magnetic material had to be used rather than steel which is conventionally used for non-magnetic high pressure measurements. Based on its mechanical properties beryllium copper #25 alloy, was thought to be the best choice. The material was annealed at 600°F for three hours. The final hardness is R.C. 37 and the tensile strength is 176,100 P.S.I. As can be seen in the figure the cell has two optical windows and five electrical leads going from the high pressure inside the cell to the outside. This is done by stacking alternating metallic and insulating (lucalox) rings with the outside surface inside the high pressure while the inside surface is at atmospheric pressure. Each metallic ring has two wires connected to it, one on the outside rim and one on the inside cylindrical surface. The flat surfaces of the metallic rings and the lucalox rings formed the pressure seals. Two cylindrical sapphire windows were used to seal the cell at the two opposite windows. These were pre-loaded by means of a spring in the form of a solid cylindrical shell with an elliptically shaped hole in the side to allow for the sample holder to be placed inside the cell. The main difficulty in sealing the cell was in lapping the sealing surfaces to optical flatness. Since this alloy is not conventionally used in high pressure equipment, no experience was available on the necessary lapping techniques, especially the surfaces to lap against and the lapping compounds. Such an experience had to be developed locally. Lapping compounds gradually decreasing in particle size from 12 to 4

Figure captions

Figure 5.4 shows a schematic diagram of the high pressure cell.

"A" is a beryllium copper nut.

"B" is a push piece made of beryllium copper.

"C" is a seal ring made of beryllium copper.

"D" is a beryllium copper stack ring.

"E" is a Lucalox ring.

"F" is a spring in the shape of a cylindrical shell with an elliptical hole in the middle. It is made of beryllium copper.

"G" is a seal ring identical to "C".

"H" is a beryllium copper push piece.

"I" is a beryllium copper nut.

"J" are two sapphire windows.

"K" is a beryllium copper window seat.

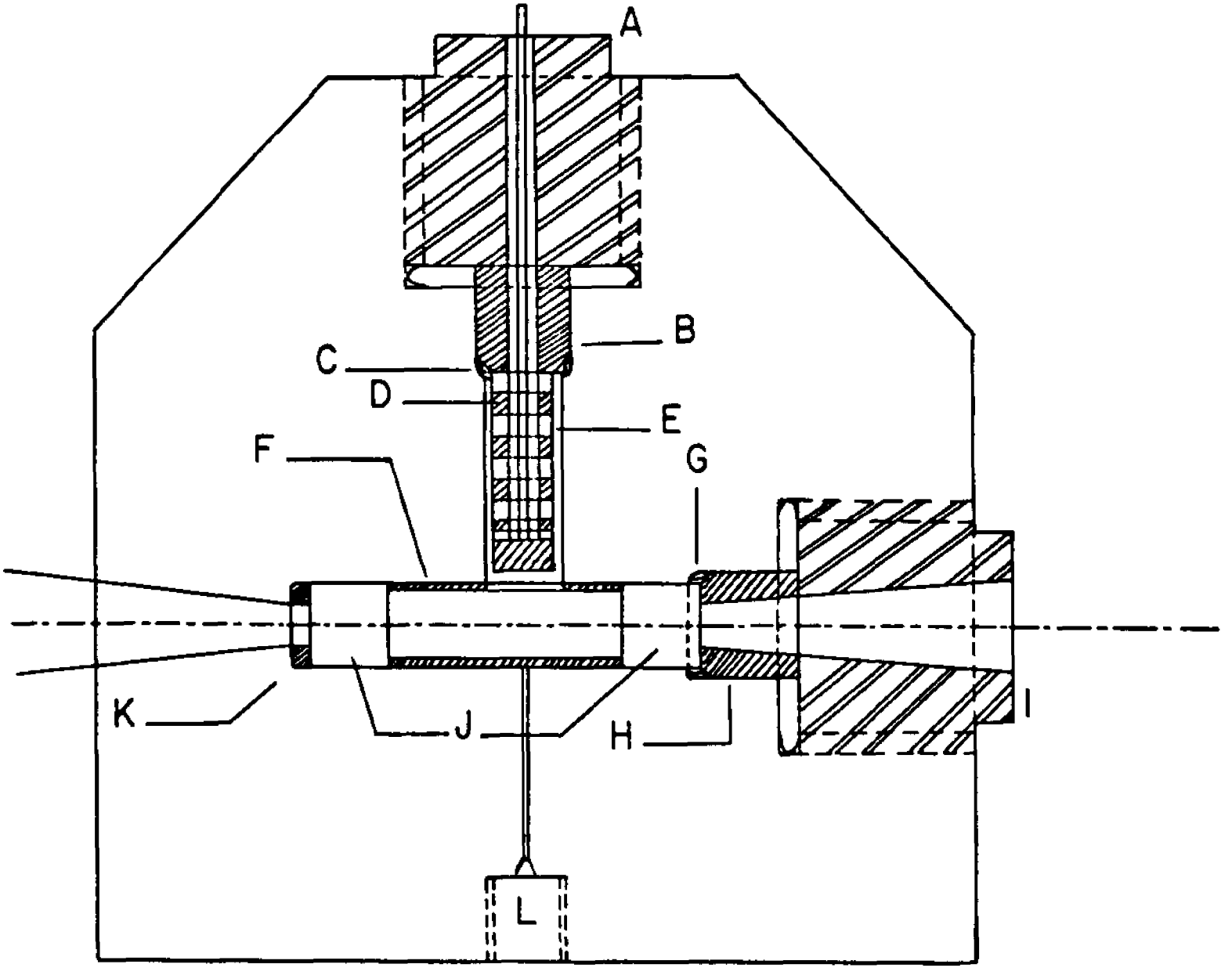

FIG.5.4
HIGH PRESSURE CELL

microns were used in a multistage lapping procedure. Finally, fine aluminum oxide powder of 2-3 microns in particle size was used with liquid soap for final polishing. In spite of a very careful lapping procedure it was necessary to use soft gaskets between the sealing surfaces. On the two windows different materials were tried as gaskets (e.g. thin aluminum foil, mylar, lead foil, teflon sheets) and thin copper foil 0.004" thick was found most suitable. In the case of the stack rings, the choice was even harder since no pre-loading exists there. The material which proved to work best was lead foil .002" thick. This was rolled down from 0.008" thick foil.

All parts of the high pressure section of the system were tested up to 8 kilobars except for the cell, which was tested up to 3.5 kilobars only.

Sample Holder

Figure (5.5) shows a schemetic drawing of the sample holder. This is a miniaturized holder which fits inside the cylindrical spring inside the bore of the cell. The holder is supported to the end piece of the stack as shown in Figures (5.6) and (5.7). The holder consists of a delrin base with a small copper base in the middle used as an electrode. The delrin was chosen because of its high resisitivity, its high resistance to organic solvents and finally, since it is rather hard, it does not deform with repeated use. The upper part of the holder is a disc of quartz, to allow U.V. light to reach the surface of the cell, coated with a thin transparent layer of tin oxide which provides the front electrode. Three other teflon coated wires go through the delrin base to provide the other three leads. In this investigation they were used for the two Hall probes and the guard ring. The wires coming out of the cell go through a metallic pipe, which acts as an electrostatic shield. This pipe ends with an aluminum box where the wires are connected to electrical posts mounted

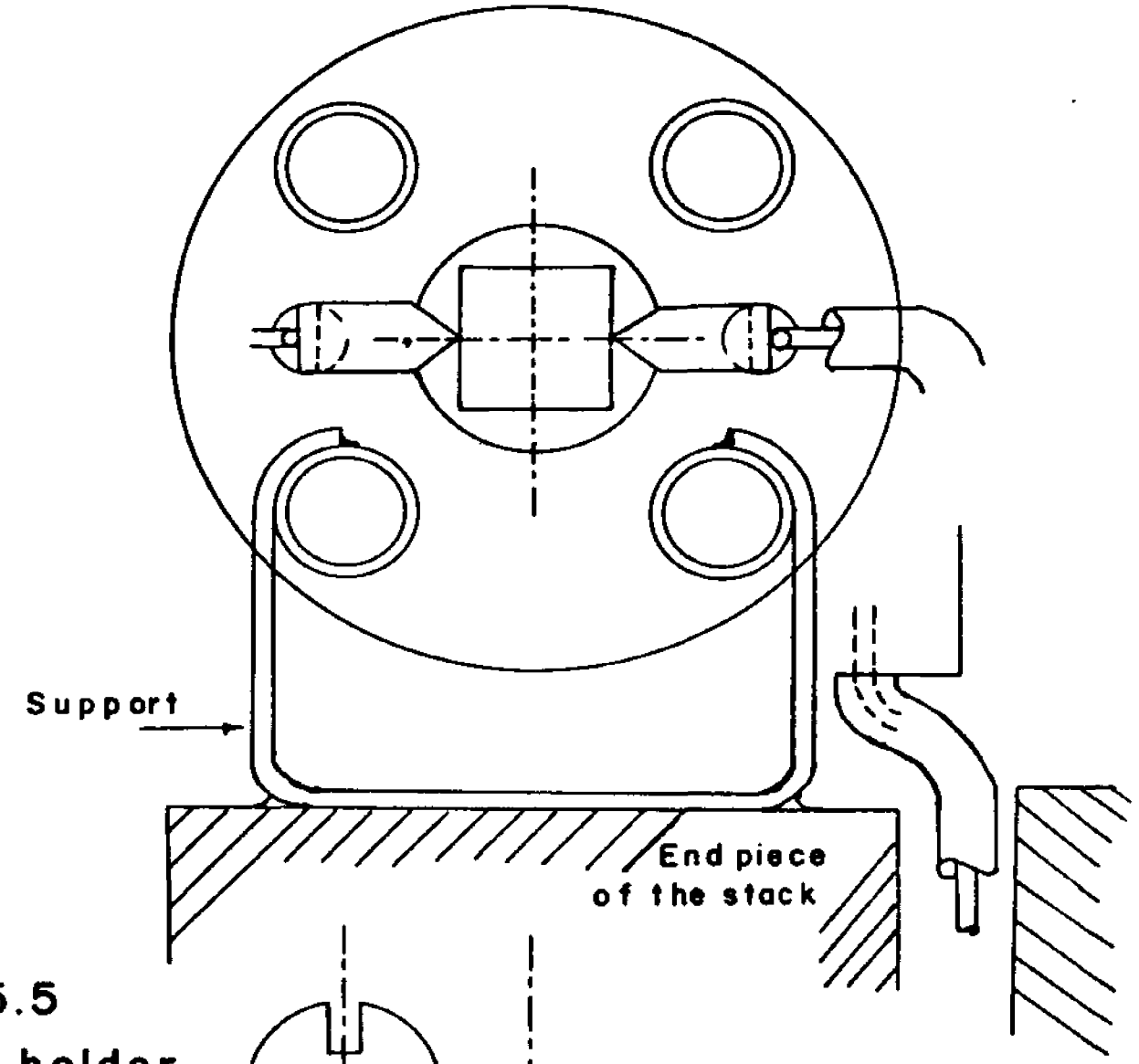

FIG.5.5
Sample holder

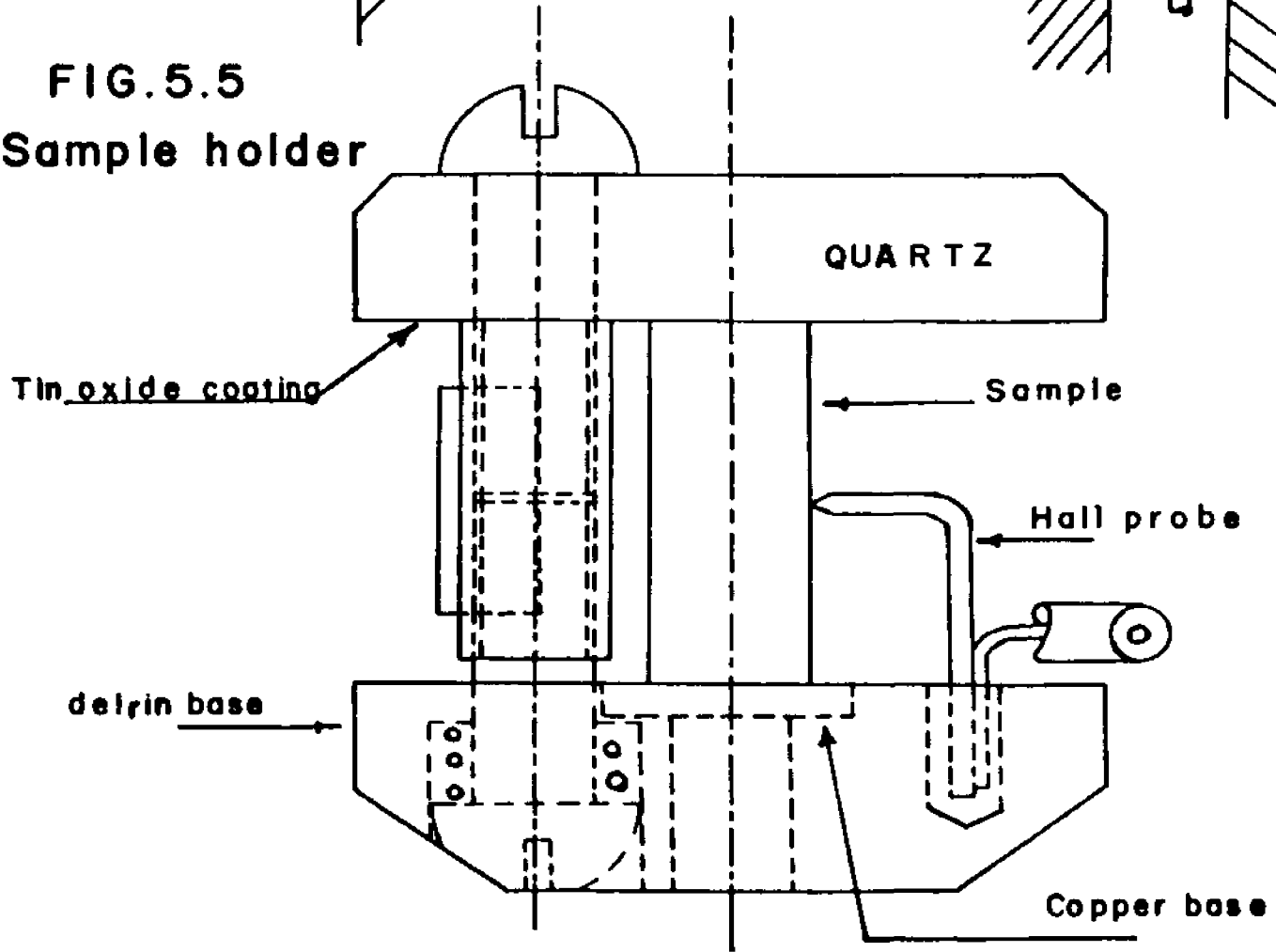

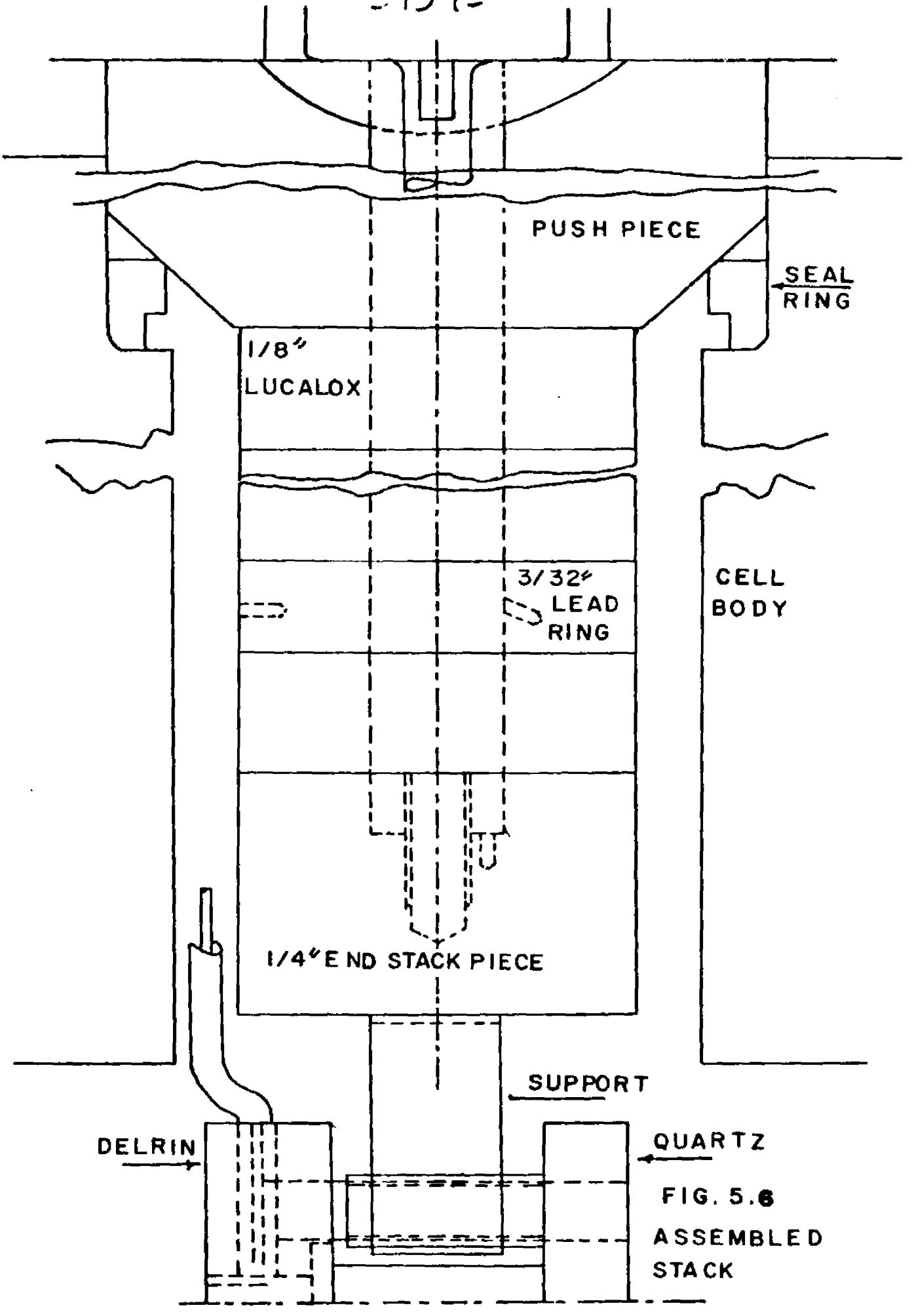

FIG. 5.6
ASSEMBLED STACK

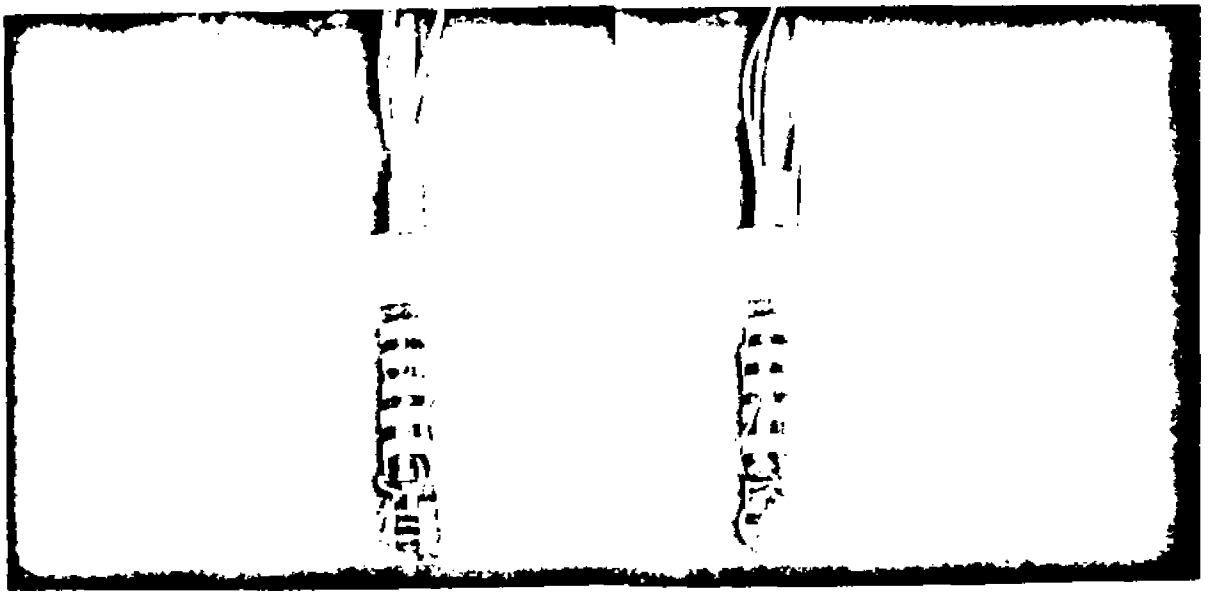

FIG. 5.7

A PHOTOGRAPH OF THE
STACK AND SAMPLE HOLDER

on one side of the box. Also two metallic strips are bolted to the cell. They are used to support the cell which hangs between the pole faces of the magnet.

It should be mentioned that this pressure system is of great versatility. It can be used for any high pressure measurement which requires the presence of a magnetic field, optical illumination, as well as the availability of as many as five electrical wires other than the ground terminal. No such system has been developed before. In the rest of this chapter we discuss how this system was used in a trial to measure photo-Hall mobility and its pressure dependence and the difficulties which were encountered in this kind of measurement.

Sample

The samples used were in the shape of a rectangular parallelopiped which were prepared as explained in Chapter III. The dimensions of the samples were 4x3x2 mm. One end of the sample was coated with silver paint to ensure uniform contact with the copper electrode in the base of the sample holder. A silver-painted guard ring was drawn very near the other end. The purpose of this ring is to help by-pass and suppress the surface currents. Two-fine point probes were silver painted in the centers of two opposite sides. These were used as Hall probes. Good contacts between the sample and the front and back electrodes were ensured by four springs which were placed between the delrin base and the heads of the four screws connecting the base to the quartz front electrode.

Experimental techniques

The techniques used is based on photo-injection of a single type of charge carriers from one end of the sample to travel through to the other end. This photo-current is about two orders of magnitude larger than the intrinsic current. With this relatively large current the Hall voltage can be measured upon applying a magnetic field.

The photo-injection was done by shining U.V.($\lambda < 4200A$) light on one end of the sample. Anthracene crystal strongly absorbs light in the U.V. range of wavelenghs. Therefore, the light is essentially absorbed at the surface, creating pairs of free charges. By properly biasing the back electrode relative to the front electrode, a single type of charge carriers can be allowed to travel through the sample. In this investigation a 1000 watt xenon lamp was used as the source of ultra-violet light. Infra-red light emitted was filtered out by means of a quartz filter filled with a solution of copper sulphate. A quartz lens was used to focus the light on the sample through the sapphire window of the cell and the tin oxide coated quartz electrode in the front of the sample holder. A mask was used to prevent light from striking the guard ring or the crystal beyond it. The guard ring was kept at the same potential of 70 volts as the front electrode.

Electrical system

The electrical system used to measure the Hall mobility is represented by the block diagram shown in Figure (5.8).

The current through the sample is measured by a vibrating reed electrometer. The voltage of each Hall probe is measured by a separate vibrating reed electrometer. A bucking potentiometer was used to cancel any initial voltage that the probe may have, resulting from a geometrical offset of its position from the point of zero voltage. The use of very high input impedence electrometers to measure the Hall probe potentials is essential in the case of molecular crystals like anthracene which have very high resistance, to avoid shunting the sample by the voltmeter. The output of the electrometers are connected to a two-channel chart recorder.

Results

In this investigation the front electrode and the guard

FIG. 5.8 Block diagram for the measurement of the Hall voltage of anthracene

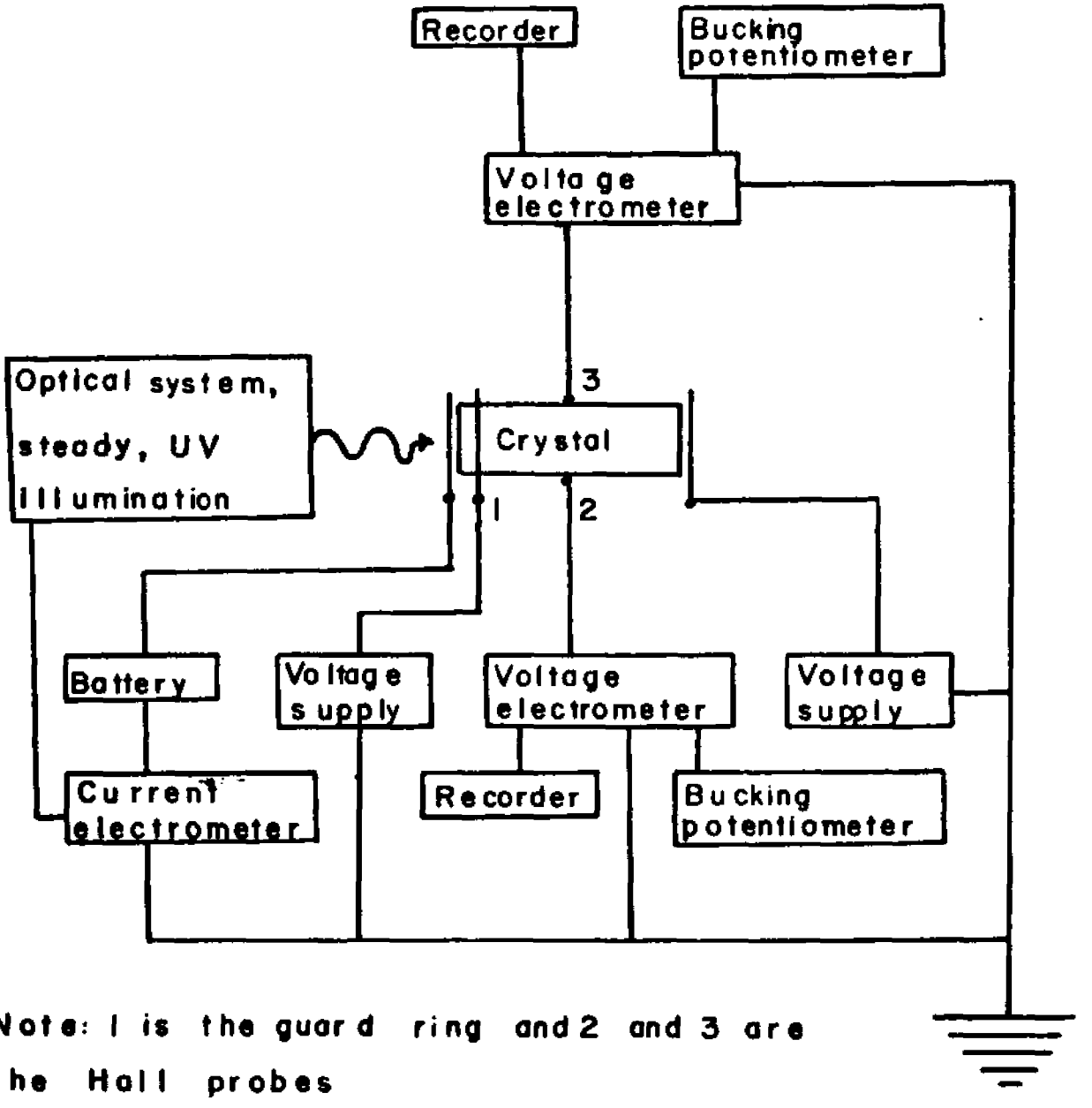

Note: 1 is the guard ring and 2 and 3 are the Hall probes

ring were kept at 70 volts (for holes) and the back electrode was given a voltage, ranging from -40 to -140 volts, adjusted to minimize the potential of the Hall probe with the lower voltage. Upon turning the lamp on the current through the crystal increased from about 5×10^{-13} amps to about $2\text{-}3 \times 10^{-11}$ amps. The potential distribution inside the sample starts to change since the trap centers are now being filled. That could be seen by a large drift rate of the potential of the Hall probes. After a few hours the drift of the potentials of the Hall probes become very small, an indication of a steady state conduction which results from more or less fixed charge distribution. Upon turning the magnetic field on a large voltage of the same polarity appeared on both Hall probes. This voltage was much larger than the expected Hall voltage. If the magnetic field is turned off the voltages return to their inital value. Upon reversing thedirection of the magnetic field a voltage of the same polarity and of almost equal magnitude again developed at the Hall probe. This is contrary to the expected behavior of the linear Hall voltage, which should reverse its polarity upon reversing the direction of the magnetic field. The experiment was repeated a large number of times on samples of different orientations. Either no deflection at all upon applying the magnetic field, or an even effect of the nature described above was observed. The magnitude of the effect however seems to change randomly from one sample to another. In some individual runs the voltage developed with the field in one direction was slightly different than the voltage developed with the field in the opposite direction. This difference can be considered to be twice the linear Hall voltage, but no definite conclusion could be reached about the magnitude of the Hall voltage, much less its pressure dependence.

Typical values used in these runs were a photo-current of 1×10^{-11} amps, a potential difference across the sample of

of 200 ^{v}, and a magnetic field of about 16 kilogauss. The change of the Hall probe voltage upon applying the magnetic field under these conditions was around 60 m.v. This even effect masks the much smaller Hall voltage expected to be in the range of few millivolts, and makes it virtually impossible to have any quantitative estimate of the latter.

Dresner[1], in his first trial to measure the Hall effect in anthracene, has seen an effect which is even with the magnetic field. This effect in Dresner's measurement was superimposed on the linear Hall voltage. According to Dresner, the even effect was small relative to the Hall voltage which made it possible to extract the latter by reversing the magnetic field. In some runs he mentioned that he had to use numerical integration techniques for the signals for two opposite directions of the magnetic field in order to be able to deduce the Hall voltage. Dresner attributed this effect to the presence of surface defects or local variations in mobility. At that time no data were available to give an alternative explanation for such an effect.

Shortly after Dresner's paper Frankevich et al[2-5] observed that magnetic field causes the photocurrents in anthracene to decrease. They first attributed that to the effect of the magnetic field on charge transfer excitons. Pope et al[6] measured the effect of the magnetic field along different directions in the ab plane on the photo-enhanced current along the c1 direction. They used evaporated gold electrode, which injects holes in the crystal, and light in the singlet absorption band (λ = 360 - 400 nm). The photo-current decreased with pronounced anisotropy. They concluded that since there is no exciton fission, and at the light intensities they used there is no triplet-triplet exciton fusion, the effect is due to interaction between a triplet exciton and a trapped hole. In a later paper Frankevich et al[7] explained the magnetic field effect on anthracene photoconductivity to be due to triplet exciton-trapped hole interaction, they also attributed their earlier results to the same effect. Ern et al[8] have given a direct evidence for the triplet-trapped hole interaction by studying the effect of injecting holes in an anthracene crystal on the triplet lifetime. With this body of data it can be

concluded that trapped holes interact with triplet excitons. The triplet excitons decay and the holes are detrapped. The existance of magnetic field apparently slows down this interaction resulting in less detrapping of holes. The effect of the decrease in the rate of detrapping on the current has been reported as mentioned before. This decrease in the rate of detrapping may also change the potential distribution along the sample. This change in the potential distribution would produce an even effect as that found in our Hall voltage measurement. Since the effect of the transverse magnetic field on the rate of detrapping does not depend on the sense of the field, this could explain the even dependence of this new effect on the magnetic field. Furthermore, the random change in the magnitude of this effect from one sample to another, under identical conditions, may be due to the different trap distributions in the samples. It also seems that the long exposure time to light, such an exposure is necessary to reach the steady state, damages the crystal. The crystals show brownish discoloration which may be an indication of some molecular bonding, defect production or oxidation. Therefore we conclude that the method used for carrier injection is not appropriate for these crystals. If this new effect reported here is due to the effect of the magnetic field on the rate of detrapping, as we think it is, a new injection technique ought to be tried which would not produce as many excitons, such a technique may or may not be possible.

References - Chapter V

1. J. Dresner,Phys. Rev. vol 143,558 (1966).
2. Frankevich E.L. and Balabanov E.I.,Zh. ETF Pis. Red. 1,33(1965) (JETP Lett.)1,169 (1965).
3. Frankevich E.L. and Sokolik I.A.,Zh. eksp. teor. Fiz. 52,1189(1967). (Sov.Phys. JETP 52,790(1967)).
4. Frankevich E.L. and Sokolik I.A.,Fiz. Tverd. Tela 9,1945(1967) (Sov. Phys.- Solid State 9,1532 (1967)).
5. Frankevich E.L. and Rumyantsev B.M., Zh. ETF Pis. Red.6,553(1967). (Sov. Phys. JETP Lett.6,70(1967)).
6. N.E.Geacintov,M.Pope and S.Fox, J.Phys.Chem.Solids Vol 31,pp.1375-1379(1970).
7. Frankevich E.L. and Sokolik I.A.,Solid State Comm. Vol.8,pp.251-253,1970.
8. V.Ern, H. Bouchriha, J. Fourny, and Delacote, Solid State Comm.,Vol.9,pp.1201-1203,1971.

Chapter VI

Conclusions:

We conclude this investigation by summarizing what was done and the significance of the results.

1. First the linear compressibilities of anthracene crystal were determined. These are important data not only to determine the correct pressure dependence of the band structure, exciton calculations, and the mobility tensor but they can also provide important information about the elastic properties of crystalline anthracene. Such information can result in better understanding of the intermolecular, and consequently interatomic potentials. A step was already done in this direction by numerically determining a set of elastic constants in the neighborhood of the experimental values and which predicts the correct linear compressibilities. The system also gives a positive definite strain energy, a criterion of a stable crystal.

2. We have calculated the band structure of crystalline anthracene and its pressure dependence using the actual linear compressibilities. These results were then used to calculate the drift mobility tensor and the Hall mobility in different directions and their pressure dependence. The calculations were made for an excess hole and an excess electron in both the constant relaxation time and the constant free path models. These calculations lead to very interesting results as follows:

(a) Although the technique used was generally the same as that developed by Le Blanc and modified by Katz et al, as pointed out by Katz the choice of the proper wavefunctions is most important in this case. We, for the first time, used the wavefunctions calculated by Hoyland and

Goodman and calculated both the two-center and the three-center integrals, Katz et al used them but they only calculated two-center integrals. With this choice of the wavefunctions we were able to predict the anisotropy of of the drift mobility tensor for holes which agrees remarkably well with experimental anisotropy in the ab plane. Although the mobility of holes in the c′ direction is about a factor of 2 smaller than the experimental mobility, it is the closest theoretical estimate for the latter. This difference with experiment may be partly due to the assumption of an isotropic relaxation time. For electrons the model predicts the anistropy of the drift mobility in the ab plane to agree quite well with experiment. However, it fails to come close to the experimental value of the electron mobility in the c direction. All these calculations so far were based on the constant relaxation time and constant free path models.

(b) For the first time theoretical predictions of the pressure dependence of the drift mobility tensor, based on the actual linear compressibilities, were available. Upon comparing these with the experimental data obtained by Kepler we found that they agreed surprisingly well in the c direction for holes while the theory predicted smaller change with pressure for the mobility in the ab plane, for both holes and electrons. The constant relaxation time model proved to be superior to the constant mean free path model in predicting the pressure data.

(c) The relaxation time calculated by comparing theoretical mobilities with experimental data is longer than that found by Katz et al. Consequently our uncertainity of energy, given by $\hbar/\tau$, is smaller than their value of both electron and hole. This result gives our model a better

internal consistency than theirs.

At this point we would like to point out that our calculations are closer to the experimental values of the drift mobilities and their pressure dependence than are other theoretical calculations.

3. A unique high pressure system was successfully developed with a non-magnetic high pressure cell which has two optical windows and five electrical leads available at the outside. This is a new contribution to the field of electrical and optical measurement at high pressure. No such cell was developed before.

4. A relatively large voltage with a polarity which is independent of the sense of the magnetic field develops at the Hall probe upon applying a magnetic field. Such an effect is believed to be due to the change of the longitudinal potential distribution along the sample. We believe that such a change could result from the effect of the magnetic field on the rate of detrapping of the filled trap centers. . This effect, being much larger than the expected Hall voltage masked the Hall voltage and made it impossible to have any quantitative measurement of the Hall mobility or its pressure dependence. Such a negative result indicates a need to develop, new carrier injection techniques which may not introduce as many triplet excitons or samples with fewer traps. Should experimental data of the Hall mobility and its pressure dependence be available in the future, they can be used to verify the theoretical predictions based on the band model made available by this investigation.

Appendix

Some details of the neutron diffraction experiment: The experiment was done on one of the standard neutron diffraction spectrometers at Brookhaven National Laboratory. The high pressure cell used was an aluminum cell in the shape of a spool with a cylindrical bore in it . The sample, a single crystal of anthracene in the shape of a rectangular parallelopiped, fitted inside the bore with the long edge parallel to the cylindrical axis. The cell was mounted on a goniometer which in turn was mounted on the spectrometer. The goniometer used has two perpendicular horizontal axes of rotation to allow adjusting the tilt of the sample in a range of 10°.

The published lattice parameters were used in a computer program which determined the approximate positions and intesities of the different Bragg reflection peaks. Three of the strong peaks were chosen to take data around. These as mentioned on page 39 were (200),(020), and (003). Two samples were used for final measurement. One sample had the b axis perpendicular to the diffraction plane and the second one had the a axis perpendicular to the diffraction plane.

Procedure.

After the cell with the sample inside it was mounted on the spectrometer a standard BF_3 counter was set at a value of a diffraction angle 2θ which corresponds to a strong peak in the plane perpendicular to the long edge of the sample. The sample was rotated along a vertical axis until the beam made an angle θ with the required planes. This was done by maximizing the diffracted intensity. At this position the tilt of the sample was adjusted by small rotations around the horizontal axes of the goniometer until an absolute maximum is obtained. In this position

the long edge of the sample is perpendicular to the diffraction plane. In the case of the sample with the long edge parallel to the b axis the counter was adjusted at the diffraction angles of a number of strong peaks and by rotating the sample around the vertical axis until the diffracted intensity was maximum the position of the peak was approximately determined. By iteratively changing the angle of the counter and the angle of the sample the best position of the peak was determined. This was taken to be half way between the two points of half maximum intensity. From the data taken on this sample we determined a, c , and the monoclinic angle β . The experiment was repeated at different pressures to give the parameters as functions of pressure up to 5.4 kilobars. The pressure system used is very similar to the one shown in fig. 5.1. From the sample with the long edge parallel to the a axis,b was determined.

The four parameters showed linear dependence up that pressure and the data were fitted to straight lines using the least square deviations method . the equations of these lines are equations 3.1-3.4.